Implications of Propeller-Wing Interactions on the Control of Aerodynamic-Surface-Free Tilt-Rotor Quad-Planes

Thesis Report

Noah Wechtler

TUDelft

Implications of Propeller-Wing Interactions on the Control of Aerodynamic-Surface-Free Tilt-Rotor Quad-Planes

Thesis Report

by

Noah Wechtler

to obtain the degree of Master of Science
at the Delft University of Technology
to be defended publicly on April 29, 2024 at 14:00

TUDelft

Delft
University of
Technology

Contents

Introduction

Quad-planes are hybrid vehicles which combine the hover capabilities of quadcopters and the forward flight efficiency of aircraft. Many quad-plane configurations exist, but the focus of this thesis lies on a particular configuration which utilizes four dual-axis tilt-rotors as means of propulsion and control [1]. In theory, this configuration allows for aerodynamic-surface-free flight, as the tilting rotors are able to fulfill the same functions. However, in reality, the quad-plane has not been able to achieve satisfactory roll control without use of ailerons.

It is believed that the discrepancy between theory and reality is caused by an oversimplification of the aero-propulsive modelling of the vehicle. To be precise, propeller-wing interactions are suspected to significantly dampen the roll moment generation of the tilt-rotors. As the control allocation framework used by the vehicle makes use of the aero-propulsive model, which does not include the propeller-wing interactions, this results in a suboptimal control allocation from the controller. Therefore, this thesis aims to identify the propeller-wing interactions present on the vehicle, as well as to find a solution which allows the vehicle to fly unhindered without aerodynamic surfaces.

This report consists of two parts, with Part I being a scientific article based on the findings of this research and Part II containing the literature study conducted at the start of the thesis. Additionally, a more elaborate explanation of the wind tunnel experiment conducted as part of this research is included in Appendix A and supporting figures for the flight tests can be found in Appendix B.

Part I

Scientific Article

Implications of Propeller-Wing Interactions on the Control of Aerodynamic-Surface-Free Tilt-Rotor Quad-Planes

Noah Wechtler

Delft University of Technology
Delft, The Netherlands

Abstract—**Quad-planes are a type of vehicle which combine the hovering capability of quadcopters and the forward flight efficiency of winged aircraft. Flight tests conducted on a dual-axis tilting-rotor quad-plane, designed to fly without aerodynamic surfaces, observed that the quad-plane suffered from insufficient roll authority during fast, forward flight. Subsequent wind tunnel testing confirmed a two- to fourfold reduction in roll moment generation from propellers mounted in front of the wing at similar levels of tilt as their rear counterparts, caused by propeller-wing interactions. To address the mismatch in actuator effectiveness shown by the wind tunnel experiment, the effect of the propeller-wing interactions was incorporated into the aero-propulsive model by means of a global polynomial, the structure of which was found using multivariate orthogonal function modelling. New flight tests demonstrated that, by including the propeller-wing interactions in the control allocation, the vehicle is capable of tracking a figure 8 maneuver without aerodynamic surfaces, and without compromising tracking performance.**

Index Terms—**UAV, Tilt-rotor, Quad-plane, Aero-propulsive Modelling, Propeller-wing Interactions**

Figure 1: Dual-axis tilt-rotor quad-plane developed by Mancinelli et al. [2]. Photo courtesy of Nico Voß.

I. INTRODUCTION

Quad-planes are a novel type of vehicle which combine the hovering capability of quad-copters and the forward flight efficiency of winged aircraft. Some quad-plane designs have separate rotors used for hovering and forward flight, such as the vehicle designed by Wang [1]. Other designs removed the need for separate hovering and forward flight propellers by incorporating tilting rotors. One such vehicle is the quad-plane developed by Mancinelli et al. shown in Figure 1. This particular quad-plane features four dual-axis tilt-rotors, which theoretically allow the vehicle to control all six degrees of freedom during hover, and five degrees of freedom during forward flight[1]. This offers new possibilities in the realm of disturbance rejection and dynamic maneuverability [2].

However, the dual-axis tilting rotors introduce additional complexity in terms of control system development and aero-propulsive modelling. The complexities in controlling the vehicle arise from the nonlinear actuator effectiveness. Mancinelli et al. proposed a Sequential Quadratic Programming (SQP) based algorithm which solves the Control Allocation (CA) problem by evaluating the nonlinear equations of motion. This CA algorithm is used in a modified Incremental Nonlinear Dynamic Inversion (INDI) control framework to effectively control the vehicle [3]. Particularly, INDI controllers are robust to model uncertainties [4] and external disturbances [5].

On the other hand, the aero-propulsive modelling of quad-planes has remained rather basic in comparison, with aerody-

namic models often based on the classical small perturbation theory stability derivatives [2, 6]. In the case of the dual-axis tilt-rotor quad-plane this rudimentary approach has resulted in a major shortcoming. Namely, flight tests revealed that the quad-plane had insufficient roll authority during fast, forward flight. This was unexpected, as the drone should have full control over this degree of freedom.

To carry out a roll maneuver, the control system chooses a suitable input based on its knowledge of the system dynamics [3], which means that the aero-propulsive model must be able to predict the change in forces and moments that occur from a change in rotor tilt-angle. However, this change in propeller elevation does not only affect the force and moment production of the propellers through the introduction of a non-zero inflow angle, but it also affects the angle at which the wake of the propellers meets the wing, which in turn affects the wing aerodynamics. Evidently, the interactions between the different subsystems are quite complex and many of these effects are not yet taken into account during the control allocation on the vehicle. This provides an obvious avenue of improvement and possible solution for the lack of roll control in fast, forward flight.

Nevertheless, addition of these effects to the new aero-propulsive model cannot be too computationally complex as it is used in the INDI controller, which has to maintain a certain minimum control frequency to keep the system stable [7]. Furthermore, the drone can only carry a limited amount of computing hardware onboard, further limiting the set of

---

[1]Due to gimbal lock, the propellers are unable to provide a lateral acceleration when the tilting mechanism is in forward flight configuration.

feasible modelling techniques.

Starting with the influence of the angle between the incoming airflow and the propeller disk, also called the inflow angle, on the performance of propellers. Theys et al. investigated how the propeller forces and torques vary as a function of the inflow angle [8]. They found that propeller thrust increases with the inflow angle. Rubin et al. attributed this to the fact that propellers act less like screws and more like rotating wings when the flow is parallel to the blades [9]. Additionally, Theys found that neither Blade Element Momentum Theory (BEMT) nor vortex lattice methods (VLM) accurately predicted the forces and torques across the entire range of inflow angles. Despite not accurately predicting forces and moments across the entire range of inflow angles, both methods did correctly identify the trends observed during the experiments. This sparked new developments such as the modified BEMT model by Leng et al. which uses an inflow correction to more accurately predict the forces at incidence [10]. Nevertheless, BEMT models currently require too much computational time to be used in real-time control. This was reinforced by the findings of Konuk and Landman, who tried to implement a modified BEMT model, but were unable to achieve sufficient computation speed for real time simulation [11], which is yet another step away from onboard control. Therefore, despite potentially having lower accuracy, models using simple explicit equations appear to be the only viable option due to the real time computation constraint imposed by the control system. One such model was derived by Gill et al. [12]. They derived an analytical BEMT model, which uses simplifications to bypass the need of finding a solution to the force and torque equations iteratively [12]. Fernandez et al. recently compared various available modelling approaches for propellers operating at incidence, and concluded that the model derived by Gill provided accurate results and due to the low computational cost is quite suitable for real time control purposes [13]. In contrast, Simmons et al. used system identification and blending functions to identify a globally valid propulsion model [14]. The main differences between the method of Simmons and the other proposed models is that Simmons lets the model identify its own structure, whereas the other models are based on theoretical derivations. Using an approach similar to Simmons is also promising, as it results in a simple set of polynomial equations which satisfy the computational and continuity requirements imposed by the controller. However, the method of Simmons requires the determination of parameters through wind tunnel testing. Although the method derived by Gill et al. does not strictly require wind tunnel data, using wind tunnel data to derive the model parameters leads to a more accurate model. This highlights a trend in the current propeller literature, namely that low order models require experimental data to produce accurate results throughout the entire range of inflow angles.

In contrast to propeller forces, the propeller-wing interactions of tilt-rotor vehicles are not as well documented, yet this phenomenon has also captured the attention of some researchers recently. For example, Yang et al. showed the slipstream curvature of a propeller at incidence from wind-tunnel experiments [15]. Additionally, they tried to model the slipstream using computational fluid dynamics (CFD), but CFD is far too computationally expensive to be used in real time simulation, let alone control. Meanwhile, most real time simulations use a momentum flow based method due to their simplicity and computational efficiency [16]. However, these methods assume that the flow behind the propeller is a cylinder without curvature, which is not applicable to the quad-plane as it neglects the fact that the freestream flow is not aligned with the cylinder and will therefore deform it. Conway derived an analytical solution from vortex theory, which can be used to determine the flow field behind a propeller [17]. This method of modelling propeller-wing interactions was recently applied to a tilt-wing tandem VTOL by May et al., but this method has not yet been experimentally validated for the particular application of tilt-rotor aircraft. Furthermore, also the analytical vortex solution does not take into account wake curvature either, and so the question remains whether this method will provide accurate results when applied to a tilt-rotor configuration. Lastly, Leng et al. describe a derivation based on vortex theory for an analytical model used to describe propeller-wing interactions, taking into account the effect of wing blockage on the wake [18]. Unfortunately, the analytical part of this model has not yet been extended to include the case of tilt-rotors. Clearly, there is a certain lack of propeller-wing interaction models tailored specifically around tilt-rotor vehicles, especially in the domain of real time computation.

Consequently, the goal of this research is twofold: First, investigate the lack of control over the roll axis during fast, forward flight by means of a wind tunnel campaign. Second, derive an extension to the stability derivative based aerodynamic model, with special emphasis on the propeller-wing interactions. With the additional constraint that the extension of the aerodynamic model must be compatible with the nonlinear CA algorithm and INDI controller used on the quad-plane.

II. METHOD

A. Reference Frames and Equations of Motion

Consider the quad-plane and the earth, body and propeller reference frames as shown in Figure 2. All coordinate systems are right-handed, of which the definitions are the following:

- Earth reference frame:
  - Origin fixed to the surface of the Earth.
  - $\hat{x}_e$ positive in the direction of North.
  - $\hat{y}_e$ positive in the direction of East.
  - $\hat{z}_e$ positive towards the center of the Earth.
- Body reference frame:
  - Origin fixed to quad-plane Center of Gravity (C.G.)
  - $\hat{x}_b$ positive out of the nose of quad-plane.
  - $\hat{y}_b$ positive out of the right wing.
  - $\hat{z}_b$ positive below the quad-plane.
- Propeller reference frame:
  - Origin fixed to center of rotation of ith propeller
  - $\hat{x}_p^i$ positive pointing out of the nose of the quad-plane in hovering configuration.
  - $\hat{y}_p^i$ positive pointing right in hovering configuration.
  - $\hat{z}_p^i$ aligned with the motor rotation axis, pointing in opposite direction of thrust.

Including the wind and control reference frames not shown in Figure 2:

- Wind reference frame:
  - Origin fixed to quad-plane C.G.
  - $\hat{x}_w$ positive in the direction of the velocity vector of the quad-plane relative to the air.

3

- $\hat{y}_w$ perpendicular to $\hat{x}_w$ and $\hat{z}_w$ positive to the right.
- $\hat{z}_w$ positive below the aircraft.

- Control reference frame:
  - Origin fixed to quad-plane C.G.
  - $\hat{x}_c$ positive out of the front of the quad-plane, running parallel with the surface of the Earth.
  - $\hat{y}_c$ perpendicular to $\hat{x}_c$ and $\hat{z}_c$ positive to the right.
  - $\hat{z}_c$ positive towards the center of Earth.
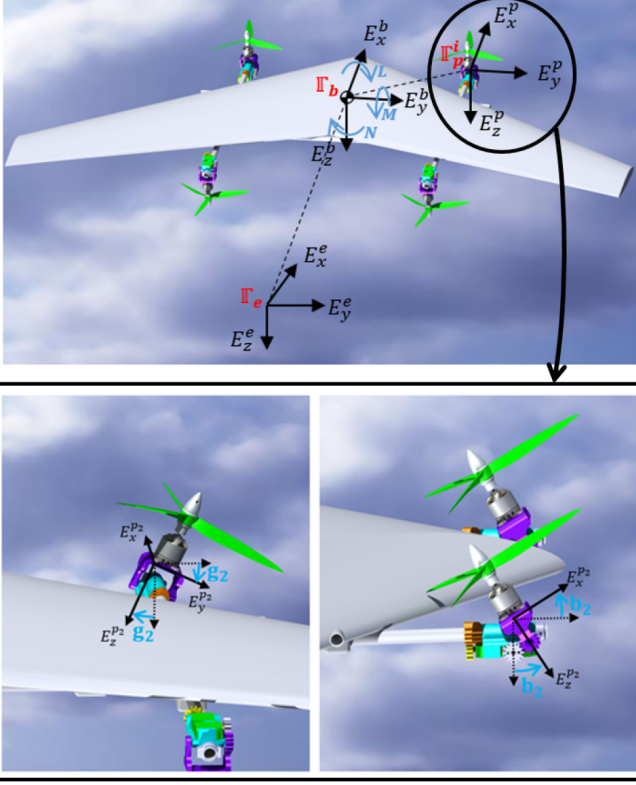

Figure 2: Quad-plane earth, body, and propeller frames [3]. Propeller elevation and azimuth are denoted by b_i and g_i respectively, starting with the first index in the front left and increasing clockwise. Note that the front left and rear right propellers spin counterclockwise, and the front right and rear left propellers spin clockwise.

The set of equations which govern the dynamics of the quad-plane can be expressed as:

$$\begin{cases} {}^e\ddot{P} = \frac{1}{m}\sum {}^e\boldsymbol{F} + g\hat{\boldsymbol{z}}_e \\ {}^b\dot{\omega} = I_b^{-1}\left(-\omega \times I_b\omega + \sum {}^b\boldsymbol{M}\right), \end{cases} \quad (1)$$

where ${}^e\ddot{P}$ are the linear accelerations expressed in the Earth frame and ${}^b\dot{\omega}$ are the angular accelerations expressed in the body frame. m and I_b are the mass and moment of inertia of the vehicle, respectively. $\sum {}^e\boldsymbol{F}$ and $\sum {}^b\boldsymbol{M}$ are the sum of all forces and moments applied to the quad-plane, expressed in the earth and body frame, respectively. For simplicity, only the aerodynamic and propulsive forces and moments are considered:

$$\begin{cases} \sum {}^e\boldsymbol{F} = {}^e\boldsymbol{F}_p + {}^e\boldsymbol{F}_a \\ \sum {}^b\boldsymbol{M} = {}^b\boldsymbol{M}_a + {}^b\boldsymbol{M}_p, \end{cases} \quad (2)$$

where the subscripts a and p refer to aerodynamic and propulsive effects, respectively. Aerodynamic forces are often calculated in the wind reference frame to simplify the resulting expressions. To transform the aerodynamic forces to the desired earth reference frame, an intermediate rotation to the body frame is first taken:

$$ {}^bR_w = \begin{bmatrix} c_\alpha c_\beta & -c_\alpha s_\beta & -s_\alpha \\ s_\beta & c_\beta & 0 \\ s_\alpha c_\beta & -s_\alpha s_\beta & c_\alpha \end{bmatrix}, \quad (3)$$

where c and s are abbreviations of the sin and cos functions and α and β denote the angle of attack and angle of sideslip, respectively. Subsequently, the rotation from body to the earth reference frame can be achieved using:

$$ {}^eR_b = \begin{bmatrix} c_\theta c_\psi & -c_\phi s_\psi + s_\phi s_\theta c_\psi & s_\phi s_\psi + c_\phi s_\theta c_\psi \\ c_\theta s_\psi & c_\phi c_\psi + s_\phi s_\theta s_\psi & -s_\phi c_\psi + c_\phi s_\theta s_\psi \\ -s_\theta & s_\phi c_\theta & c_\phi c_\theta \end{bmatrix}, \quad (4)$$

where θ is the pitch angle, ϕ the roll angle and ψ the yaw angle of the vehicle.

Similarly, the propulsive forces are usually calculated in the propeller reference frame. In this case, as the propellers are not fixed in alignment with the body, the forces and moments produced by the propellers are first converted to the body frame:

$$ {}^bR_p^i = \begin{bmatrix} c_{b^i} & 0 & s_{b^i} \\ s_{g^i}s_{b^i} & c_{g^i} & -s_{g^i}c_{b^i} \\ -c_{g^i}s_{b^i} & s_{g^i} & c_{g^i}c_{b^i} \end{bmatrix}, \quad (5)$$

where b^i and g^i are the elevation and azimuth angle of the ith propeller respectively as denoted in Figure 2. The tilting mechanism's range of motion in elevation can be seen in Figure 3, with the tilt-angle in hover and forward flight denoted by b_{hover} and b_{flight}. Additionally, the mechanism can achieve a ± 45 degree rotation side-to-side.
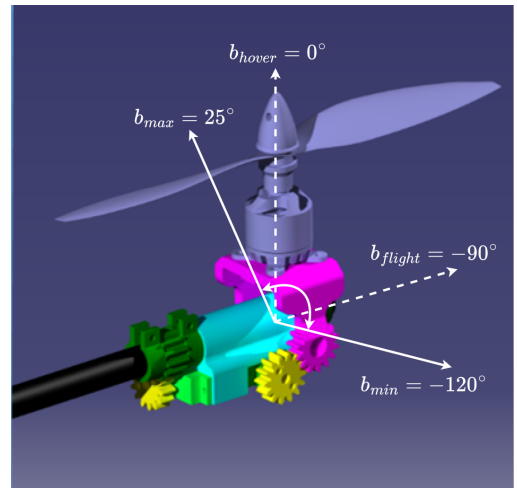
Figure 3: Elevation range of motion of the tilting mechanism, including hover and forward flight datums.

Lastly, the control allocation algorithm evaluates the linear accelerations in the control reference frame. The rotation from body to control reference frame is defined by:

$$ {}^cR_b = \begin{bmatrix} c_\theta & s_\phi s_\theta & c_\phi s_\theta \\ 0 & c_\phi & -s_\phi \\ -s_\theta & s_\phi c_\theta & c_\phi c_\theta \end{bmatrix}. \quad (6)$$

4

B. Aerodynamic Model

As mentioned in the introduction, the aerodynamic forces are calculated using stability derivatives:

$$^e\boldsymbol{F}_a = {}^eR_b \, {}^bR_w \frac{1}{2}\rho V^2 S \begin{bmatrix} C_{D_0} + k_{C_d}\left(C_{L_0} + C_{L_\alpha}\alpha\right)^2 \\ C_{Y_\beta}\beta \\ C_{L_0} + C_{L_\alpha}\alpha \end{bmatrix}. \tag{7}$$

Where, in addition to the aerodynamic coefficients, the air density is given by ρ, the airspeed by V and the wing surface area by S.

Similarly, the aerodynamic moments expressed in the body frame are calculated using:

$$^b\boldsymbol{M}_a = \frac{1}{2}\rho V^2 S \begin{bmatrix} b\left(C_{l_0} + C_{l_\beta}\beta + \frac{b}{2V}\left(C_{l_p}p + C_{l_r}r\right)\right) \\ c\left(C_{m_0} + C_{m_\alpha}\alpha\right) \\ \frac{b^2}{2V}\left(C_{n_p}p + C_{n_r}r\right) \end{bmatrix}, \tag{8}$$

where p, q and r are the roll, pitch and yaw rates. Additionally, the wingspan is represented by b and the mean aerodynamic chord by c.

None of the propeller-wing interaction models mentioned in the introduction generalized well to the tilt-rotor quad-plane, which led to the adoption of a global error correction polynomial. This polynomial will be used to correct the dimensionless roll moment coefficient for the propeller-wing interactions. The reason behind using polynomials lies in the fact that they are simple to implement and troubleshoot, but any other approximation method could also be used.

For now, it is assumed that the roll moment correction is a function of the propeller rotational velocity Ω, the airspeed V and the propeller elevation angle b:

$$\Delta C_{Mx} = f\left(\Omega_{1\text{-}4}, V, b_{1\text{-}4}\right), \tag{9}$$

which can be modelled by subtracting the roll moment coefficient generated by the wingless quad-plane from the roll moment coefficient generated by the regular quad-plane:

$$\Delta C_{Mx}\left(\Omega_{1\text{-}4}, V, b_{1\text{-}4}\right) = C_{Mx_{\text{wing}}} - C_{Mx_{\text{wingless}}}. \tag{10}$$

Finally, the error correction term can be added in straightforward fashion to Equation 8:

$$^b\boldsymbol{M}_{a,\text{new}} = {}^b\boldsymbol{M}_a + \frac{1}{2}\rho V^2 S \begin{bmatrix} b\Delta C_{Mx} \\ 0 \\ 0 \end{bmatrix}. \tag{11}$$

This process can easily be generalized to the other moment components as outlined in Appendix A.

C. Propulsive Model

The 5-component propeller model derived by Gill et al. [12] was implemented to replace the static thrust model used previously. This model maps the propeller forces and moments to the propeller rotational speed Ω, airspeed V and inflow angle i_p by assuming a specific blade geometry and linear aerodynamics.

First, the propeller radius R, rotational speed of the propeller, airspeed, and inflow angle are related to the climb ratio λ_c and advance ratio μ:

$$\lambda_c = \frac{V\cos\left(i_p\right)}{\Omega R}, \; \mu = \frac{V\sin\left(i_p\right)}{\Omega R}. \tag{12}$$

Additionally, the propeller model depends on the solidity ratio σ:

$$\sigma = \frac{N_b c_{tip}}{\pi R}. \tag{13}$$

The induced inflow λ_i is then computed using Equation 18, which can be summed with the climb ratio λ_c to obtain the total inflow λ:

$$\lambda = \lambda_c + \lambda_i, \tag{14}$$

The propeller thrust and drag coefficients are computed using Equation 19 and Equation 20. Meanwhile, the roll, pitch, and yaw moment coefficients are computed using Equation 21, Equation 22 and Equation 23, respectively.

Whereupon the propeller forces and moments are expressed as functions of the force and moment coefficients:

$$\begin{bmatrix} F_T \\ F_x \\ M_Q \\ M_R \\ M_P \end{bmatrix} = \begin{bmatrix} C_{FT}\left(\lambda, \mu\right)\frac{1}{2}\rho R^2\left(\Omega R\right)^2 \\ C_{FX}\left(\lambda, \mu\right)\frac{1}{2}\rho R^2\left(\Omega R\right)^2 \\ C_{MQ}\left(\lambda, \mu\right)\frac{1}{2}\rho R^3\left(\Omega R\right)^2 \\ C_{MR}\left(\lambda, \mu\right)\frac{1}{2}\rho R^3\left(\Omega R\right)^2 \\ C_{MP}\left(\lambda, \mu\right)\frac{1}{2}\rho R^3\left(\Omega R\right)^2 \end{bmatrix}, \tag{15}$$

the definition and assumed positive direction of which are shown in Figure 4.

The propeller forces expressed in the Earth reference frame are given by:

$$^e\boldsymbol{F}_p = \sum_{i=1}^{4} {}^eR_b^i \, {}^bR_p^i \begin{bmatrix} -{}^pF_x^i \\ 0 \\ -{}^pF_T^i \end{bmatrix}. \tag{16}$$

Likewise, the propeller moments expressed in the body frame can be computed:

$$^b M_p = \sum_{i=1}^{4}\left(\begin{bmatrix} l_x^i \\ l_y^i \\ l_z^i \end{bmatrix} \times \left({}^bR_p^i F_p^i\right) + {}^bR_p^i \begin{bmatrix} (-1)^i M_R^i \\ M_P^i \\ (-1)^{i+1} M_Q^i \end{bmatrix}\right). \tag{17}$$

The resulting equations are computationally efficient due to their explicit nature. Nevertheless, the model accuracy heavily relies upon a set of nine parameters:

$$\begin{bmatrix} c_{l_0} & c_{l_a} & c_{d_0} & c_{d_a} & c_{m_0} & c_{m_a} & \delta & \theta_{tip} & c_{tip} \end{bmatrix},$$

where c_{l_0}, c_{l_a}, c_{d_0}, c_{d_a}, c_{m_0} and c_{m_a} define the aerodynamics of the propeller airfoil. δ represents the fraction of the propeller blade which is not useful, θ_{tip} is the propeller pitch angle at the tip and c_{tip} is the propeller tip chord.

Gill proposed two methods to estimate these parameters. The first method, which is considered more accurate, consists of fitting the parameters to wind tunnel data using nonlinear optimization. As this method requires dedicated wind tunnel time, it was instead decided to go with the second method.

The second method assumes certain values based on observations made by Gill et al. during the making of their paper, which reduces the optimization problem into two separate root finding problems. This root finding problem only requires the static thrust and moment coefficient of the propellers, which

$$\lambda_i\left(\lambda_c,\mu\right) = \frac{1}{8}\left(-4\lambda_c + c_{l,a}\sigma\left(\delta-1\right) + \left(16\lambda_c^2 + 8c_{l,a}\left(\delta-1\right)\lambda_c\sigma \right.\right.$$
$$\left.\left. + \frac{1}{\delta}\left(\delta-1\right)\sigma\left(-8c_{l,0}\delta\left(1+\delta\right) + c_{l,a}\left(c_{l,a}\left(\delta-1\right)\delta\sigma - 8\left(2\delta+\mu^2\right)\theta_{tip}\right)\right) - 8c_{l,0}\mu^2\sigma\ln\left(\delta\right)\right)^{\frac{1}{2}}\right) \tag{18}$$

$$C_{FT}\left(\lambda,\mu\right) = \frac{\sigma}{2\delta}\left(\left(1-\delta\right)\left(c_{l,0}\delta\left(1+\delta\right) - 2c_{l,a}\delta\left(\lambda-\theta_{tip}\right) + c_{l,a}\mu^2\theta_{tip}\right) - c_{l,0}\delta\mu^2\ln\left(\delta\right)\right) \tag{19}$$

$$C_{FX}\left(\lambda,\mu\right) = \frac{\mu\sigma}{2\delta}\left(\left(1-\delta\right)\left(2c_{d,0}\delta + \theta_{tip}\left(\left(c_{l,a}-2c_{d,a}\right)\lambda + 2c_{d,a}\theta_{tip}\right)\right) - c_{l,0}\delta\lambda\ln\left(\delta\right)\right) \tag{20}$$

$$C_{MR}\left(\lambda,\mu\right) = \frac{1}{2}\left(1-\delta\right)\sigma\mu\left(c_{l,0}\left(\delta+1\right) - c_{l,a}\left(\delta-2\theta_{tip}\right)\right) \tag{21}$$

$$C_{MP}\left(\lambda,\mu\right) = \frac{c_{tip}}{2\delta R}\sigma\mu\left(c_{m,a}\left(\delta-1\right)\left(\delta-2\theta_{tip}\right) - 2c_{m,0}\delta\ln\left(\delta\right)\right) \tag{22}$$

$$C_{MQ}\left(\lambda,\mu\right) = \frac{1}{6}\left(1-\delta\right)\sigma\left(2c_{d,0}\left(1+\delta+\delta^2\right) + 3c_{l,0}\left(\delta+1\right)\lambda + 6\left(c_{d,a}\left(\lambda-\theta_{tip}\right) - c_{l,a}\lambda\right)\left(\lambda-\theta_{tip}\right)\right.$$
$$\left. + \frac{3\mu^2\left(c_{d,0}\delta + c_{d,a}\theta_{tip}^2\right)}{\delta}\right) \tag{23}$$

Figure 4: Counter-clockwise rotating propeller force and moment definitions [12]. For a clockwise rotating propeller, the direction of assumed positive M_Q and M_P are inverted.

had already been determined during initial developments of the drone. A root finding algorithm is then used to determine the two remaining parameters, consisting of c_{l_a} and c_{d_a}.

D. Computation of the Inflow Angle

As discussed in the previous section, part of the propeller model relies on the inflow angle i_p. The inflow angle is a function of propeller orientation and airspeed vector, and it can be determined using the definition of the angle between two vectors:

$$\cos\left(i_p^i\right) = \frac{\boldsymbol{V}\cdot -\,{}^b\hat{\boldsymbol{z}}_p^i}{\|\boldsymbol{V}\|\,\|-\,{}^b\hat{\boldsymbol{z}}_p^i\|}, \tag{24}$$

$$\sin\left(i_p^i\right) = \frac{\boldsymbol{V}\times -\,{}^b\hat{\boldsymbol{z}}_p^i}{\|\boldsymbol{V}\|\,\|-\,{}^b\hat{\boldsymbol{z}}_p^i\|}\cdot{}^b\hat{\boldsymbol{y}}_p^i. \tag{25}$$

Multiplying with ${}^b\hat{\boldsymbol{y}}_p^i$ in Equation 25 is necessary to distinguish between positive and negative elevation angles. Note that $\cos\left(i_p\right)$ and $\sin\left(i_p\right)$ are used directly by the propeller

model, making it unnecessary to invert the expressions to obtain i_p itself.

However, these definitions are only valid for non-zero airspeed. Luckily, the outcome of the propeller model does not depend on the inflow angle when the airspeed is zero. Therefore, i_p can be assumed zero when the airspeed is zero. Alternatively, it is possible to leverage certain implementations of the arctan2 function to bypass the need for special treatment when the airspeed is zero. The definition of the inflow angle then becomes:

$$i_p^i = \arctan2\left(\left(\boldsymbol{V}\times -\,{}^b\hat{\boldsymbol{z}}_p^i\right)\cdot{}^b\hat{\boldsymbol{y}}_p^i,\ \boldsymbol{V}\cdot -\,{}^b\hat{\boldsymbol{z}}_p^i\right). \tag{26}$$

The sideslip angle can be discarded in the calculation of the inflow angle to further simplify the equations used in the real time control allocation:

$$i_p^i = b^i + \frac{\pi}{2} + \alpha, \tag{27}$$

where the $\frac{\pi}{2}$ offset is necessary, as the elevation angle and inflow angle are offset by 90 degrees due to the definition of b^i given in Figure 3.

E. Wind Tunnel Experiment

A wind tunnel test was carried out to identify aerodynamic forces and moments as well as isolate the roll moment coefficient discussed in the previous sections. The wind tunnel experiment was performed in TU Delft's Open Jet Facility.

The experiment contains four independent variables: airspeed, propeller rotational speed, front propeller elevation and rear propeller elevation. To reduce the number of test cases, and because the vehicle is symmetric, only the right side rotors were tilted. Additionally, propellers were all spun at the same RPM during each of the test cases. Furthermore, the setup was fixed at an angle of attack of six degrees, regardless of the velocity, as this is a representative angle of attack for the

tested flight regime.

Figure 5 shows the test setup, including body and sensor reference frames.

Figure 5: Wind tunnel experiment setup of the quad-plane, with sensor and body frames shown. Note that the drone is mounted upside down.

During testing, the wind tunnel velocity was varied between 9 and 15 meters per second in steps of three meters per second. The rotational velocity of the propellers was varied between 600 and 1000 radians per second. Cases in which the rotors could not produce more thrust than to overcome the drag caused by the quad-plane were discarded from the experiment to save time. The front and rear propellers were deflected from -120 to +20 degrees in increments of 10 degrees. Refer to Figure 2 and Figure 3 for a definition of these tilt angles. Unfortunately, the propeller elevation range had to be reduced to [-120, -60] degrees, when rotational velocities were equal to or exceeded 900 radians per second. This was done to limit the heat produced by the motors, as prolonged testing would eventually lead to a weakening of the Polylactic Acid (PLA) motor mount. An overview of the experiment matrix can be found in Table I.

This experiment matrix was run twice, once with the complete drone and once without the wing, as shown in Figure 5 and Figure 6, respectively.

As mentioned previously, all propellers were spun at the same RPM. Consequently, it will not be possible to derive a model containing both front and rear propeller RPM as input. However, it is assumed that the front propellers dominate the propeller-wing interactions, which is supported by section III-B. As such, it is unnecessary to include the RPM of the rear propeller in the derivation of the model. Additionally, only the right side propellers were tilted. Therefore, Equation 10 will be computed in two parts. First, the roll moment error coefficient as a function of right side propeller tilt (b_2, b_3) and front right propeller rotational speed (Ω_2) is computed:
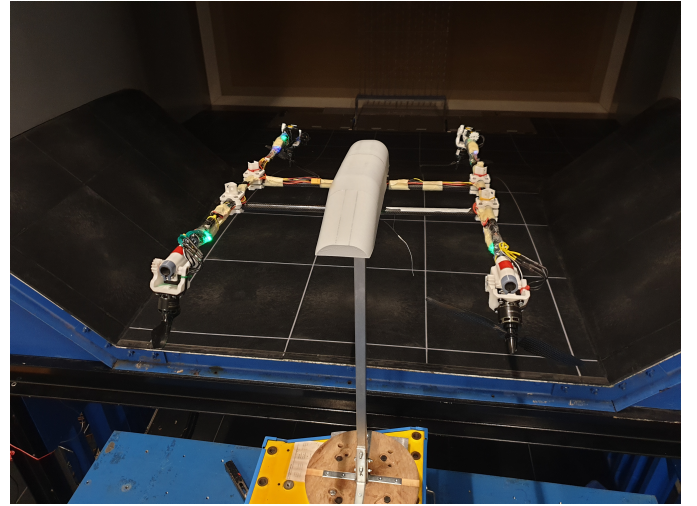
Figure 6: Wind tunnel experiment setup of the quad-plane skeleton.

$$\Delta C_{Mx_r}(\Omega_2, V, b_2, b_3) = C_{Mx_{\text{wing}}} - C_{Mx_{\text{wingless}}}. \quad (28)$$

Then, the roll moment error coefficient as function of left side propeller tilt (b_1, b_4) and front left propeller rotational speed (Ω_1) is computed using the same function and simply inverting the sign:

$$\Delta C_{Mx_l} = -\Delta C_{Mx_r}(\Omega_1, V, b_1, b_4). \quad (29)$$

Both terms can then be added to give rise to the final term used in Equation 10:

$$\Delta C_{Mx} = \Delta C_{Mx_r} + \Delta C_{Mx_l}. \quad (30)$$

F. Multivariate Orthogonal Function Modelling

To find suitable expressions for the error correction term ΔC_{Mx}, multivariate orthogonal function (MOF) modelling was employed. MOF modelling was chosen over regular polynomial fitting, due to MOF's ability to easily determine which terms are most relevant in modelling the response [19]. This is important due to the computational requirements imposed by the controller, to prevent overfitting, and to reduce the time spent searching for important terms. The QR-decomposition based method of generating orthogonal functions, described by Morelli et al. [20], will be outlined in this paper. Alternatively, the Gram-Schmidt procedure has also been used to generate orthogonal functions [19].

The first step is to settle on a set of suitable candidate modelling functions. Subsequently, the regular least squares problem is solved for all candidate modelling functions:

$$z = X\Theta + \epsilon, \quad (31)$$

where z is the N dimensional system response, Θ the M dimensional vector of unknown parameters, X the $N \times M$ dimensional matrix of candidate modelling functions and ϵ the N dimensional vector of equation errors.

The unknown parameter vector Θ can be estimated by minimizing the least squares cost function:

$$J(\Theta) = \frac{1}{2}(z - X\Theta)^T(z - X\Theta), \quad (32)$$

Table I: Range of propeller elevation angles tested during the wind tunnel experiment given certain wind tunnel and rotor speed combinations. Propeller elevation angles were varied in ten degree increments, and cases which were not tested are labelled N.T.

	600 [rad/s]	700 [rad/s]	800 [rad/s]	900 [rad/s]	1000 [rad/s]
9 [m/s]	[-120, 20]	[-120, 20]	[-120, 20]	[-120, -60]	[-120, -60]
12 [m/s]	N.T.	N.T.	[-120, 20]	[-120. -60]	[-120, -60]
15 [m/s]	N.T.	N.T.	N.T.	[-120, -60]	[-120. -60]

which has the solution:

$$\hat{\Theta} = \left(X^T X\right)^{-1} X z^T. \tag{33}$$

Conventionally, the output of the regular least squares model is computed using:

$$\hat{y} = X\hat{\Theta}. \tag{34}$$

However, the goal is to find a smaller subset of basis functions to model the error correction term. Therefore, the vector of modelling functions X can be orthogonalized using a QR decomposition:

$$X = QR, \tag{35}$$

where Q has the same dimensions as the matrix of modelling functions X and R is a square upper triangular matrix.

The general form of a MOF model is equal to that of the least squares model given in Equation 31. However, the matrix of modelling functions, X, is now replaced with the orthonormal matrix Q obtained from QR decomposition:

$$z = Qa + \epsilon, \tag{36}$$

where a is the unknown vector of orthogonal parameters.

The j$^{\text{th}}$ term of the unknown vector of orthogonal parameters, $\hat{a}_j$, is computed using the j$^{\text{th}}$ column of the orthonormal matrix Q:

$$\hat{a}_j = q_j^T z. \tag{37}$$

To determine which terms will be discarded, two metrics will be considered. First, the orthonormal modelling functions are chosen to minimize the predicted squared error (PSE) [20]:

$$PSE = \frac{1}{N}\left(z^T z - \sum_{j=1}^{n}\left(q_j^T z\right)^2\right) + \sigma_{max}^2 \frac{n}{N}, \tag{38}$$

where n is the number of considered candidate functions, and the maximum model fit error variance σ_{max}^2 can be estimated using [20]:

$$\sigma_{max}^2 = 25\hat{\sigma}^2 = 25\frac{(z - \hat{y})^T (z - \hat{y})}{N - n}. \tag{39}$$

The first term in Equation 38 is also referred to as the mean squared fit error (MSFE), whereas the second term is an overfit penalty, which is proportional to the number of chosen modelling functions. The PSE function has one global minimum, because the MSFE term decreases with each addition of a new function, whereas the overfit penalty increases with each addition of a new function [19]. The PSE criterion can further be reduced to:

$$\left(q_j^T z\right)^2 > \sigma_{max}^2, \tag{40}$$

because $z^T z$, σ_{max}^2 and N solely depend on the dependent variable data [20].

Additionally, the orthogonal modelling functions are chosen such that they have a meaningful contribution to modelling the variation around the mean. This is done by computing the ΔR^2 achieved through addition of each new function. The ΔR^2 is computed using:

$$\Delta R_{min}^2 \leq \frac{\left(q_j^T z\right)^2}{\left(z^T z - N\bar{z}\right)}, \tag{41}$$

where a ΔR_{min}^2 cut-off of 0.005 was chosen [20].

Furthermore, due to the procedural nature of the orthogonalization algorithm, the order in which functions are introduced can greatly change the number of terms which are selected [21]. Since each orthogonal function depends on the previous function to form a basis, non-significant terms which appear before the final significant term must also be kept.

The least squares cost function for the orthogonal functions is given by:

$$J\left(\hat{a}\right) = \frac{1}{2}\left(z^T z - \sum_{j=1}^{n}\left(q_j^T z\right)^2\right), \tag{42}$$

where only $\left(q_j^T z\right)^2$ is dependent on the chosen functions. Therefore, to reduce the dependence on the order of terms, terms should be sorted by their contribution to $\left(q_j^T z\right)^2$ and they should be introduced in that order. All orthogonal functions which satisfy both the PSE and the ΔR^2 requirement are then chosen as the basis for the polynomial model. Finally, to obtain a physically meaningful polynomial, the ordinary least squares procedure is repeated, this time containing only the subset of m selected terms:

$$\hat{y} = X_m \hat{\Theta}_m. \tag{43}$$

G. Controller Implementation of the New Aero-Propulsive Model

The quad-plane controller is based on an Incremental Nonlinear Dynamic Inversion (INDI) framework, wherein the nonlinear dynamic inversion is achieved through a Sequential Quadratic Programming (SQP) algorithm [3]. The cost function used in the nonlinear optimization is given by:

$$C\left(u\right) = \|W_\nu \left(f\left(x, u\right) - \nu\right)\|^2 + \left\|\gamma^{\frac{1}{2}} W_u \left(u - u_d\right)\right\|^2, \tag{44}$$

where $f\left(x, u\right)$ are the nonlinear equations of motion of the vehicle expressed in the control reference frame, ν are the desired global accelerations, and u are the actuator inputs. The

remaining terms are weights used to fine tune the solution.

As this scheme makes use of the nonlinear vehicle dynamics to find the solution to the CA problem, it is possible to integrate the derived aerodynamic model into the control allocation algorithm, provided that it does not increase the computational requirements beyond a certain threshold.

Upon implementing the new aerodynamic models into the nonlinear controller, it was noticed that the CA algorithm prioritized tilting the rotors over using the wing in some climb and straight flight conditions. Due to the model's dependence on airspeed and inflow angle, and the inclusion of the RPM in the cost function, the minimization of the cost function would result in a condition where the propellers were tilted excessively. To solve this issue, the secondary objective term related to RPM was replaced by the motor power:

$$P_{motor}^i = M_Q^i \Omega^i, \tag{45}$$

where M_Q is the magnitude of the propeller yaw moment as given by Equation 23. The motor power was then normalized, effectively limiting the range to:

$$0 \le P_s \le 2. \tag{46}$$

The change in the secondary objective of Equation 44 is reflected by:

$$\left\| \gamma^{\frac{1}{2}} W_\Omega \left(\Omega - \Omega_d \right) \right\|^2 \to \left\| \gamma^{\frac{1}{2}} W_P \left(P_s - P_d \right) \right\|^2, \tag{47}$$

where W_P is a new weight related to the power.

III. RESULTS

A. Polynomial Fit of Experimental Data

First, a set of basis functions was chosen, which were used to fit the wind tunnel data:

$$\begin{bmatrix} V_s & \Omega_{F,s} & \sin\left(b_F\right) & \cos\left(b_F\right) & \sin\left(b_R\right) & \cos\left(b_R\right) \end{bmatrix}, \tag{48}$$

where the subscripts F and R refer to the front and rear propellers respectively. The airspeed and propeller rotational velocity were scaled such that they stay within the range $[0, 2]$. The subscript s will be used whenever scaled values are used.

Then, both the data pertaining to the wing and wingless configuration were fit to a global fourth order polynomial. The full fourth order polynomial with six variables, including cross terms and a bias term, consists of 210 terms. However, the order of individual variables was limited to two to resolve issues with diverging polynomials, reducing the number of possible terms to 168. Table II shows the Root-Mean-Square Error (RMSE) of the polynomial fit, as well as the R^2 value. Additionally, the number of terms used in the MOF shortened polynomial are shown. Both shortened, and full polynomials show good agreement with the experiment data, with high R^2 values above 0.97 in all cases. Most importantly, the RMSE of the roll moment coefficient (C_{M_x}) is small, as the experiment was tailored around finding the influence of tilt on the roll moment.

Table II: Comparison of the full and shortened fourth order polynomial fit of wing experimental data.

	RMSE full	R^2 full	RMSE short	R^2 short	n_{terms}
C_{M_x}	0.000939	0.998	0.00313	0.983	6
C_{M_y}	0.00876	0.999	0.0392	0.977	9
C_{M_z}	0.00118	0.997	0.00357	0.975	10

Similarly, the polynomials related to the wingless configuration show good agreement with the experimental data, with high R^2 values and low RMSE as shown in Table III.

Table III: Comparison of the full and shortened fourth order polynomial fit of skeleton experimental data.

	RMSE full	R^2 full	RMSE short	R^2 short	n_{terms}
C_{M_x}	0.000817	0.999	0.00317	0.989	6
C_{M_y}	0.00647	0.999	0.0391	0.974	10
C_{M_z}	0.00107	0.998	0.00453	0.972	10

Since the error term is a function of the wing and wingless polynomial, it is possible to obtain the coefficients exactly, as both polynomials can be subtracted from each other. This means that the resulting error terms have similar accuracy.

B. Roll Moment Investigation

The six terms which model the shortened roll moment coefficient polynomial for tilting the right side propellers are:

$$\begin{aligned} \Delta C_{Mxr} = {} & c_1 \Omega_{2_s} \cos\left(b_2\right) + c_2 \Omega_{2_s} \sin\left(b_3\right) \cos\left(b_2\right)^2 \\ & + c_3 V_s^2 \Omega_{2_s} \cos\left(b_2\right) + c_4 \Omega_{2_s} \sin\left(b_2\right) \cos\left(b_3\right)^2 \\ & + c_5 \Omega_{2_s} \sin\left(b_3\right) \cos\left(b_3\right)^2 + c_6 \Omega_{2_s}^2 \cos\left(b_2\right), \end{aligned} \tag{49}$$

with the coefficients given in Table IV.

Table IV: Shortened roll moment coefficients for tilting right side propellers.

Coeff.	c_1	c_2	c_3	c_4	c_5	c_6
Value	0.012	-0.0040	-0.021	0.0045	-0.0065	0.0075

The roll moment can be plotted as a function of airspeed, propeller rotational speed and propeller elevation angle. Figure 7 shows the experimental data in a slow flight condition of nine meters per second, where the propellers are spinning at 600 radians per second. Clearly, using the front propellers to generate a rolling moment is inefficient when the wing is mounted. On the other hand, the presence of the wing has a negligible effect on the roll moment generation of the rear propellers.

The same holds true if the propeller rotational speed is increased to 1000 radians per second, as shown in Figure 8.

The effect becomes slightly less pronounced at a higher airspeed of fifteen meters per second. Nevertheless, the rear propellers are still at least twice as effective in generating a roll moment as shown in Figure 9.

It is likely that the front propellers induce a downwash on the wing, which in turn reduces the lift produced by the wing section located behind the propellers. The local reduction in lift generates a roll moment which opposes the moment generated by front propellers, effectively reducing the total roll moment. This confirms the existence of non-negligible propeller-wing
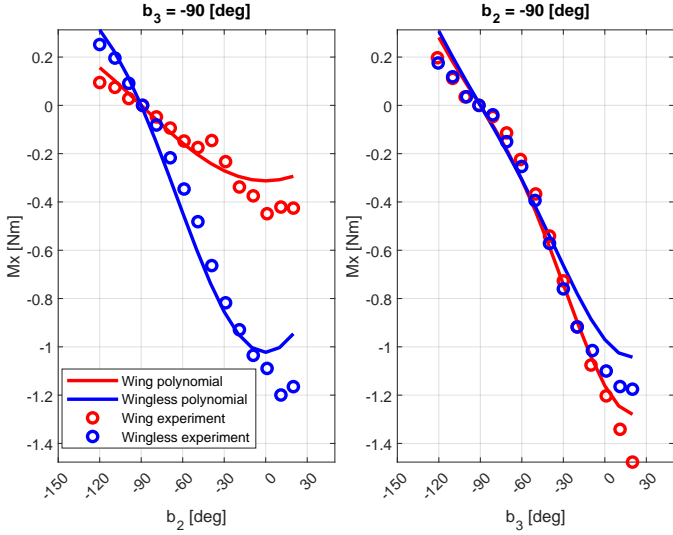
Figure 7: Rolling moment as a function of right side front (b_2) and rear (b_3) propeller elevation, Ω = 600 rad/s and V = 9 m/s. Zero degrees elevation corresponds to the hover configuration, and -90 to forward flight.
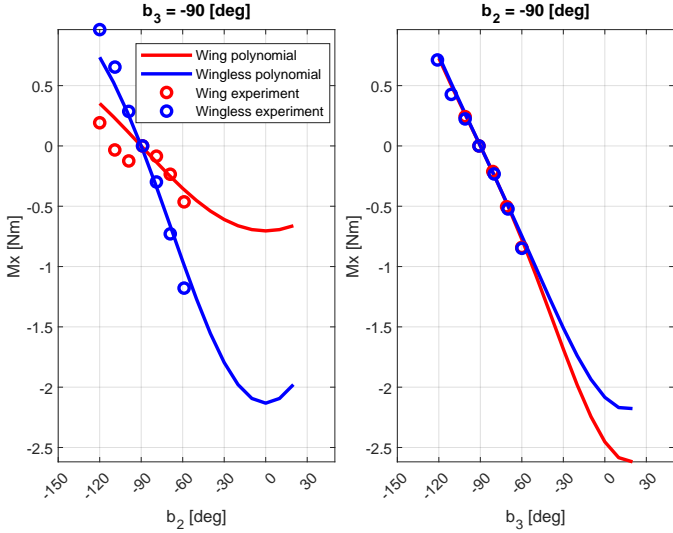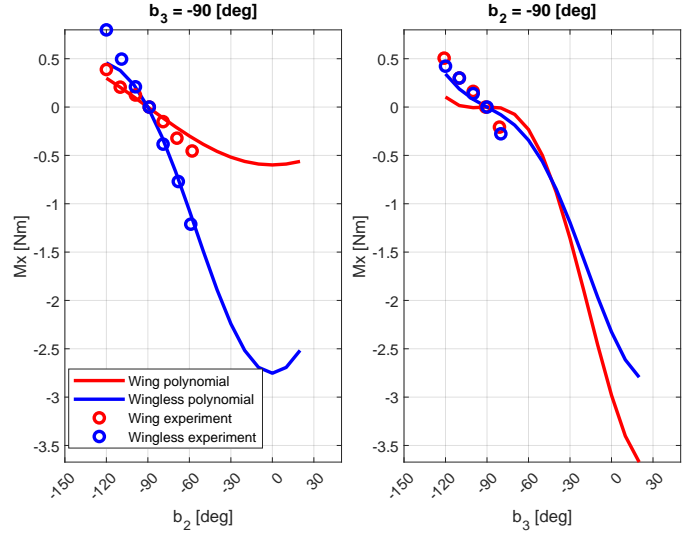

Figure 9: Rolling moment as a function of right side front (b_2) and rear (b_3) propeller elevation, Ω = 1000 rad/s and V = 15 m/s. Zero degrees elevation corresponds to the hover configuration, and -90 to forward flight.

Figure 8: Rolling moment as a function of right side front (b_2) and rear (b_3) propeller elevation, Ω = 1000 rad/s and V = 9 m/s. Zero degrees elevation corresponds to the hover configuration, and -90 to forward flight.

interactions, which result in an inaccurate estimation of the front rotor actuator effectiveness. Although INDI is robust to model uncertainties [4], the overestimation of the front propeller effectiveness likely resulted in insufficient roll control, as experienced in early stages of the quad-plane's development.

C. Determination of Propeller model parameters

As the propellers were not independently tested during the wind tunnel campaign, the propeller model parameters were obtained through the second method described by Gill et al. [12]. This method requires that the propeller was previously tested on a static test bed to determine the static thrust C_T and torque C_Q coefficients. Where the static propeller model is given by:

$$T = C_T \Omega^2, \ Q = C_Q \Omega^2. \qquad (50)$$

The drone is using T-motor carbon fiber 10x5.5 propellers with a static thrust coefficient of $0.95 \cdot 10^{-5} [kg \cdot m]$ and a static moment coefficient of $1.31 \cdot 10^{-7} [kg \cdot m^2]$. Additionally, the propeller tip chord was measured to be eleven millimeters, and the pitch at the propeller tip can be obtained using [12]:

$$\theta_{tip} = \frac{1.25P}{2\pi R}, \qquad (51)$$

where P and R are the propeller pitch and radius, respectively. The propeller pitch can usually be inferred from the propeller name. Since a 10x5.5 propeller is used, the propeller pitch is equal to 5.5 inches. Furthermore, as there is no information present on the propeller airfoil, Gill recommends the usage of standard values for the following aerodynamic properties: the lift coefficient at zero angle of attack c_{l_0}, the moment coefficient at zero angle of attack c_{m_0} and the moment coefficient derivative with respect to alpha c_{m_a} should all be assumed equal to 0. The drag coefficient at zero angle of attack c_{d_0}, is set to 0.05. Finally, δ is assumed to be equal to 0.2. This reduces the problem to two separate root finding problems to determine the propeller c_{l_a} and c_{d_a}:

$$\text{find } c_{l_a} \text{ s.t. } F_T(\Omega, V = 0, i_p = 0) = C_T \Omega^2, \qquad (52)$$

$$\text{find } c_{d_a} \text{ s.t. } M_Q(\Omega, V = 0, i_p = 0) = C_Q \Omega^2. \qquad (53)$$

The parameters obtained through the static propeller model and root finding are shown in Table V.

Table V: Propeller model parameters obtained using static propeller thrust and moment coefficient.

C_{l_0}	C_{l_a}	C_{d_0}	C_{d_a}	C_{m_0}	C_{m_a}	δ	θ_{tip}	c_{tip}
0.0	3.42	0.05	0.32	0	0	0.2	0.22	0.011

D. Force-Torque comparison between Simulation and Wind tunnel Experiment

The aero-propulsive models including and excluding the roll moment correction were tested against the wind tunnel data,

to ensure that adding the difference polynomials and propeller model had a positive effect on model accuracy. Table VI shows the RMSE and error distributions of the new and old model in relation to the wind tunnel test data. Besides the vertical force, F_z, all forces and moments saw an improvement in the RMSE value. F_x saw an extreme improvement due to the new propeller model. Most importantly, the RMSE, mean and standard deviation of the error in M_x improved with the addition of the polynomials.

Table VI: RMSE, and error distributions of the original model using pure stability derivatives and a static propeller model, and the new aero-propulsive model including ΔM_x and Gill's propeller model [12] with respect to wind tunnel data. μ is the mean error and σ is the standard deviation.

Case	ΔM_x and Gill prop			Pure stability derivs.		
	RMSE	μ	σ	RMSE	μ	σ
F_x [N]	2.6	0.80	2.4	10	9.6	4.3
F_z [N]	4.1	-3.4	2.3	3.3	-2.4	2.3
M_x [Nm]	0.31	-0.13	0.28	0.70	-0.31	0.63
M_y [Nm]	0.77	0.44	0.64	0.91	0.37	0.84
M_z [Nm]	0.36	-0.090	0.35	0.51	0.44	0.26

Similar to section III-B, further discussion of the simulation will be limited to the roll moment, as it is the primary focus of this study.

Figure 10 shows the roll moment as a function of b_2 and b_3 at an airspeed of nine meters per second. Clearly, the inclusion of the error correction polynomial and the new propeller model resulted in a closer fit to the wind tunnel data. Additionally, the greater effectiveness of the rear rotors (b_3) in producing a roll moment is captured by the inclusion of ΔM_x.
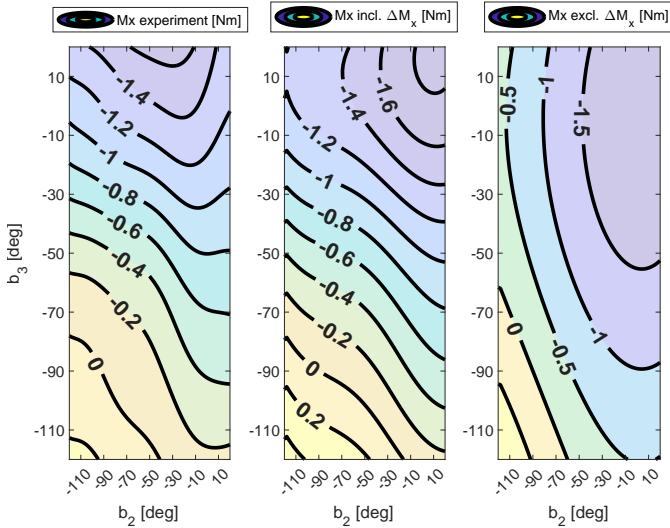
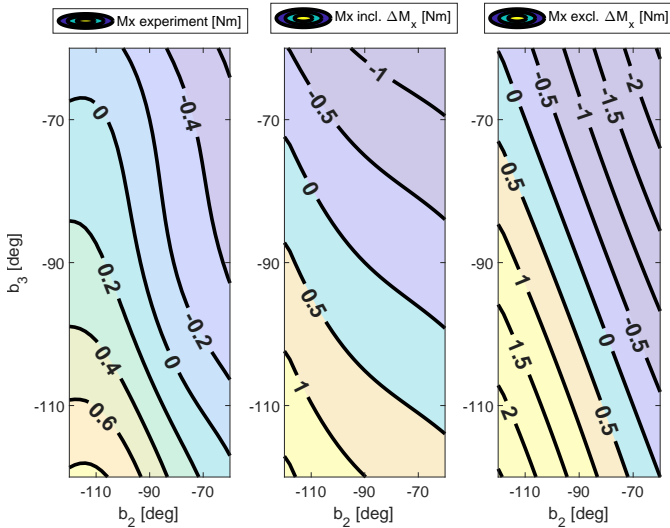**Figure 10:** Comparison between polynomial fit of experimental data, new aero-propulsive model and old model at V=9m/s and $\Omega = 600$ rad/s.

Nonetheless, there are still has some considerable errors, as shown in Figure 11. The worst mismatch between wind tunnel data and the new model occurs when the inflow angle of the front and rear rotors are larger than ninety degrees. This is expected, as the propellers experience inflow from behind the propeller disk in this region, which likely has a highly nonlinear effect on their performance. Despite this shortcoming, there is

still a much larger low error region compared to purely using stability derivatives.
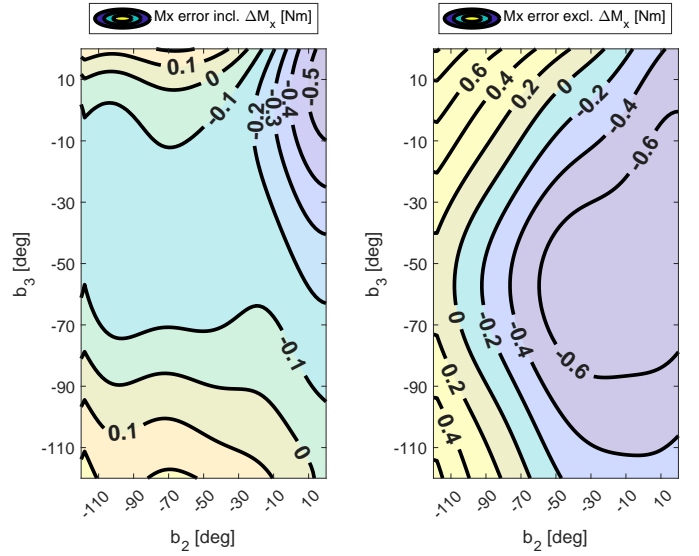
Figure 11: New and old aero-propulsive model error at V=9m/s and $\Omega = 600$ rad/s, compared to the unshortened polynomial fit of the experimental data

Figure 12 shows the case in which the drone is flying at nine meters per second and the propellers are operating at maximum power. While the errors in the new model are still smaller than those of the original model, it is clear that even the model including ΔM_x fails to capture some nonlinearity exhibited by the experimental data.
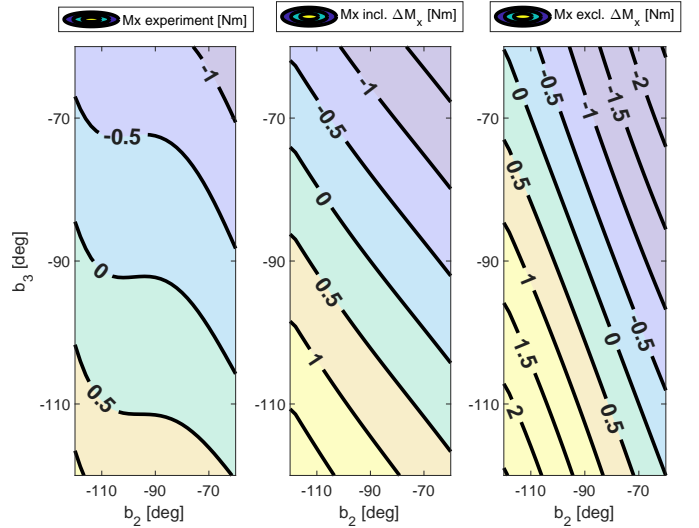
Figure 12: Comparison between polynomial fit of experimental data, new aero-propulsive model and old model at V=9m/s and $\Omega = 1000$ rad/s

Once again, the regions of largest errors lie at the edges of the domain, as shown in Figure 13. Due to the limitations experienced during the wind tunnel test as mentioned in section II-E, only a small region of the total tilt mechanism envelope was covered for high RPM operations. Based on the experience with Figure 11, it is reasonable to assume that the error will only grow in the region beyond in which data was gathered. Therefore, it is likely that the difference polynomials

misrepresent reality for high RPM and large elevation angles given the current data.
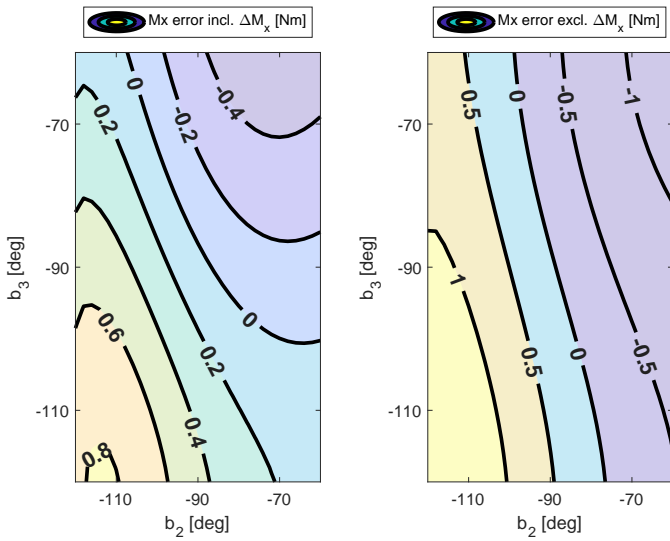
Figure 13: New and old aero-propulsive model error at V=9m/s and $\Omega = 1000$ rad/s, compared to the unshortened polynomial fit of the experimental data

Figure 14 considers the case in which the drone is flying at fifteen meters per second and the motors are operating at maximum RPM. The outcome is similar as before, the model fails to capture some of the nonlinearity. However, compared to the previous case, the error grows much quicker in the direction of rear propeller elevation (b_3) as shown in Figure 15.

Figure 14: Comparison between polynomial fit of experimental data, new aero-propulsive model and old model at V=15m/s and $\Omega = 1000$ rad/s

Overall, the global roll error correction polynomial reduces the difference between simulated and measured roll moments. Yet, in some cases the error remains substantial and due to the higher order nature of the polynomials the error might grow even faster outside the bounds in which wind tunnel testing was conducted.

E. Flight Test Analysis

The goal of the flight tests is to prove that the quad-plane can fly in common conditions without the use of aerodynamic
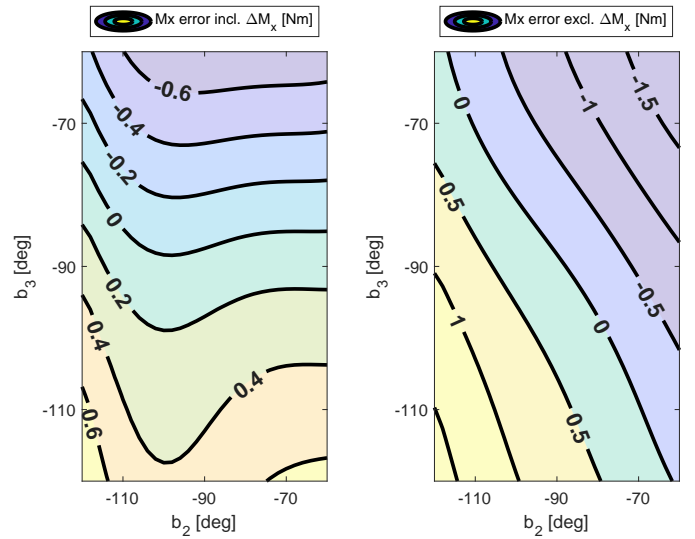
Figure 15: New and old aero-propulsive model error at V=15m/s and $\Omega = 1000$ rad/s, compared to the unshortened polynomial fit of the experimental data

surfaces. Three test flights were conducted. First a flight which included the roll moment correction polynomial and the propeller model developed by Gill et al. [12], however the drone was **not** allowed to use the ailerons. The second flight used the same controller, but the drone **was** allowed to use the ailerons. Finally, the same track was flown with the original model containing **neither** the error correction polynomials **nor** Gill's propeller model. The quad-plane was also allowed to use the ailerons during the last flight.

All flight tests followed the same circuit, consisting of four waypoints to form a figure 8, as shown in Figure 16. Additionally, the drone had to track a constant airspeed of fifteen meters per second. The flight using the roll moment corrections without the ailerons shows some oscillations around the reference trajectory, mostly in the segment p1-p2. However, it should be noted that the wind was quite strong on the day of testing, and the quad-plane experienced cross winds in segment p1-p2. An estimate of the forward component of the wind can be seen in Figure 17. Taking the wind into consideration, the quad-plane tracked the figure 8 adequately.

1) Flight Path and Attitude Tracking

Through visual inspection of the flight path, it was already noted in the previous section that the flight not using ailerons showed some additional oscillations. To further compare the accuracy with which the drone tracks the circuit, a comparison between desired and actual XY-accelerations in the control reference frame can be made. Figure 18 shows very similar XY-acceleration tracking for all models using ailerons. However, when the drone is not using ailerons, a slight increase in lateral acceleration error is observed. This is visible at 4 and 16 seconds into the figure 8 maneuver, respectively. The flight in which no ailerons were used had the highest tracking error, as observed in Table VII.

In addition to the linear acceleration, it is important to assess the attitude tracking of the drone with the model additions. Figure 19 shows the roll and pitch angle data collected throughout the flight tests. At a first glance, pitch angle tracking is similar between all models. This is further confirmed by the RMSE given in Table VII. More importantly,

Figure 16: Flown path comparison of different models for one round of the figure 8 circuit.
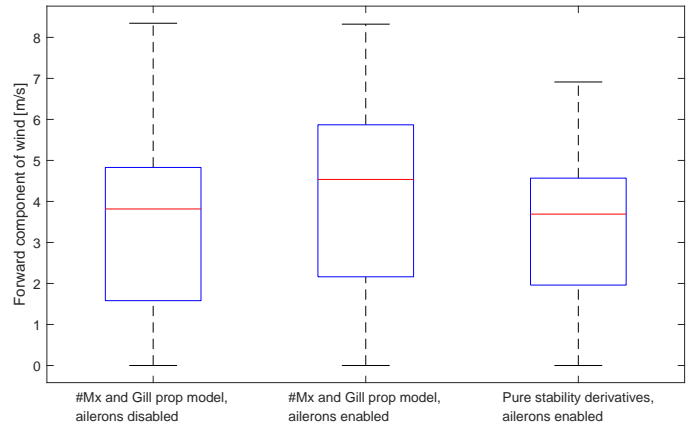

Figure 17: Absolute value of estimated wind speeds during each of the test flights.

in Table VII.

On average, the quad-plane flew slower than the desired fifteen meters per second, regardless of the model used in control. The new model tracked airspeed slightly better, with a mean airspeed of 14.4 meters per second in both cases, and the original configuration with an average of 14.2 meters per second. Though, the RMSE are almost equal as shown in Table VII. The measured airspeed, wind speed and ground speed can be seen in Figure 20.

Table VII: Flight path and attitude tracking RMSE during figure 8 circuit.

	Incl. ΔM_x ailerons disabled	Incl. ΔM_x ailerons enabled	Original
X-acc [m/s^2]	1.38	1.10	1.15
Y-acc [m/s^2]	1.44	0.75	0.96
θ [deg]	1.8	1.8	1.4
ϕ [deg]	12.7	6.5	10.3
V [m/s]	1.0	0.9	1.1

2) Actuator Commands

Intuitively, not using the ailerons requires more frequent deflections of the propellers, which can be seen in Figure 21. Compared to the other test flights, the propellers were deflected to a much higher degree, even leading to some saturation. This saturation is most noticeable at four seconds in to the flight, and aligns with a worsening of the lateral acceleration tracking, as mentioned in the previous section.

Besides the short spike at 37 seconds, the elevation of the propellers remains much more limited in both cases where the quad-plane is allowed to use the ailerons. Additionally, the changes to the cost function mentioned in section II-G appear to lead to a more independent tilting of the rotors compared to the original.

No significant differences were observed in the desired motor speeds commands given during the different flights, as shown in Figure 22. There are a few fluctuations in the commanded motor speed towards the end of the figure 8 when the use of ailerons is prohibited, the reason of which is the issue with the angle of attack estimation mentioned in the previous section.

3) Impact on Computational Time

Finally, the impact of the error correction polynomials and more complex propeller model on the computational requirements of the control allocation algorithm can be assessed.

the worst roll angle tracking was observed in the case of no ailerons. This should be expected as the propellers are fully responsible for roll actions making them subject to saturation, whereas previously roll was fully delegated to the ailerons. The topic of actuator saturation will be further discussion in section III-E2. Additionally, at 53 seconds, a sharp change in reference roll angle is observed. This happens as a result of experiencing a (near) negative angle of attack during a turn. This is an issue with the angle of attack estimation and should be investigated. If this artifact is removed, the RMSE across the flight test would decrease to 9.9 degrees, which would put it on par with the original model using ailerons. It should also be noted that the new model performed significantly better in tracking the roll angle when allowed to use ailerons, as shown

Figure 18: X- and Y-acceleration tracking of all models for one round of the figure 8 circuit.

To preface this discussion, it should be mentioned that the control allocation onboard the drone is performed in C, however the cost function is first derived in Matlab and subsequently converted to C code using the Matlab Coder[2] library. The process in which the cost function is derived was improved, resulting in fewer repeated computations in the new model. However, this optimization was not implemented for the original model, making a direct comparison unfair. The addition of equations to the model certainly contributes extra terms to the cost function, which means that in a fair environment, computation cost would also be increased.

In all cases the constraints imposed on the control allocation were equal, namely a time limit of 0.005 seconds, maximum number of cost function evaluations of 1000 and a maximum number of iterations of 200. Where an iteration occurs when the solver chooses a new point to evaluate. Table VIII gives an overview of the controller performance during the test flight. It is obvious that the time constraint is the dominant factor in terminating the optimization. Only in the case where no ailerons were used did the control allocation manage to have a slightly higher average frequency than the absolute minimum of 200 Hertz. It also had the largest amount of iterations and

function evaluations. A more direct comparison can be made between the original model and the case in which the new model is allowed to use ailerons, as both are limited by the time constraint. On average, the original model achieved 6.0% more function evaluations. Although the new model computes slower than the original when ailerons are activated, the penalty in performance is not significant enough to hinder control of the quad-plane.

Table VIII: Controller statistics

	Incl. ΔM_x ailerons disabled	Incl. ΔM_x ailerons enabled	Original
Mean freq. [Hz]	208	200	200
Mean func. evals	200	167	177
Mean iterations	95	79	88

IV. CONCLUSIONS

This paper highlights the importance of characterizing the propeller-wing interactions in vehicles using tilting rotors as the sole means of control. In the case of the dual-axis tilting rotor quad-plane designed by Mancinelli et al., wind tunnel testing showed that the propeller-wing interactions caused the front rotors to generate a two to four times weaker roll
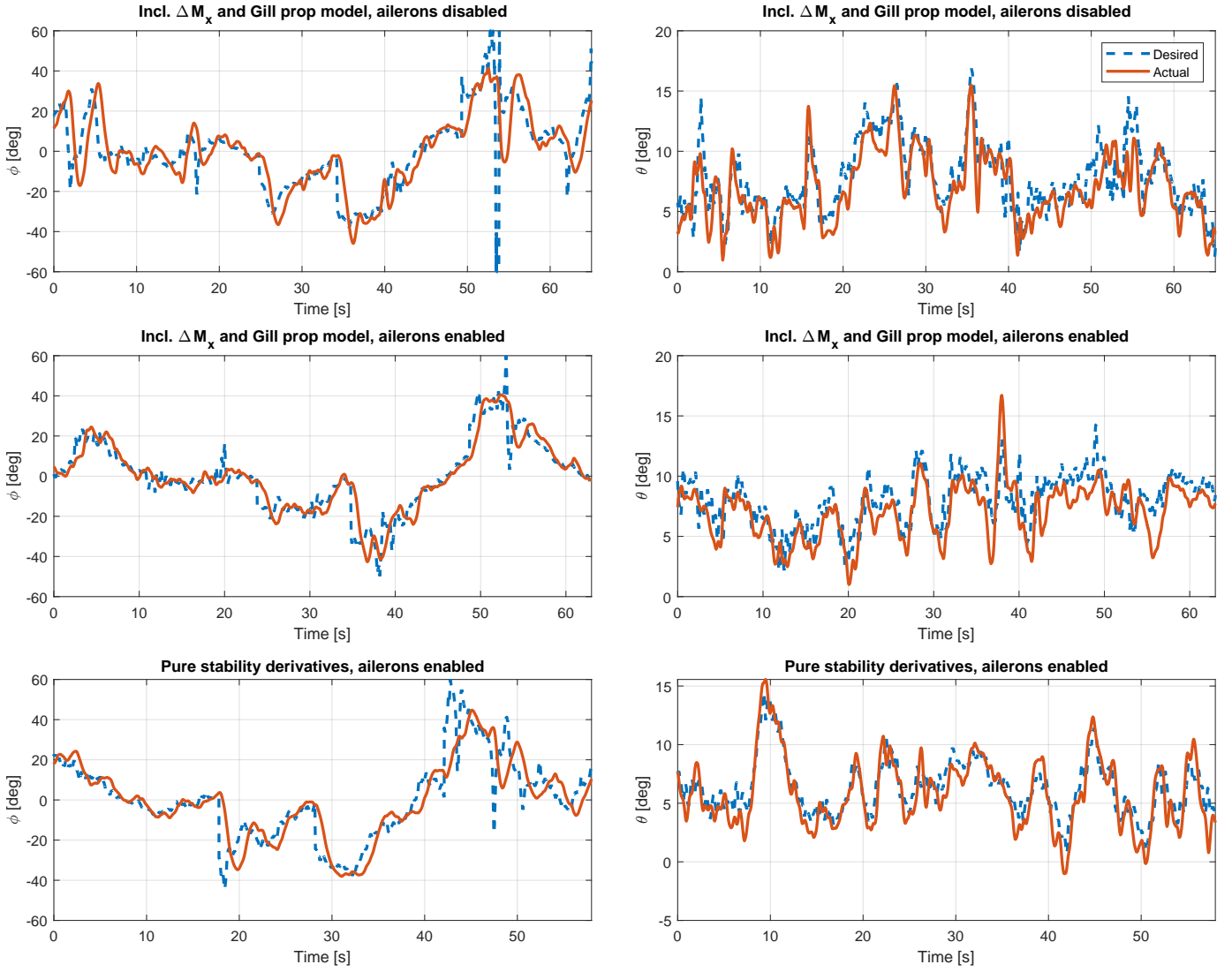
Figure 19: Roll and pitch angle tracking during figure 8 circuit of all models.

moment compared to an equal tilt of the rear rotors. The control allocation algorithm was not aware of this, preventing the drone from performing certain maneuvers in its aerodynamic-surface-free configuration.

By including the propeller-wing interactions in the new aero-propulsive model, the drone was able to track a figure 8 maneuver without ailerons. A small decrease in lateral acceleration and roll angle tracking accuracy was observed when compared to the flights using ailerons, but this decrease in accuracy was not significant enough to hinder operations. However, saturation of the tilt mechanism was observed, which could be a concern in certain circumstances, such as heavy gusts.

Propeller-wing interactions were approximated by a global polynomial obtained through multivariate orthogonal function (MOF) modelling. Although the global error-correction polynomials fulfilled their intended purpose of granting the drone the ability to fly without the use of ailerons, they still lack in accuracy due to their global nature. Additionally, it was difficult to obtain a set of polynomials which extrapolated well over the entire flight envelope and actuator space.

Future research efforts could be directed at investigating the influence of the relative position between the wing and front rotors to minimize or even benefit from the effect of the propeller-wing interactions.

REFERENCES

[1] Alwin Wang. "Conceptual Design of a QuadPlane Hybrid Unmanned Aerial Vehicle". In: Nov. 2017. DOI: 10.13140/RG.2.2.23090.84163.

[2] Alessandro Mancinelli et al. "Dual-axis tilting rotor quad-plane design, simulation, flight and performance comparison with a conventional quad-plane design". In: *2022 International Conference on Unmanned Aircraft Systems, ICUAS 2022*. United States: Institute of Electrical and Electronics Engineers (IEEE), 2022, pp. 197–206. DOI: 10.1109/ICUAS54217.2022.9836063.

[3] Alessandro Mancinelli et al. "Real-Time Nonlinear Control Allocation Framework for Vehicles with Highly Nonlinear Effectors Subject to Saturation". In: *Journal of Intelligent & Robotic Systems* 108 (July 2023). DOI: 10.1007/s10846-023-01865-8.

[4] S. Sieberling, Q. P. Chu, and J. A. Mulder. "Robust Flight Control Using Incremental Nonlinear Dynamic Inversion and Angular Acceleration Prediction". In:
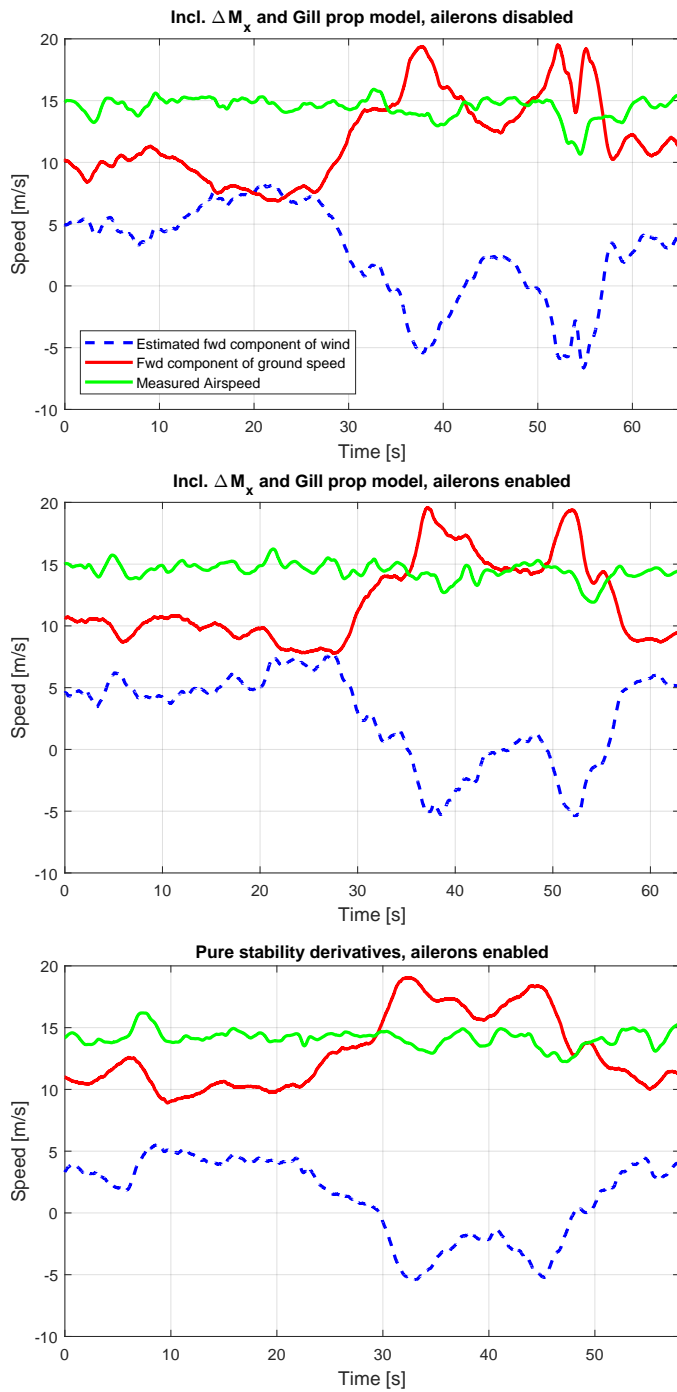
Figure 20: Airspeed tracking during figure 8 circuit for all models.
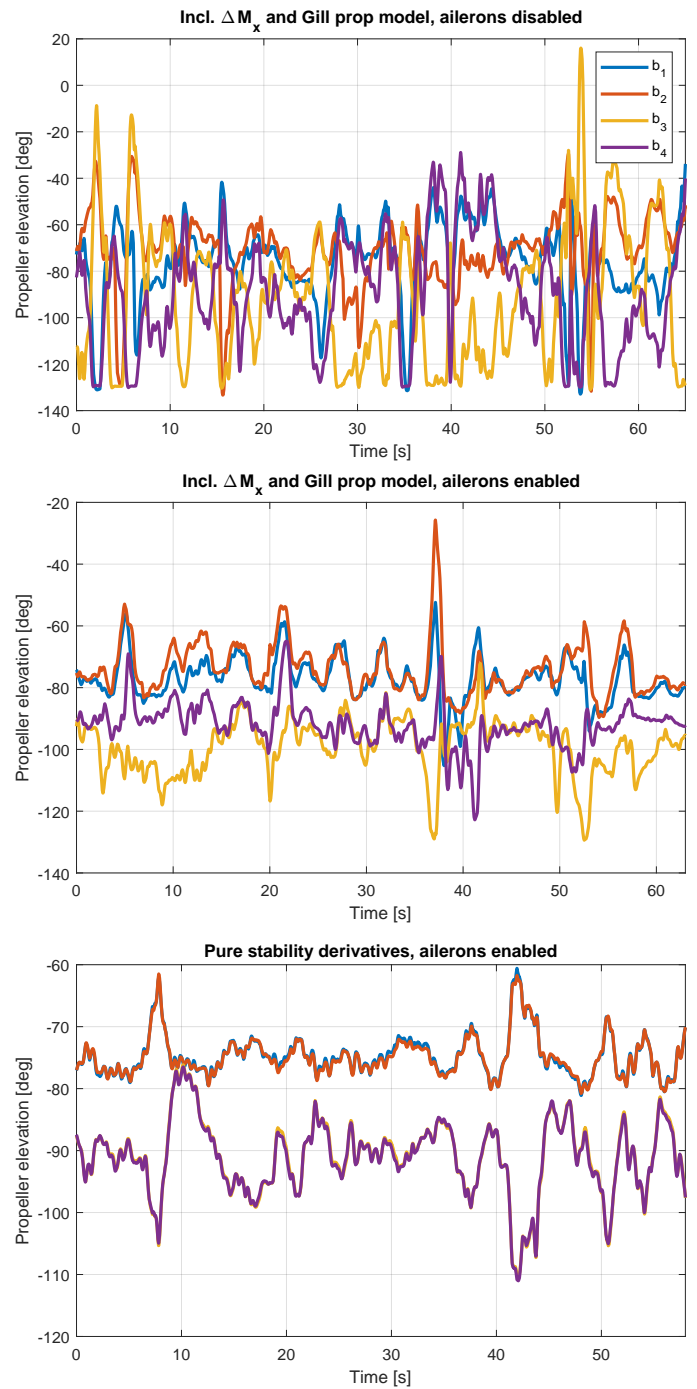
Figure 21: Propeller elevation states during figure 8 circuit for all models. With b_1 being the front left propeller, b_2 the front right, b_3 the rear right and b_4 the rear left propeller.

Journal of Guidance, Control, and Dynamics 33.6 (2010), pp. 1732–1742. DOI: 10.2514/1.49978. URL: https://doi.org/10.2514/1.49978.

[5] Ewoud J.J. Smeur, Guido C.H.E. de Croon, and Qiping Chu. "Gust disturbance alleviation with Incremental Nonlinear Dynamic Inversion". In: *2016 IEEE/RSJ International Conference on Intelligent Robots and Systems (IROS)*. 2016, pp. 5626–5631. DOI: 10.1109/IROS.2016.7759827.

[6] M.Z. Mimouni et al. "A new control scheme for an aerodynamic-surface-free tilt-rotor convertible UAV". In: *The Aeronautical Journal* (2023), pp. 1–26. DOI: 10.1017/aer.2023.90.

[7] Norman S. Nise. *Control Systems Engineering*. Eighth. Hoboken, NJ: Wiley, 2019. ISBN: 978-1-119-59013-2.

[8] B. Theys et al. "Experimental and Numerical Study of Micro-Aerial-Vehicle Propeller Performance in Oblique Flow". In: *Journal of Aircraft* 54.3 (2017), pp. 1076–1084. DOI: 10.2514/1.C033618.

[9] Rafael L. Rubin and Dan Zhao. "New Development of Classical Actuator Disk Model for Propellers at Incidence". In: *AIAA Journal* 59.3 (2021), pp. 1040–1054. DOI: 10.2514/1.J059734.
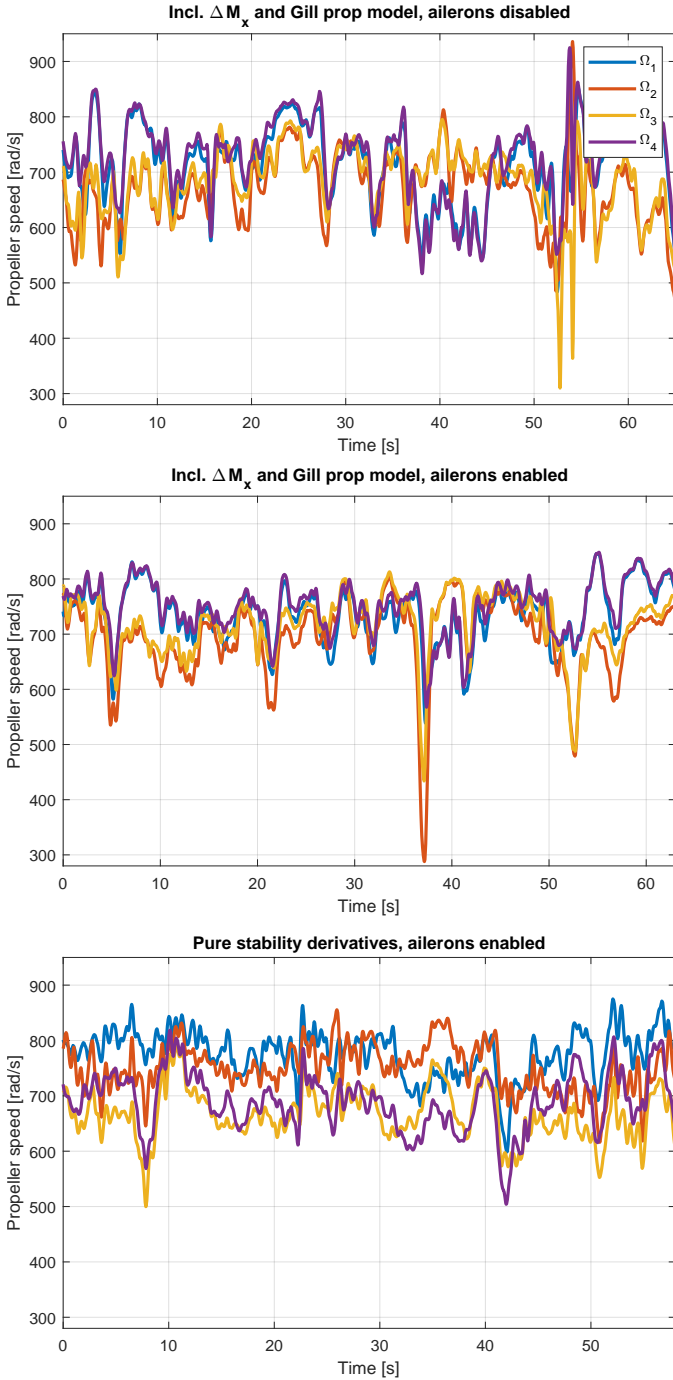
Figure 22: Motor speed states during figure 8 circuit for all models.

[10] Yuchen Leng et al. "Aerodynamic Modeling of Propeller Forces and Moments at High Angle of Incidence". In: *AIAA Scitech 2019 Forum*. DOI: 10.2514/6.2019-1332.

[11] Ege Konuk and Drew Landman. "Computer Based Modeling for Tilt-Wing e-VTOL Propeller Performance". In: *AIAA SCITECH 2023 Forum*. DOI: 10.2514/6.2023-0339.

[12] Rajan Gill and Raffaello D'Andrea. "Computationally Efficient Force and Moment Models for Propellers in UAV Forward Flight Applications". In: *Drones* 3.4 (2019). ISSN: 2504-446X. DOI: 10.3390/drones3040077.

[13] Luiz F. Fernandez et al. "Assessment of Methods for Propeller Performance Calculation at High Incidence

Angles". In: *AIAA SCITECH 2023 Forum*. DOI: 10.2514/6.2023-2283.

[14] Benjamin M. Simmons. "System Identification for Propellers at High Incidence Angles". In: *Journal of Aircraft* 58.6 (2021), pp. 1336–1350. DOI: 10.2514/1.C036329.

[15] Haitao Yang et al. "Aerodynamic performance of a small-scale tilt rotor: Numerical simulation and experiment in steady state". In: *Proceedings of the Institution of Mechanical Engineers, Part C: Journal of Mechanical Engineering Science* (2020). DOI: 10.1177/0954406220950352.

[16] Michael Selig. "Modeling Propeller Aerodynamics and Slipstream Effects on Small UAVs in Realtime". In: *AIAA Atmospheric Flight Mechanics Conference*. DOI: 10.2514/6.2010-7938.

[17] John T. Conway. "Analytical solutions for the actuator disk with variable radial distribution of load". In: *Journal of Fluid Mechanics* 297 (1995), pp. 327–355. DOI: 10.1017/S0022112095003120.

[18] Yuchen Leng et al. "Comparisons of Different Propeller Wake Models for a Propeller-Wing Combination". In: *8th European Conference for Aeronautics and Space Sciences*. Madrid, Spain, July 2019. URL: https://hal.science/hal-03385864.

[19] Eugene Morelli. "Efficient Global Aerodynamic Modeling from Flight Data". In: *50th AIAA Aerospace Sciences Meeting including the New Horizons Forum and Aerospace Exposition*. DOI: 10.2514/6.2012-1050.

[20] Eugene A. Morelli. "Real-Time Global Nonlinear Aerodynamic Modeling for Learn-To-Fly". In: *AIAA Atmospheric Flight Mechanics Conference*. DOI: 10.2514/6.2016-2010. URL: https://arc.aiaa.org/doi/abs/10.2514/6.2016-2010.

[21] Eugene A Morelli. "Practical aspects of real-time modeling for the learn-to-fly concept". In: *2018 Atmospheric Flight Mechanics Conference*. 2018, p. 3309.

APPENDIX

GENERALIZATION OF ERROR CORRECTION POLYNOMIALS

Similarly to the roll moment coefficient, the pitch, and yaw correction coefficients can be expressed as functions of Ω, V and the propeller elevation:

$$\begin{bmatrix} \Delta C_{Mx} \\ \Delta C_{My} \\ \Delta C_{Mz} \end{bmatrix} = f\left(\Omega_{1\text{-}2}, V, b_{1\text{-}4}\right). \tag{54}$$

These coefficients are then related to the moment coefficients using the following expression:

$$\begin{bmatrix} \Delta M_x \\ \Delta M_y \\ \Delta M_z \end{bmatrix} = \begin{bmatrix} \frac{1}{2}\rho V^2 Sb\Delta C_{Mx} \\ \frac{1}{2}\rho V^2 Sc\Delta C_{My} \\ \frac{1}{2}\rho V^2 Sb\Delta C_{Mz} \end{bmatrix}, \tag{55}$$

where c is the mean aerodynamic chord. The moment coefficients due to a tilt of the right hand side propellers are once again obtained by subtracting the moment measurements of the wingless quad-plane from the moment measurements of the full quad-plane:

$$\begin{bmatrix} \Delta C_{Mx}\left(\Omega_{1\text{-}4}, V, b_{1\text{-}4}\right) \\ \Delta C_{My}\left(\Omega_{1\text{-}4}, V, b_{1\text{-}4}\right) \\ \Delta C_{Mz}\left(\Omega_{1\text{-}4}, V, b_{1\text{-}4}\right) \end{bmatrix} = \begin{bmatrix} C_{Mx_{\text{wing}}} - C_{Mx_{\text{wingless}}} \\ C_{My_{\text{wing}}} - C_{My_{\text{wingless}}} \\ C_{Mz_{\text{wing}}} - C_{Mz_{\text{wingless}}} \end{bmatrix}, \tag{56}$$

which can be incorporated into the moment equations as follows:

$$^{b}\boldsymbol{M}_{a,\text{new}} = {}^{b}\boldsymbol{M}_{a} + \frac{1}{2}\rho V^{2} S \begin{bmatrix} b\Delta C_{M_{x}} \\ c\Delta C_{M_{y}} \\ b\Delta C_{M_{z}} \end{bmatrix}. \qquad (57)$$

The pitch and yaw tracking was already sufficient prior to adding the error correction coefficients and including them would consume unnecessary computational resources, hence they were excluded from the controller. The pitch and yaw coefficients were however included in simulation, but did not significantly increase the accuracy of the model, as shown in Table VI.

Part II

Literature Study

2

Summary

Mancinelli et al. recently designed a dual-axis tilting rotor quad-plane, which offers new possibilities in the realm of disturbance rejection and dynamic maneuverability [1]. The quad-plane features four propellers which can be tilted along elevation and azimuth, giving the vehicle the capability to hover and fly efficiently. However, the current aerodynamic model is still lacking in certain areas, which hampers the vehicle's ability to perform certain maneuvers within the flight envelope.

Due to the tilting rotors, the quad-plane should have control over all 6 degrees of freedom. However, during flight tests, it was observed that the vehicle could not successfully roll by tilting the propellers in fast, forward flight. It was hypothesized that the downwash acting on the wing due to the propellers was countering the roll moment introduced by tilting the propellers. Therefore, this research aims to create a more accurate aero-propulsive model, covering the full flight envelope of the vehicle. Where much focus will be placed on understanding the complex aerodynamic interactions between the propulsion system and the airframe.

The main difficulty in modelling the quad-plane's aerodynamics is the large sideslip angles which regularly occur during operation. All methods outlined in Chapter 5 including, small perturbation theory, the polynomial like model derived by Lustosa et al. [2], lifting line theory (LLT) and vortex lattice methods (VLM) are capable of modelling the desired sideslip effects. However, they go about it in different ways. Small perturbation theory and Lustosa's model fit parameters based on experimental or theoretical data. On the other hand, LLT and VLM use the wing shape and flow properties to determine the forces acting on the vehicle. LLT is not guaranteed to run in real time, and VLM cannot run in real time. Realistically, this leaves only the former type of model as a viable option. As a result, the current small perturbation based model was deemed sufficient, given its simplicity and flexibility.

Out of all methods related to propulsive modelling covered in Chapter 6, only analytical models and models based on system identification are capable of running in real time. The comparison by Fernandez showed that the analytical model derived by Gill et al. [3] is the most accurate among the analytical models [4]. Furthermore, the model by Gill can be supplemented with experimental data to increase the accuracy.

Correct modelling of propeller-wing interactions are likely the key to resolve the issues related to insufficient roll authority during fast, forward flight. Dynamic inflow provides many advantages over other methods, such as VLM and actuator disc theory. Namely, the model can be extended to be a combined inflow and wake model for the propellers. This makes the dynamic inflow attractive in the sense that it can be applied in two separate areas of the model. Additionally, dynamic inflow is capable of handling systems in which propellers operate inside a slipstream [5, 6], and it is comparatively computationally efficient. However, dynamic inflow has not been validated on a tilt-rotor UAV, as such a wind tunnel experiment would have to be conducted to validate the resulting model. However, the wind tunnel data could also be used to directly identify a propeller-wing interactions model.

To bring all the separate pieces together, and keeping the aforementioned points in mind, the model will consist of the following elements. First, the small perturbation based aerodynamic model will remain in place, as the model is flexible enough for the current use-case. The current static propeller model will be replaced by Gill's propeller model [3], as it consists of computationally cheap expressions while also taking into account the inflow angle. Finally, the propeller-wing interactions will be derived by means of a wind tunnel experiment, as all the models found in the literature contained several drawbacks.

It is clear that wind tunnel experiments are necessary to gather missing data for the model. To this extent, it is beneficial to employ modern design of experiment (MDOE) methods, as they improve the information contained within the captured data. This means that more information can be captured in fewer runs, which reduces the time spent using expensive resources such as a wind tunnel test facility. Space-filling designs are being considered as they allow for good coverage of the flight envelope, while keeping the number of test cases limited.

List of Figures

List of Tables

Nomenclature

List of Abbreviations

BEMT Blade Element Momentum Theory

CCD Central Composite Design

CFD Computational Fluid Dynamics

DOE Design of Experiment

DOF Degree of Freedom

EOM Equations of Motion

GNC Guidance, Navigation and Control

LE Leading Edge

LLT Lifting Line Theory

MDOE Modern Design of Experiment

MOF Multivariate Orthogonal Function

OFAT One Factor At a Time

PCB Printed Circuit Board

RMSE Root mean square error

RPF Relative Peak Factor

TE Trailing Edge

UAV Unmanned Aerial Vehicle

VLM Vortex Lattice Method

VTOL Vertical Take-off and Landing

List of Symbols

α Angle of attack

β Angle of sideslip

Ω Propeller Angular velocity

ω Angular velocity

ϕ Roll angle

ψ Yaw angle

τ 6-DOF wrench

θ Pitch angle

p Roll rate

q Pitch rate

r Yaw rate

u Forward velocity component

v Sideways velocity component

w Vertical velocity component

ϵ Error matrix

λ Tip speed ratio

λ Total inflow through the rotor

$[L]$ Inflow gain matrix

$[M]$ Apparent mass matrix

ϕ Phase component

Ψ Propeller azimuth angle

ρ Density

Σ Covariance matrix

σ Standard deviation

A Area

D Drag

i_p Angle of incidence

J Advance Ratio

J Cost function

L Lift

m Mass

N Number of samples

p Multivariate Orthogonal function

R Propeller radius

r Radial coordinate

Re Reynold number

T Period

T Thrust

V Velocity

V_∞ Freestream velocity

3

Introduction Literature Study

Mancinelli et al. recently designed a novel dual-axis tilting rotor quad-plane, which offers new possibilities in the realm of disturbance rejection and dynamic maneuverability [1]. The quad-plane features four propellers which can be tilted along elevation and azimuth, giving the vehicle the capability to hover and fly forward efficiently. This configuration gives the vehicle independent control of all six degrees of freedom. In forward flight, the vehicle is capable of achieving speeds up to twenty meters per second. Additionally, the vehicle is capable of lateral flight up to five meters per second and backwards flight up to five meters per second. However, the current aerodynamic model is still lacking in certain areas, which hampers the vehicle's ability to perform certain maneuvers within the flight envelope.

Figure 3.1: Picture of the quad-plane.

Due to the tilting rotors, the quad-plane should have independent control over all six degrees of freedom. However, during flight tests it was observed that the vehicle could not successfully roll by tilting the propellers in fast, forward flight. It was hypothesized that the downwash acting on the wing due to the propellers was counteracting the roll moment introduced by tilting the propellers. Therefore, the goal of this research is to get a better understanding of these effects:

Research Objective

This research aims to create a more accurate aero-propulsive model, covering the full flight envelope of the vehicle. Therefore, much focus will be placed on understanding the complex aerodynamic interactions between the propulsion system and the airframe. The new aero-propulsive model will enable more accurate simulation as well as supporting the guidance and control algorithms currently employed on the system.

The first step in establishing a new model is to conduct a literature review on the current state-of-the-art in aero-propulsive modelling. To fulfill the research objective, the literature review should answer the following four questions:

Research Question 1

What methods are best suited for full-envelope aerodynamic modelling?

Research Question 2

What methods are best suited for propulsive modelling of propellers?

Research Question 3

What methods are best suited for modelling propeller-wing interactions?

Research Question 4

How can the aerodynamic and propulsive model be combined into a global aero-propulsive model?

To this end, Chapter 4 will define common definitions in aerodynamics, analyze the current model, and develop criteria which help in answering the research questions. Subsequently, Chapter 5 will give an overview of modern aerodynamic modelling. Chapter 6 and Chapter 7 will cover propulsive modelling and propeller-wing interactions, respectively. Chapter 8 will elaborate on some concepts and combine what was previously investigated to form a combined global aero-propulsive model. Modern designs of experiments will be treated in Chapter 9, as there is a need for wind tunnel experiments. The research which will follow this literature review will be outlined in Chapter 10. Finally, conclusions will be drawn in Chapter 11.

4

Background Information

4.1. Definitions and Coordinate Frames

For the analysis of the aerodynamics and propulsion system, it is practical to define a set of coordinate frames and definitions which will be used consistently throughout the literature review. The coordinate systems which will be used in this report are all right-handed and were previously defined by Mancinelli et al. as shown in Figure 4.1. Here, the superscript e refers to the inertial frame, b to the body frame and p is the propeller frame.

Figure 4.1: Overview of the Earth, Body, and Propeller frames (taken from [1]).

Due to the nature of the design, the quad-plane will remain in a regime in which the surrounding air is

incompressible. This is the case when the mach number is smaller than 0.3. The mach number is defined by Equation 4.1, where c is the speed of sound.

Definition (Incompressible flow). A flow in which the density ρ is constant [7].

$$M = \frac{V}{c} \tag{4.1}$$

Generally, aerodynamic properties are a function of the Reynolds number, as defined by Equation 4.2. Where μ is the dynamic viscosity and l is the characteristic length. The Reynolds number is a measure of the ratio of inertia forces to viscous forces in a flow [7].

$$Re = \frac{\rho V_\infty l}{\mu} \tag{4.2}$$

The quad-plane and its propellers generally operate at relatively low Reynolds numbers, which means that viscous effects dominate the aerodynamics. However, unless stated otherwise, the models in question will consider the flow to be steady and inviscid.

Definition (Steady flow). A flow that does not change over time [7].

Definition (Inviscid flow). A flow that is assumed to involve no friction, thermal conduction, or diffusion [7].

Other important quantities which for aerodynamic analysis are the angle of attack α and angle of sideslip β, defined by Equation 4.3 and Equation 4.4 respectively. Where the velocities are defined in the body frame.

$$\alpha = \arctan\left(\frac{^bV_{\infty,z}}{^bV_{\infty,x}}\right) \tag{4.3} \qquad \beta = \arcsin\left(\frac{^bV_{\infty,y}}{^bV_\infty}\right) \tag{4.4}$$

Similarly, a number of convention can be established for the analysis of the propellers. Figure 4.2 defines the forces and moments as they will be evaluated during propeller analysis. Here, the angle of incidence is defined as the angle between the propeller rotor plane and the incoming velocity V_∞, and is denoted by i_p.
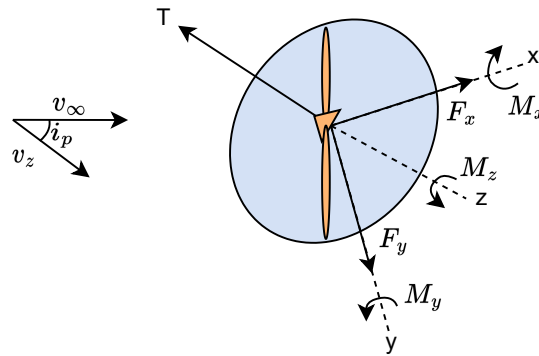

Figure 4.2: Propeller coordinate system, forces and moments, adapted from [8].

An important quantity in the analysis of propellers is the advance ration J. Propeller performance changes as a function of advance ratio, which is the ratio between the freestream velocity and the tip speed, as given by Equation 4.5.

$$J = \frac{V_\infty}{nD} \tag{4.5}$$

4.2. Flight Dynamics

The dynamics of a general rigid body system can be described by the following set of differential equations given in Equation 4.6 [2].

$$\begin{cases} \dot{\boldsymbol{v}}_b = \frac{1}{m} \sum \boldsymbol{F}_b + {}^b\boldsymbol{R}_e \boldsymbol{g}_e - \hat{\boldsymbol{\omega}}_b \boldsymbol{v}_b \\ \dot{\boldsymbol{\omega}}_b = J^{-1} \sum \boldsymbol{M}_b - J^{-1} \hat{\boldsymbol{\omega}}_b J \boldsymbol{\omega}_b \end{cases} \tag{4.6}$$

$\boldsymbol{v}_b \in \mathbb{R}^3$: linear velocity expressed in the body frame

$\boldsymbol{\omega}_b \in \mathbb{R}^3$: Angular velocity expressed in the body frame

$\sum \boldsymbol{F}_b \in \mathbb{R}^3$: Sum of all external forces expressed in the body frame

$\sum \boldsymbol{M}_b \in \mathbb{R}^3$: Sum of all external moments expressed in the body frame

${}^b\boldsymbol{R}_e \in \mathbb{SO}(3)$: Rotation matrix from inertial to body frame

$\boldsymbol{g}_e \in \mathbb{R}^3$: gravity vector in the inertial frame

$m \in \mathbb{R}_+$: mass of the system

$J \in \mathbb{R}^3$: Inertia matrix

Where $\hat{\boldsymbol{\omega}}_b$ is given by the following skew symmetric matrix:

$$\hat{\boldsymbol{\omega}} = \begin{bmatrix} 0 & -\omega_3 & \omega_2 \\ \omega_3 & 0 & -\omega_1 \\ -\omega_1 & \omega_1 & 0 \end{bmatrix} \tag{4.7}$$

The goal of aero-propulsive modelling is to find the relationship between the current state of the vehicle and the forces and moments acting on the vehicle.

$$\boldsymbol{\tau}_b = \begin{bmatrix} \sum \boldsymbol{F}_b \\ \sum \boldsymbol{M}_b \end{bmatrix} = f(\boldsymbol{x}, \boldsymbol{u}, t) \tag{4.8}$$

4.3. Current Model

The system outlined in Chapter 3 has already been flown, and a simulation has been established in previous efforts by Mancinelli et al. The simulation and current control allocation algorithm rely on the aero-propulsive model to supply the aerodynamic and propulsive forces acting on the vehicle.

4.3.1. Aerodynamic Model

The current aerodynamic model used for simulation is a simple decoupled model based on aerodynamic stability derivatives. This type of model is part of a larger group of models based on small perturbation theory, which will be discussed in Section 5.1. Equation 4.9 and Equation 4.10 show the relationship between the state variables and the aerodynamic forces and moments, respectively. The use of this kind of model is still widespread, which is likely attributed to its simplicity and reasonable accuracy.

$$\boldsymbol{F}_a = {}^e R_b \, {}^b R_w \frac{1}{2} \rho V_{tot}^2 S \begin{bmatrix} C_{D_0} + k_{cd} \left(C_{L_0} + C_{L_\alpha} \alpha \right)^2 \\ C_{Y_\beta} \beta \\ C_{L_0} + C_{L_\alpha} \alpha \end{bmatrix} \tag{4.9}$$

$$\boldsymbol{M}_b = \frac{1}{2} \rho V_{tot}^2 S \begin{bmatrix} b \left(C_{l_0} + C_{l_\beta} \beta + \frac{b}{2V_{tot}} \left(C_{l_p} p + C_{l_r} r \right) \right) \\ c \left(C_{m_0} + C_{m_\alpha} \alpha \right) \\ \frac{b^2}{2V_{tot}} \left(C_{n_p} p + C_{n_r} r \right) \end{bmatrix} \tag{4.10}$$

However, the current model suffers from some limitations. The first and most obvious limitation is that the forces and moments are modelled as a combination of linear functions. This does not pose a problem when the vehicle only experiences small excursions from the nominal flight condition, but for UAVs and agile aircraft with large flight envelopes, this linearity becomes a source of error. Although there are some regions of linearity, aerodynamics are inherently nonlinear.

The second issue is that the current model does not take any coupling into account. As an example, a large sideslip angle in combination with a nonzero roll angle will likely produce some vertical forces. However, the current model does not calculate the contributions of lateral flow to longitudinal forces and moments.

4.3.2. Propulsive Model

The current propulsive model used in the control allocation contains three terms related to the propeller forces and moments[1]. The first contribution is due to the propeller thrust, which is assumed to be perfectly aligned with the z-axis in the propeller frame. The choice of model is one based on a coefficient multiplied by the rotational velocity squared, as shown in Equation 4.11. The coefficient was determined through static bench tests.

$$\boldsymbol{F}_p = \sum_{i=1}^{N} {}^{e}R_b \, {}^{b}R_p^i \begin{bmatrix} 0 \\ 0 \\ -K_p^T \Omega_i^2 \end{bmatrix} \tag{4.11}$$

The thrust generated by the rotor gives rise to a moment about the center of mass of the vehicle. This moment can be found by taking the cross product between the thrust generated by the rotor and the position vector of each propeller in the body frame. This gives rise to Equation 4.12.

$$M_p^T = \sum_{i=1}^{N} \left({}^{b}R_p^i \begin{bmatrix} 0 \\ 0 \\ -K_p^T \Omega_i^2 \end{bmatrix} \right) \times \begin{bmatrix} l_x^i \\ l_y^i \\ l_z^i \end{bmatrix} \tag{4.12}$$

In addition to generating thrust, the rotor blades also experience drag, which causes a moment about the z-axis in the propeller frame. Staying consistent with the previous contributions, the moment due to rotor drag is modelled as a coefficient multiplied by the rotation velocity squared, as shown in Equation 4.13.

$$M_p^D = \sum_{i=1}^{N} - {}^{b}R_p^i \begin{bmatrix} 0 \\ 0 \\ K_p^M \Omega_i^2 \end{bmatrix} (-1)^i \tag{4.13}$$

All things considered, the current model is very simple, which gives rise to the following opportunities for improvements. First, because of the tilt-rotor nature, it is guaranteed that the rotors will experience inflow at incidence. To model the forces and moments more accurately, it is therefore necessary to include these effects. The effect of inflow is likely more involved than a simple dependence in the thrust coefficient. Currently, the in-plane forces caused by the propeller are neglected because thrust is assumed to be acting along the z-axis. However, when the propeller operates in non-axial flow, there will be in-plane forces which could have a significant effect on the system. Section 6.1 explores a more detailed model, which follows the same principles as the current model.

Additionally, the current model cannot predict the propeller slipstream, which is important in modelling propeller-wing interactions. In fact, the current model does not take any propeller-wing interactions into account. One of the main reasons for extended aerodynamic modelling of the current vehicle was outlined in Chapter 3. Namely, that tilting the rotors did not provide the expected result in inducing roll. It was hypothesized that propeller-wing interactions play an important role in understanding this phenomenon. Therefore, including propeller-wing interactions in the new model will play an important role in identifying the most important aerodynamic modes of this vehicle.

---

[1]There are additional terms due to precession and tilting of the rotors/vehicle, however these are not important for the current analysis

4.4. New Model Criteria

After identifying the shortcomings of the current model, it is possible to come up with a set of criteria, which should be adhered to in order to make the new model. By evaluating different modelling approaches using these criteria, it should be possible to answer the research questions outlined in Chapter 3. First, a set of general criteria can be identified which needs to be adhered to across all parts of the model:

1. The model should be able to handle nonlinearities.
2. The model should not contain any singularities inside the flight envelope.
3. The model should run in real time.
4. The method should not be iterative.

The first two general criteria should be strictly enforced. The model must be able to model nonlinearities in the global aerodynamics, and at no point inside the flight envelope should the model contain singularities. The third and fourth general criteria are not enforced as strictly. Ideally, the computation time should be short enough to supply the Guidance, Navigation, and Control (GNC) algorithms with the data they need. However, since it is possible to construct surrogate models, which can be evaluated in real time, the additional insights of higher order methods should be taken into account when choosing the final method. Additionally, the method should not be iterative, as the required steps to converge, and in turn also run time, can vary considerably under different conditions.

In addition to these general criteria, a set of criteria specific to each part of the model can be established:

1. RQ 1: Which methods are viable for full-envelope aerodynamic modelling?
   (a) General criteria mentioned above.
   (b) The aerodynamic model should accurately predict the vehicle's response to large sideslip angles.
2. RQ 2: Which methods are viable for full-envelope propulsive modelling of propellers?
   (a) General criteria mentioned above.
   (b) The model should be able to estimate all 6 components of the propulsive wrench.
   (c) The model should take the inflow angle into account.
3. RQ 3: Which methods are viable for modelling propeller-wing interaction?
   (a) General criteria mentioned above.
   (b) The model should be able to identify which portions of the wing are affected by the propeller wake.
   (c) The model should be able to identify the curvature of the wake.
   (d) The model should be able to take wing downwash into account.

5

Aerodynamic Modelling

This chapter covers the topic of aerodynamic modelling, with the focus being on wing modelling. In Section 4.3.1 it was established that the model currently employed is based on small perturbation theory. Section 5.1 will investigate whether this model is sufficiently accurate across the entire envelope. Subsequently, an alternate parameterization in the form of body velocities will be explained in Section 5.2. Following the discussion on coefficient based models, Section 5.3 will give an overview of the current state of Lifting Line methods. An extension of lifting line theory, namely the vortex lattice method, will then be discussed in Section 5.4. Finally, an approach based on strip theory will be discussed in Section 5.5.

5.1. Small Perturbation Theory

For flight dynamic analysis, the six degree of freedom equations of motion shown in Equation 4.6 are often linearized around a certain flight condition using small perturbation theory. These linearized equations are a function of certain derivatives which relate to the aerodynamics of the vehicle. Additionally, it is convenient to decouple the longitudinal and lateral equations. For general aviation aircraft, this model is accurate enough to capture the most dominant modes, making it a popular tool. However, this oversimplification of the aerodynamics may not be valid for some vehicles, such as the quad-plane in consideration.

Models based on small perturbation theory are essentially just polynomial functions. In essence, this means that instead of simplifying the model by neglecting terms, it is also possible to add any coupling terms. Furthermore, the model is not only limited to first order terms, it is possible to make a small perturbation model which contains terms up to an arbitrary degree. This gives this class of models extreme flexibility, however choosing a model structure is not always a trivial task. Therefore, Simmons et al. applied Multivariate orthogonal functions to automatically determine the model structure by discarding components which contribute below a certain threshold [9]. While this approach does alleviate the burden of having to find a suitable model structure, it does not guarantee that the model is accurate across the entire flight envelope. Aerodynamics are inherently complex, with regions of linearity and nonlinearity. It can become difficult for a single polynomial function to approximate the entire flight envelope.

5.1.1. Identifying the Model Structure

Ultimately, finding the correct set of functions is nearly impossible without full knowledge of the underlying physics. This means that finding a good model structure may involve many iterations and intuition. Therefore, Morelli describes a framework called Multivariate Orthogonal Function (MOF) modelling [10]. MOF modelling does not alleviate the need to supply the appropriate basis functions, but it is capable of automatically removing any unnecessary functions from the model. Morelli drops terms which contribute less than 0.1% of the total Root Mean Square Error (RMSE). Although MOF modelling was first introduced over a decade ago, the framework is still being used today, some examples are the recent work by Simmons et al. [9, 11].

The method described by Morelli solves a conventional least squares problem. The form of the model is given by Equation 5.1, where z are the response variables, a is the parameter vector, P are the orthogonal modelling functions and ϵ is the residual error.

$$z = Pa + \epsilon \tag{5.1}$$

33

The least squares cost function is then given by Equation 5.2.

$$J = \frac{1}{2}(z - Pa)^T (z - Pa) = \frac{1}{2}\epsilon^T \epsilon \tag{5.2}$$

Conventionally, the functions used in least-squares modelling are polynomials, which are not orthogonal functions by default [10]. This makes it difficult to estimate how each function affects the total result of the least squares outcome, because the covariance matrix is not diagonal. The covariance matrix can be estimated using Equation 5.3, where σ^2 is the variance.

$$\Sigma = \sigma^2 \left(P^T P\right)^{-1} \tag{5.3}$$

If the modeling functions are multivariate orthogonal functions, it is possible to decouple the least squares problem. Orthogonal functions have the property that only the trace of the $P^T P$ matrix is non-zero. In other words, $P^T P$ is a diagonal matrix:

$$p_i^T p_j = 0, i \neq j \tag{5.4}$$

The estimated parameter vector $\hat{a}$ can then be rewritten as Equation 5.5.

$$\hat{a}_j = \frac{p_j^T z}{p_j^T p_j} \tag{5.5}$$

The cost function can then be rewritten, keeping in mind the properties of the orthogonal functions, taking the form of Equation 5.6.

$$\hat{J} = \frac{1}{2}\left(z^T z - \sum_{j=1}^{n}\frac{\left(p_j^T z\right)^2}{p_j^T p_j}\right) \tag{5.6}$$

Now, the cost function using multivariate orthogonal functions depends only on the response variable data z and added orthogonal modelling function p_j.

5.1.2. Generating Orthogonal Functions

Morelli uses a Gram-Schmidt orthogonalization procedure to generate multivariate orthogonal functions from ordinary multivariate functions [10]. The first step is to generate a set of regular multivariate functions which can be for example polynomials up to a certain degree, splines, or a combination of both. The next step is to choose the first function which will serve as a basis for generating subsequent orthogonal functions. Generally, the bias can be chosen as the first orthogonal function:

$$p_1 = 1 \tag{5.7}$$

Each subsequent orthogonal function is then determined by Equation 5.8, where ξ_j is the jth regular multivariate function.

$$p_j = \xi_j - \sum_{k=1}^{j-1}\gamma_{kj}p_k, j = 2, 3, \ldots, n_t \tag{5.8}$$

The γ_{kj} terms are then determined by multiplying both sides with p_k^T and enforcing the orthogonality condition.

$$\gamma_{kj} = \frac{p_k^T \xi_j}{p_k^T p_k}, k = 1, 2, \ldots, j - 1 \tag{5.9}$$

If the vectors of $\boldsymbol{p}_j$ and $\boldsymbol{\xi}_j$ are arranged in the columns of matrices P and G respectively, then the orthogonal multivariate functions are related to the regular functions as shown in Equation 5.10.

$$\boldsymbol{P} = \boldsymbol{X}\boldsymbol{G}^{-1} \tag{5.10}$$

Where G is the upper triangular matrix consisting of the γ_{kj} terms:

$$G = \begin{bmatrix} 1 & \gamma_{12} & \gamma_{13} & \cdots & \gamma_{1n_t} \\ 0 & 1 & \gamma_{23} & \cdots & \gamma_{2n_t} \\ 0 & 0 & 1 & \cdots & \gamma_{3n_t} \\ \vdots & \vdots & \vdots & \vdots & \vdots \\ 0 & 0 & 0 & \cdots & 1 \end{bmatrix} \tag{5.11}$$

This way, a link can still be made between the orthogonal functions and the physically meaningful regular functions, which results in a simple procedure with few downsides. The procedure of generating the orthogonal functions is usually done offline, which means that computation time is not a real concern. Choosing the right explanatory variables and model order is now the only necessary step, as the MOF modelling procedure removes irrelevant terms on its own.

5.2. Velocity Parameterization

From the definitions of α and β in Section 4.1, it is clear that under certain conditions these quantities are undefined. The singularities occur when $V_{\infty,x}$ or V_∞ are zero for α, and β respectively, which is only seen in hovering flight. These near-zero divisions can lead to some numerical instabilities in simulations [2]. In reality, velocities will never be *exactly* zero, due to many factors such as wind, and inaccuracies in sensing equipment.

A potential solution to this problem is assigning specific values to α and β in the case that the vehicle is close to a singularity. May et al. chose for such an approach, where the definitions of α and β are given by Equation 5.12 and Equation 5.13 [12]. Unsurprisingly, Equation 5.12 is exactly the definition of the arctan2 function, which is still undefined when both u and w velocities are equal to zero. Therefore, the solution employed by May et al. does not solve the entire problem.

$$\alpha = \begin{cases} \arctan\left(\frac{V_{\infty,z}}{V_{\infty,x}}\right), V_{\infty,x} > 0 \\ \mathrm{sgn}\left(V_{\infty,z}\right)\pi + \arctan\left(\frac{V_{\infty,z}}{V_{\infty,x}}\right), V_{\infty,x} < 0, V_{\infty,z} \neq 0 \\ \pi, V_{\infty,x} < 0, V_{\infty,z} = 0 \\ \mathrm{sgn}\left(V_{\infty,x}\right)\frac{\pi}{2}, V_{\infty,z} = 0 \end{cases} \tag{5.12}$$

$$\beta = \begin{cases} \arcsin\left(\frac{V_{\infty,y}}{V_\infty}\right), \|\boldsymbol{V_\infty}\| > 0 \\ 0, \text{otherwise} \end{cases} \tag{5.13}$$

Alternatively, it is possible to completely circumvent the use of angle of attack and sideslip as explanatory variables when deriving the aerodynamic forces and moments. This alternate formulation defines the aerodynamic wrench as functions of the linear and angular velocities only. A model based on this approach was derived by Lustosa et al. [2]. The aerodynamic wrench as a function of body velocity is given in Equation 5.14.

$$\boldsymbol{\tau}_b = -\frac{1}{2}\rho S\eta C\Phi\left(\boldsymbol{\eta}_b\right)C\boldsymbol{\eta}_b \tag{5.14}$$

Where the C matrix relates to the dimensions of the wing, as given by Equation 5.15 and Equation 5.16.

$$C = \begin{bmatrix} I_{3x3} & 0_{3x3} \\ 0_{3x3} & B \end{bmatrix} \qquad (5.15) \qquad\qquad B = \begin{bmatrix} b & 0 & 0 \\ 0 & c & 0 \\ 0 & 0 & b \end{bmatrix} \qquad (5.16)$$

And the velocities are represented by Equation 5.17 and Equation 5.18.

$$\eta = \sqrt{V_\infty^2 + \phi\omega_\infty^2}, \quad \phi > 0 \qquad (5.17) \qquad\qquad \boldsymbol{\eta}_b = \begin{bmatrix} {}^b\boldsymbol{V}_\infty \\ {}^b\boldsymbol{\omega}_\infty \end{bmatrix} \qquad (5.18)$$

The structure of Equation 5.14 is very similar to that of Equation 4.9 and Equation 4.10. Indeed, the only difference lies in the parameters which must be identified. There are a total of 37 parameters which can be identified or calculated based on other theories. 36 of these parameters reside in the Φ matrix given by Equation 5.19. Each of the elements inside the Φ matrix given in Equation 5.19 is a three by three sub matrix, which must be positive definite. The superscripts denote how the velocities are linked to the wrench. For example, $\Phi^{(fv)}$ links the linear velocities to the aerodynamic forces.

$$\Phi = \begin{bmatrix} \Phi^{(fv)} & \Phi^{(f\omega)} \\ \Phi^{(mv)} & \Phi^{(m\omega)} \end{bmatrix} \qquad (5.19)$$

The similarities between this model and the regular parameterization become even more apparent when expanding the $\Phi^{(m\omega)}$ matrix as shown in Equation 5.20. Here one can see that the commonly used stability derivatives are linked to $\Phi^{(m\omega)}$ by a factor of one half. The final parameter which can be tuned is ϕ in Equation 5.17.

$$\Phi^{(m\omega)} = \frac{1}{2} \begin{bmatrix} C_{l_p} & C_{l_q} & C_{l_r} \\ C_{m_p} & C_{m_q} & C_{m_r} \\ C_{n_p} & C_{n_q} & C_{n_r} \end{bmatrix} \qquad (5.20)$$

Besides solving the issue of having undefined parameters during certain flight phases, a velocity parameterization has numerous other, arguably more important, benefits. First, the model is natively compatible with propeller wake models, which will be discussed in Section 7.1. Propeller wake models usually return the state of the flow behind the propeller in terms of velocity components. Using the same formulation for determining aerodynamic forces and moments circumvents having to determine the induced angle of attack through trigonometric functions. This is a massive advantage in view of the model's applicability to optimization based control.

Lustosa et al. also conducted some wind tunnel experiments, where they identified trim points throughout the flight envelope. They then fit a Buckingham-π based model to the wind tunnel data, which used a (α, β, Re, M) parameterization. Finally, they compared the trim points obtained from the new velocity model to the Buckingham-π based model. Here they found that the new model was less accurate in predicting trim points. Although, it should be noted that the coefficients for the new model were obtained from thin airfoil theory, whereas coefficients for the other model were derived from wind tunnel experiments. Therefore, it is difficult to establish whether the difference in accuracy stems from the model or the method used to derive the coefficients.

5.3. Lifting Line Theory

The study of finite wing aerodynamics dates back to the early 20th century. One of the first practical theories to predict wing lift was developed by Prandtl during the first World War. The general idea is to place multiple horseshoe vortices along a single line, famously dubbed the lifting line, and to determine the vorticity distribution along the span. The vorticity distribution is then integrated over the entire span to come up with an estimate of the wing lift and induced drag.

Although simple, classical lifting-line theory suffers from a number of limitations. First, the relationship between the lift coefficient and effective angle of attack are assumed linear. This means that the lift can only be estimated accurately at low to moderate angle of attack [7]. To solve this limitation, a more general nonlinear LLT was developed. However, to obtain a solution to the nonlinear LLT, the local lift distribution

is updated iteratively. Iterative methods, although convenient, can often suffer from convergence issues. Nonlinear LLT methods are not exempt from convergence issues, as shown by Goates and Hunsaker [13]. Additionally, in his original work, Prandtl only considered a straight wing. This assumption was important in the derivation of the classical lifting line theory [14]. Consequently, some modifications to the classical theory need to be made if it were to be used for the platform which is considered in this research.

More recent efforts by Goates and Hunsaker extended LLT to also work with swept wings subjected to sideslip [13]. Additionally, their work focused on overcoming the singularities which are often present in the lifting-line downwash integrals. Shortly after, Reid and Hunsaker proved that this method provides second-order convergence when the control points are cosine clustered [14]. Additionally, the calculated lift distributions closely match those of higher order panel methods.

However, there are still downsides to using a LLT based method. Although the lift calculations are quite accurate, only the induced drag is estimated. Therefore, one still has to determine the parasitic or viscous drag using some other methods.

5.4. Vortex Lattice Methods

An extension to the lifting line theory are a group of methods known as Vortex Lattice Methods (VLM). In contrast to classical LLT, VLM methods arrange the horseshoe vortices along a 2D grid on the wing. This results in more accurate predictions of the lift and moments acting on the body. Typical applications of VLM methods are small angles of attack and sideslip, where the boundary layer is generally thin and attached [15]. However, this does not mean that VLM methods cannot be applied to arbitrary flight conditions.

Unfortunately, the additional fidelity provided by arranging the vortices in a lattice further adds to the computational time over LLT codes. This makes VLM a bad choice for real-time evaluation of the aerodynamic forces and moments, as the runtime is usually on the order of seconds to minutes. However, VLM still has its use cases. Many vortex lattice augmentations were developed to explain specific phenomena, making it a great tool for understanding some underlying aerodynamics.

5.5. Strip Theory

Strip theory is different from the previously mentioned methods in the sense that it cannot predict the aerodynamic forces and moments on its own. Strip theory is a framework which divides the vehicle into smaller segments. Aerodynamic forces and moments are then individually calculated for each segment based on some other theories mentioned in the previous sections. This allows modelling on a component basis, which results in a flexible model. Many implementations of strip theory can be found throughout the literature. For example, Selig used a nonlinear LLT code to generate look up tables for lift, drag, and moment coefficients, which are then used to calculate the aerodynamic wrench applied at each segment [16]. Another example is the work by May et al., where 2D airfoil aerodynamics was used in tandem with 3D corrections to resolve the aerodynamic forces at each section [17]. The benefit of employing a strip theory approach is that one can simply add or subtract components of what make up the total aerodynamics in a certain section.

5.6. Takeaways

The main difficulty in modelling the quad-plane's aerodynamics is the large sideslip angles which regularly occur during operation. All methods mentioned in the previous section are capable of doing so. However, they go about it in different ways. Small perturbation theory and Lustosa's model fit parameters based on experimental or theoretical data. On the other hand, LLT and VLM use the wing shape and flow properties to determine the forces acting on the vehicle. LLT is not guaranteed to run in real time, and VLM currently cannot run in real time. Realistically, this leaves only the former type of model as a viable option. In terms of solving the problems experienced in roll, there would be little gain in implementing Lustosa's model over the currently used small perturbation based model.

Table 5.1: Comparison of aerodynamic modelling methods described throughout Chapter 5.

Method	real-time	Iterative	Singularities	Nonlinearities
Small Perturbation	Yes	No	No	Yes
Velocity Parameterization	Yes	No	No	Yes
LLT	Potentially	Yes	No	Yes
VLM	No	Yes	No	Yes

6

Propulsive Modelling

The most common methods used to determine the propulsive forces and moments caused by propellers will be outlined in this chapter. As explained in Section 4.3.2, the current model is based on static bench measurements. Section 6.1 expands upon this methodology by including effects caused by incidence. Subsequently, Section 6.3 covers blade element momentum theory, which is possibly the most widely used method of predicting propeller forces at incidence. A short overview of VLM based methods will be given in Section 6.4. Lastly, Section 6.5 will give an overview of the applicability of each method.

6.1. Parameter Identification

If the facilities are available, conducting additional experiments to extend the current model is a valid option. Simmons et al. constructed a global propeller model through model identification [11]. To obtain the force and moment data, Simmons et al. subjected a propeller to static wind tunnel tests at a variety of RPM, wind tunnel velocities and incidence angles. The independent variables were varied in a one-factor-at-a-time experiment.

Simmons et al. used a polynomial model akin to the stability derivative models used for aerodynamic modelling. Since they did not know the model structure beforehand, they used MOF modelling as outlined in Section 5.1.1. To recapitulate, the basic idea behind this method is to orthogonalize a set of predetermined regressors, such that the regressors are uncorrelated. When regressors are uncorrelated, it is simple to determine which terms contribute significantly to the model. Regressors which contribute less than a specified cut-off value are then simply discarded. The set of explanatory variables which Simmons et al. used to formulate a model are the advance ratio J and the Reynolds number Re. Furthermore, they made a distinction between tangential and axial advance ratio, defined by Equation 6.2 and Equation 6.1, respectively. Since MOF modelling will take care of discarding any terms which do not contribute sufficiently, one can simply choose a maximum polynomial degree and test for all combinations of explanatory variables.

$$J_z = \frac{V_z}{nD} = J \cos\left(i_p\right) \tag{6.1}$$

$$J_x = \frac{V_x}{nD} = J \sin\left(i_p\right) \tag{6.2}$$

An example of a model which was determined using MOF modelling is given in Equation 6.3. This model contains up to third order terms.

$$C_{T_z} = C_{T_{z_0}} + C_{T_{z_{J_z^2}}} J_z^2 + C_{T_{x_{J_x^2}}} J_x^2 + C_{T_{x_{\hat{Re}^3}}} \hat{Re}^3 + C_{T_{z_{J_z^3}}} J_z^3 \tag{6.3}$$

To obtain the coefficients given in Equation 6.3, Simmons et al. chose to use a simple least squares algorithm.

Unfortunately, propeller force and moment coefficients as well as model structure can vary considerably across the range of incidence angles and advance ratios. A possible solution is to establish local models,

which was adapted by Simmons et al. However, it is still not obvious how many local models need to be established and what ranges these local models would have to cover. The partitioning of local models is beyond the scope of this literature review, however Weinstein et al. have previously applied an automated framework in the context of global aerodynamic modelling [18]. The partitioning which Simmons et al. used can be seen in the top of Figure 6.1. The local models were then blended to obtain a global model, which can be seen in Figure 6.2. Blending of the local models was done using smoothing functions.
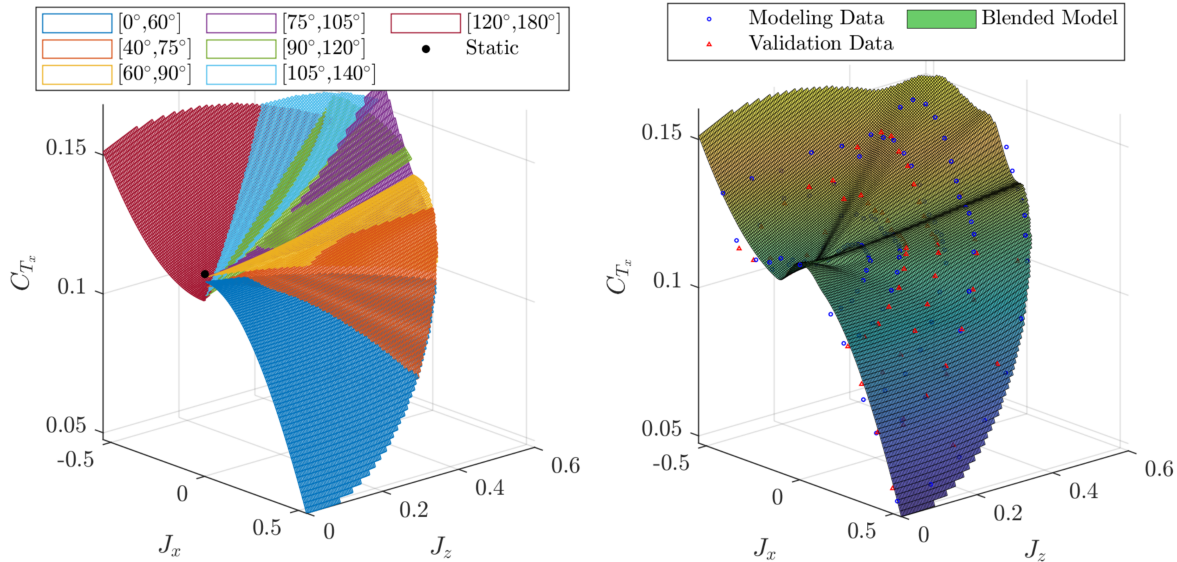
Figure 6.1: Partitioned thrust coefficient models over their region of validity (taken from [11]).

Figure 6.2: Global blended thrust coefficient model (taken from [11]).

6.2. Actuator Disk

The simplest analytical model to evaluate the thrust of a propeller is based on momentum theory. The model makes no assumptions on the propeller geometry, and assumes that the flow experiences a sudden jump of pressure when it crosses the propeller plane. This jump in pressure is what causes the flow to accelerate, which in turn creates thrust. Additionally, the model assumes that the inflow velocity is uniform, incompressible and inviscid. Since the geometry of the blades is not taken into account, classical momentum theory does not factor in the profile drag of the blades. This results in large discrepancies between theoretically and experimentally found power coefficients. However, the thrust coefficient overall agrees well with experiments. [19]

Rubin and Zhao derived an actuator disk model which predicts the thrust at incidence as a function of thrust at zero incidence [19]. They found that the thrust of a propeller can be attributed to two contributions. The first being the axial thrust due to the change in velocity of the flow at the propeller disk, denoted by T_{axial}. The second contribution is due to the lift generated by the propeller blades, denoted by T_{wing}. The total thrust is then a sum of both terms, as shown in Equation 6.4.

$$T = T_{axial} + T_{wing} \tag{6.4}$$

Which of the two terms is dominant is dependent on the angle of incidence at which the propeller is operating. Rubin and Zhao found that T_{axial} is dominant when the propeller operates at an incidence of 60 degrees or fewer. Naturally, this means that T_{wing} dominates when at large incidence angles. In this case, the propeller behaves like a rotating wing as the flow is aligned with the propeller disk. Equation 6.5 gives a simple analytical equation for determining the thrust at incidence.

$$\frac{T}{T_{i_p=0}} = 1 + \frac{\sin\left(i_p\right)^2}{\left(\cos\left(i_p\right) + \frac{w}{v}\right)\left(\sqrt{1 + 2\frac{w}{v}\cos\left(i_p\right) + \frac{w}{v}^2} + \cos\left(i_p\right) + \frac{w}{v}\right)} \tag{6.5}$$

Compared to higher fidelity theoretical models, actuator disk models lack in accuracy. However, they make up for it in computational time. Additionally, due to the assumption of uniform inflow, actuator disk models cannot compute off-axis forces. This means that overall, actuator disk models are only capable of (accurately) estimating one out of six wrench components.

6.3. Blade Element Momentum Theory

Blade element momentum theory is a combination of blade element theory and momentum theory with the purpose of predicting propeller performance. In blade element theory, the propeller blade is split into multiple elements, which are then analyzed independently. This requires knowledge about the local flow and airfoil geometry of the propeller. This knowledge is embedded into the method through momentum theory, which describes the flow of air passing through the propeller disk. The forces and moments induced by all elements are then summed up to find the total sum of forces and moments induced by the propeller.

BEMT is a widely used tool to predict the performance of propellers and wind turbines. However, the original theory was derived with axial flow in mind. To remedy this limitation, BEMT can be combined with a nonuniform inflow model, the like of which will be covered in Section 7.1. However, when Theys et al. performed a study on the accuracy of BEMT based models, they found that BEMT and VLM predicted correct trends in forces and moments but failed to accurately predict performance of propellers at large inclination [20]. The inflow model which Theys et al. used was a first order harmonic model given by Equation 6.6.

$$V_i\left(r, \Psi\right) = V_{i_{mean}}\left(1 + 2k_x r \cos\left(\Psi\right) + 2k_y r \sin\left(\Psi\right)\right) \tag{6.6}$$

Where k_x and k_y are coefficients which depend on azimuth angle Ψ, angular velocity of the propeller ω, freestream velocity V_∞ and propeller elevation angle. Leng et al. realized that rotational stall delay plays a large role in determining propeller performance at low advance ratios [8]. Therefore, they added a stall delay model to BEMT using the same first order inflow model as Theys et al. Contrary to Theys, Leng et al. found good agreement between their BEMT model and CFD analysis. Recently, Konuk et al. applied Leng's BEMT model to the case of a tilt-wing e-VTOL vehicle [21]. They found that the maximum thrust force coefficient error was approximately 8% at high speed, low incidence. Additionally, normal force maximum error was approximately 30% at high speed, moderate incidence.

The ultimate goal of the propulsive model is to be able to provide a 6-DOF wrench for each of the four propellers, as well as the induced velocity downstream of the two propellers in front of the wing. Additionally, all of this needs to happen in real time. Konuk et al. reported that their implementation of the model made by Leng et al. did not achieve real-time runtime. Nonetheless, they still used Leng's model and instead opted to construct a surrogate model based on Gaussian processes. The addition of the surrogate model surely contributed to the error seen in the comparison to experimental data. If a simple framework such as BEMT cannot run in real time and must be approximated by a surrogate model, then why not use a more accurate model in the first place? After all, Theys et al. showed that VLM performed slightly better than BEMT in predicting the forces and moments generated by small scale propellers under incidence [20].

Alternatively, one may apply simplifications to the classical BEMT theory to obtain an analytical model. For example, Gill et al. applied the simplification of a linear lift slope, quadratic drag polar, and specific chord distribution [3]. In contrast, Leng et al. linearized the thrust and power coefficients with respect to the tip speed ratio ($\lambda = \frac{V_\infty}{\Omega R}$), and the inflow model is approximated by a 2-harmonic cosine wave. The simplifications may vary between models, but the overarching goal is to keep the benefits of BEMT, namely being capable of determining the 6-DOF propulsive wrench, while reducing the computational cost. There will always be a trade-off between accuracy and computational time, so deriving a custom analytical BEMT model using assumptions specific to the quad-plane might be one of the best choices discussed so far for propulsive modelling.

6.4. Vortex Lattice Methods

There are two types of VLM implementations commonly used for propeller modelling. The difference lies in the description of the wake, namely one can prescribe a certain geometry to the wake of the propeller or the propeller wake can develop freely based on a given wake model. These methods are called prescribed

wake and free wake modelling, respectively. Prescribed wake models are generally more simple, less accurate and require less computation time.

Recently, Fei et al. developed an unsteady VLM code to model propellers at incidence [22]. This particular VLM implementation uses a simple free wake model. Additionally, the model neglects viscous contributions. Even with these simplifications, the model managed to predict very similar forces and moments compared to CFD analysis. Additionally, having a model of the wake embedded in the thrust calculations could simplify the process of modelling the propeller-wing interactions. Figure 6.3 shows the wake as predicted by the VLM code from Fei et al. under different incidence angles. Unfortunately, the model still ran nowhere near real-time. In fact, the author reported that it took between 20 seconds and 170 minutes to solve for a single case using two 24 core Intel Xeon Platinum 8160 CPUs, while parallelizing the Bio-Savart computations on four NVIDIA Tesla P4 GPUs. While this is still magnitudes faster than CFD, it is far too slow to be used for real-time propulsive modelling, let alone on a lightweight drone. This renders VLM infeasible unless a surrogate model is used.
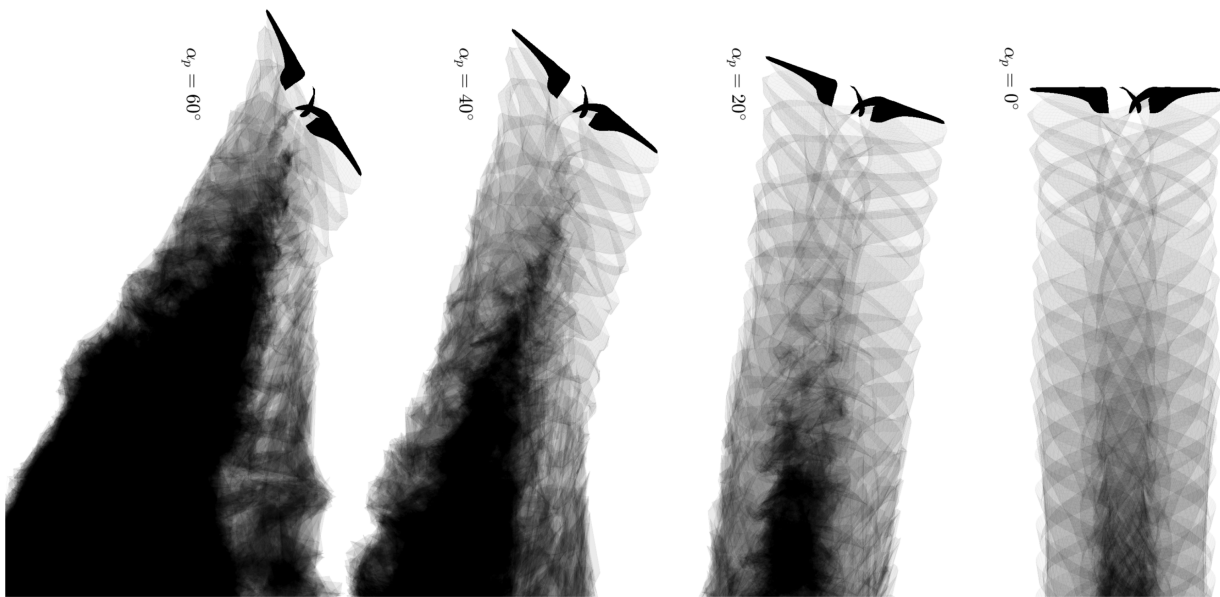
Figure 6.3: VLM capabilities of modelling wake behind propellers at incidence (taken from [22]).

6.5. Takeaways

Recently, Fernandez et al. compared analytical propeller models to experimental data under different incidence angles [4]. The models which they tested included the ones by Gill et al. [3], Leng et al. [23], and Rubin et al. [19].

Figure 6.4 shows one of many test cases used to compare the accuracy of the models. Visually, the trends remain largely the same between test cases. First, all models discussed provide reasonable approximating power for the thrust coefficient at no incidence. The first model to show a large deviation is the one by Rubin et al., which can likely be attributed to not factoring in the blade geometry. This deviation occurs already at low incidence, where the thrust prediction is already outside the confidence bounds at an incidence of twenty degrees. The analytical model derived by Leng et al. provides reasonable prediction of the thrust coefficient for incidence angles up to 55 degrees, however it quickly deviates after. Interestingly, this is exactly at the point in which Rubin et al. predicted that the lift produced by the propeller blades becomes the driving factor in producing thrust [19]. Lastly, the model proposed by Gill et al., provides a much more accurate prediction across the entire range of incidence angles. This is the case even when the parameters inside the model are identified using first principle aerodynamics, denoted by Gill A in Figure 6.4. Computing the power coefficient is a different story entirely. The only model which came reasonably close to predicting the power coefficient, was the model by Gill et al. where parameters were obtained through experiments, denoted by Gill E.
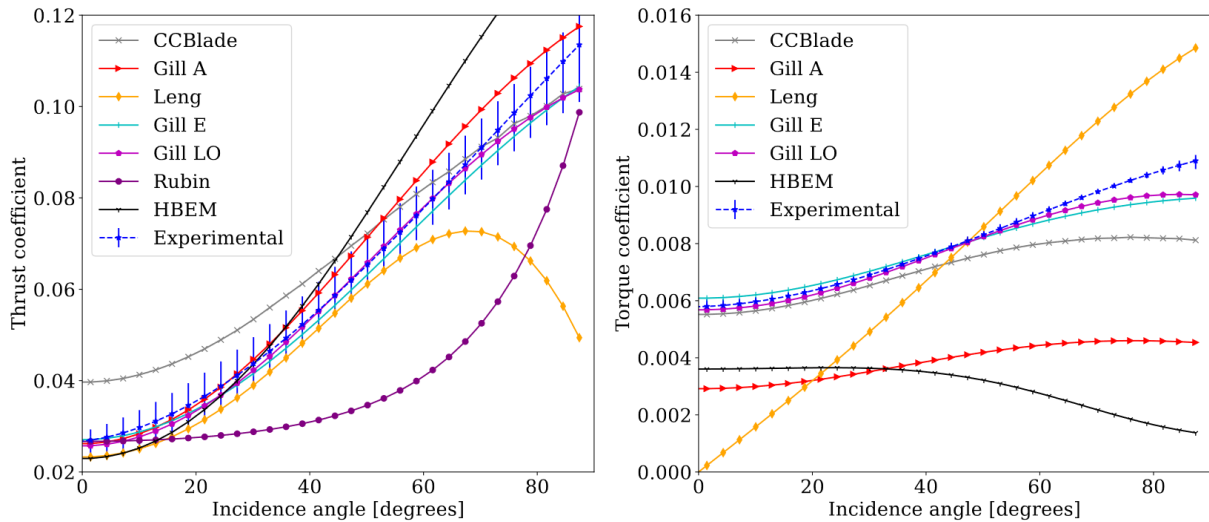
Figure 6.4: Comparison of thrust and power coefficients of different propeller models and experimental data, $V_\infty = 9\frac{m}{s}$ and $\Omega = 700\frac{rad}{s}$ (taken from [4]).

Theys et al. also compared different models to experimental data [20]. Their study was focused on BEMT and VLM methods. It is difficult to directly compare the results from Fernandez to the results of Theys. Theys found that both BEMT and VLM predicted thrust well, however the inaccuracy grows with incidence angle. This trend carried over to moment and off-axis force estimation, where the error grew with incidence angle. The difference in estimation was large enough that Theys concluded that neither BEMT nor VLM could accurately predict these forces. However, even at large incidence the magnitude of these forces was small, indicating that they will have negligible effect on the dynamics of the vehicle.

Table 6.1 makes a comparison between models in terms of computational time and output variables. One of the criteria for the propulsive model was that it returned all six components of the propulsive wrench. All models besides the actuator disk model fulfill this criterion. Additionally, it is clear that only analytical models and system identification models can run in real time. Both the analytical model provided by Gill et al. and the system identification based model by Simmons et al. show good agreement with experimental data, making both methods viable.

Table 6.1: Comparison between propeller models, CPU time adapted from [23].

Class	Method	Level of Resolution	CPU time [s]	Outputs
Analytical	Actuator Disk [19]	Low		C_T
	Analytical BEMT-based [23]	Low	10^{-3}	6-DOF coefficients
	Analytical BEMT-based [3]	Medium		6-DOF coefficients
Sys ID	Simmons et al. [11]	Medium	$<10^{-3}$	6-DOF coefficients
BEMT	Leng et al. [24]	Medium	10^1	6-DOF coefficients
VLM	Fei et al. [22]	High	10^4-10^6	6-DOF coefficients

A comparison between the models based on the general criteria can be found in Table 6.2.

Table 6.2: Comparison of propeller modelling methods described throughout Chapter 6.

Class	real-time	Iterative	Singularities	Nonlinearities
Analytical	Yes	No	No	Yes
System ID	Yes	No	No	Yes
BEMT	Potentially	Yes	No	Yes
VLM	No	Yes	Yes	Yes

<div align="right">

7

</div>

Propeller-wing Interactions

This chapter covers the theory and methods commonly used to model propeller-wing interactions. First is the characterization of the propeller wake, which applies mainly to the front two propellers, covered in Section 7.1. This section will cover three methods, namely jet theory which is built on momentum theory, vortex theory, and a dynamic inflow based approach. Additionally, the effects of wing obstruction will be investigated in Section 7.2. Finally, the main takeaways of the propeller-wing interactions will be summarized in Section 7.4.

7.1. Propeller Wake

Understanding the interactions between the propellers and the wing might be the key to identifying why the quad-plane does not roll when the propellers are tilted. However, the interactions between the propellers and the wing are extremely complex. The most simple case occurs when the propellers are aligned with the wing. In this case, actuator disc and momentum based models are often used due to their simplicity. These methods model the propeller wake induced velocity as a tube of constant axial velocity, where the magnitude of the induced velocity is determined through momentum theory. However, the assumption that the induced velocity behind the propeller is constant is not consistent with reality. Instead, the velocity in the wake of the propeller will include radial terms due to the rotation of the propeller, which are dependent on the azimuth angle. This leads to an increased angle of attack on the side where the propeller blades are travelling upwards and a decreased angle of attack on the side where the blades are travelling downward. Figure 7.1 shows how this affects the lift coefficient distribution over a finite wing.
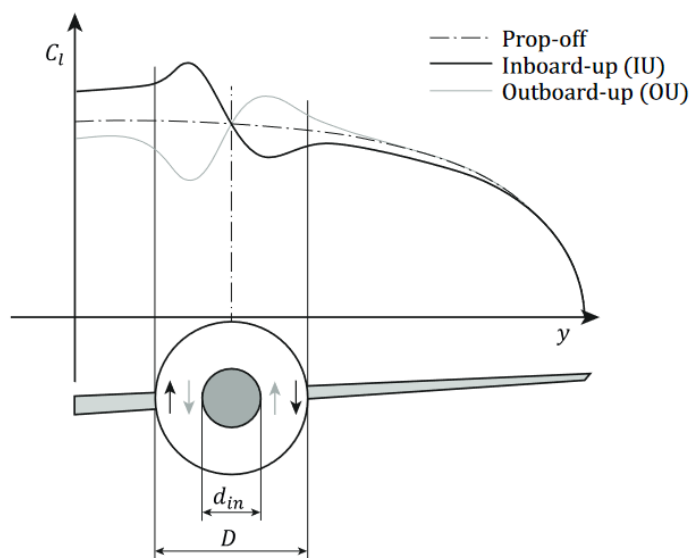
Figure 7.1: Effect of propeller slipstream on wing lift distribution (taken from [25]).

The dual-axis tilting rotors add additional complexity to determining the wing interactions. First, the wake will have a certain curvature when the propellers are tilted. This effect is the result of the interactions between the freestream flow and the propeller wake. Figure 7.2 shows wake measurements conducted by Yang et al. [26]. The figure clearly shows that the wake is no longer a cylindrical tube when the incidence angle increases. Additionally, The streamlines show that the resultant wake has a downwards velocity. This downwards velocity likely causes a reduction in wing lift in areas affected by the wake, which is the main reason believed to cause the rolling problem in fast, forward flight. Therefore, it is important that the model will be capable of predicting either the angle or vertical velocity component of the wake flow under incidence. The case gets even more complex when the angle of incidence is a combination of elevation and azimuth deflection. In this case, the areas of the wing affected are not directly behind the propeller, and the propeller likely induce both downwash and sideslip at some yet unknown location.
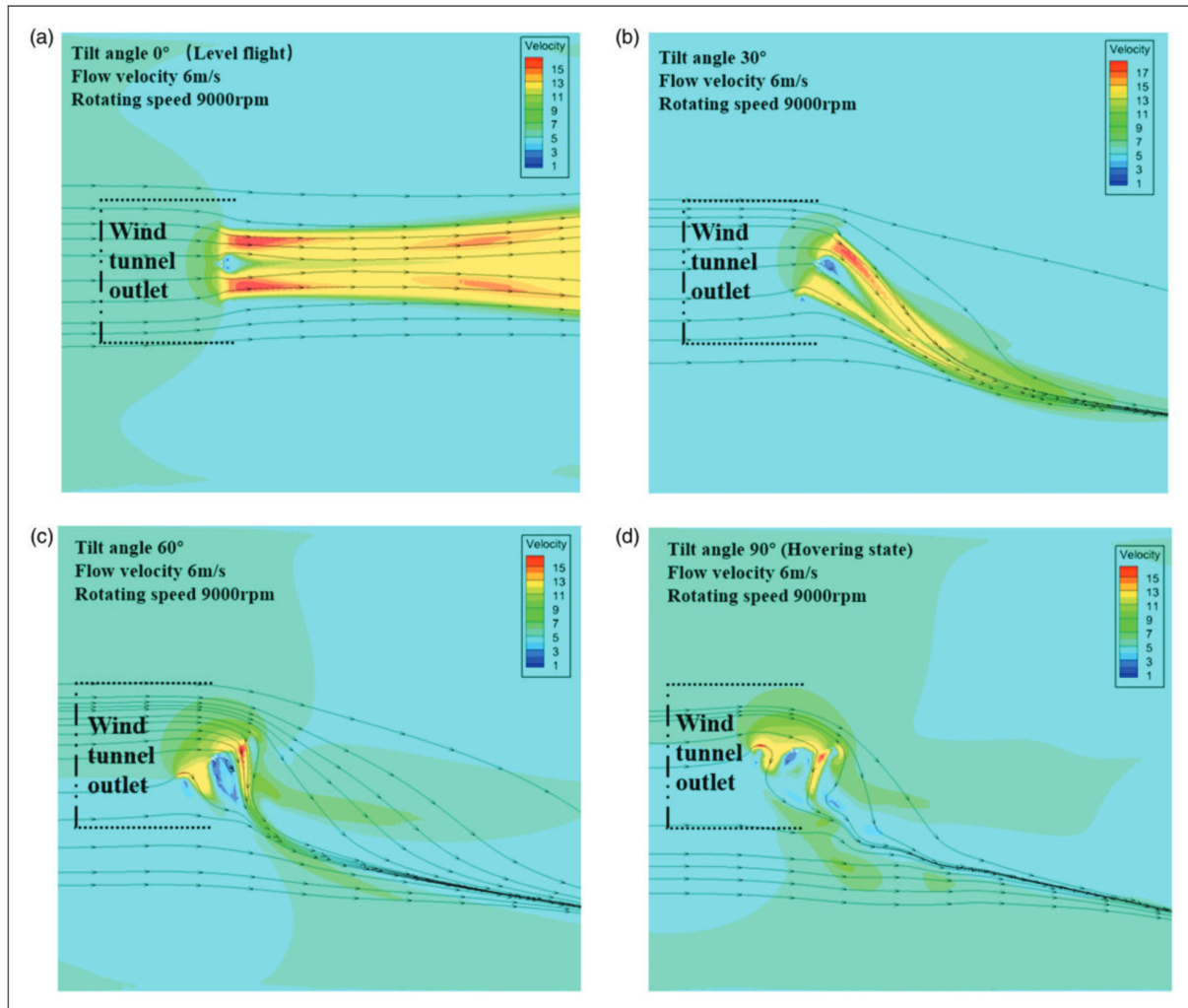
Figure 7.2: Slipstream flow field of tilt-rotors shown at different angles of incidence (taken from [26]).

Before diving into the different theories and methods of modelling the propeller wakes, it is important to first quantify the necessary output variables needed to incorporate the effects into the aerodynamic model.

The models covered in Chapter 5 model the forces based on one of two methods. Either they consider the angle of the flow with respect to the wing, or they use the flow velocity directly. Therefore, the most convenient output from the wake model would be an induced flow field, which can be added to the freestream velocity. The forces can then be calculated using the velocities directly, or they can first be converted into the appropriate angles.

The scale of the propellers is rather small compared to the size of the vehicle, which means that only part

of the wing will be affected by the propeller wake. Therefore, the area affected by the propeller wake needs to be known as well. It should be possible to determine the area affected by the wing directly from the flow field obtained from the wake model. However, as shown in Figure 7.1, the wake is not uniform throughout the wake. The most convenient method to model this non-uniformity is to apply a strip theory based method. This way the wing can be discretized, and the aerodynamic properties can be calculated locally based on the propeller induced flow field.

7.1.1. Jet Theory

One of the most simple methods of predicting slipstream effects on the wing is by considering the wake of the propeller to be a tube with an increased velocity due to the propeller. Selig argues that the wake of a propeller in hover behaves similarly to a free jet [27]. However, during cruise flight, the slipstream of the propeller contracts. Typically, the induced velocity downstream becomes twice the induced velocity at the propeller disc within a few propeller diameters [27].

The basic wake model is then given by simple addition of the propeller induced velocity and the freestream velocity, as described by Equation 7.1 and Equation 7.2.

$$V_{DS} = V_{local} + w_{DS} \qquad (7.1) \qquad\qquad w_{DS} = k_w w \qquad (7.2)$$

Where the jet flow parameter k_w is defined by Equation 7.3,

$$k_w = \begin{cases} k_s, m < m_s \\ k_s + \frac{(m-m_s)(k_f-k_s)}{m_f-m_s}, m_f > m > m_s \\ k_f \end{cases} \qquad (7.3)$$

and m is defined by Equation 7.4. The subscripts f and s can be regarded as a measure of propeller loading, where f denotes high and s denotes low propeller loading. k_s and k_f are predetermined coefficients which are roughly equal to 0.8 and 1.8 respectively.

$$m = \frac{V_{\infty,n}}{V_{disc,n}} \qquad (7.4)$$

The induced velocity is finally calculated using Equation 7.5.

$$w = \frac{1}{2}\left(-V_\infty + \sqrt{V_\infty^2 + \frac{2T}{\rho A}}\right) \qquad (7.5)$$

This results in a very simple slipstream model, which only gives a uniform axial component within the propeller slipstream. Selig additionally supplements this model with angle corrections to account for curved flow during maneuvers and first order time delays to account for unsteady effects. Although simple, there is not much accuracy to be gained over using a simple momentum theory based model. Additionally, the model can only provide a constant axially induced velocity, which is not in line with the concept shown in Figure 7.1.

7.1.2. Analytical Solution using Vortex Theory

This section will closely follow the work done by May et al. [17], in which they did aerodynamic modelling for a tilt-wing VTOL vehicle. The wake modelling technique which they applied is based on vortex theory. In contrast to momentum and jet theory, vortex theory is able to provide an axially varying induced velocity distribution. A prerequisite of this method is that the load distribution along the propeller blades must be known. This load distribution f_x is commonly approximated by Goldstein's optimal distribution given in Equation 7.6, where $\hat{r}$ is the nondimensional position given by Equation 7.7, and a, m, and n are coefficients to adapt the shape of the distribution to the propeller configuration.

$$f_x = \tilde{F}\hat{r}^m \left(\frac{a - \hat{r}^n}{a}\right) \qquad (7.6)$$

$$\hat{r} = \frac{r - r_{in}}{R - r_{in}} \tag{7.7}$$

Where r is the radial position with respect to the propeller axis, r_{in} the radius of the propeller hub, and R the complete radius of the propeller. The induced velocity at the propeller disc is given by Equation 7.8, which turns out to be identical to Equation 7.5.

$$V_x(r, x = 0) = \sqrt{\frac{V_{\infty,x}^2}{4} + \frac{f_x}{4\rho\pi r}} - \frac{V_{\infty,x}}{2} \tag{7.8}$$

After being accelerated by the propeller disc, the propeller slipstream will have a lower pressure than the flow in the vicinity. This pressure differential will cause the slipstream to contract. An analytical model for the wake propagation is given by Conway, which is shown in Equation 7.10. This propagation model assumes that the load distribution along the blades is elliptical, leading to an induced velocity at the disc, which follows from Equation 7.9. This velocity differs from the Goldstein optimal model.

$$\hat{V}_x(r, 0) = \frac{V_{x,0}}{R}\sqrt{R^2 - r^2} \tag{7.9}$$

$$\hat{V}_x(r, x) = 2V_x(r, 0) + V_{x,0}\left(-\hat{a} + \frac{x}{R}\arcsin\left(\frac{2R}{\hat{b}}\right)\right) \tag{7.10}$$

Where $\hat{a}$ and $\hat{b}$ are given by Equation 7.11 and Equation 7.12, respectively.

$$\hat{a} = \sqrt{\frac{\sqrt{R^2 - r^2 - x^2 + 4R^2x^2} + R^2 - r^2 - x^2}{2R^2}} \tag{7.11}$$

$$\hat{b} = \sqrt{x^2 + (R + r)^2} + \sqrt{x^2 + (R - r)^2} \tag{7.12}$$

To obtain the actual axially induced velocity V_x, the propagation model is multiplied by the in-plane solution provided by Conway. The axial velocity distribution at an arbitrary point follows from Equation 7.13.

$$V_x(r, x) = \frac{V_x(r, 0)}{\hat{V}_x(r, 0)}\hat{V}_x(r, x) \tag{7.13}$$

The concept that the propeller slipstream will eventually accelerate to twice the induced velocity at the propeller is an idealized theory. In reality, momentum exchange will occur between the fast travelling propeller wake and the slow travelling outside flow. This means that the slipstream will after a certain point start to expand again. This point is called the efflux plane, denoted by x_0 and calculated by Equation 7.14. This effect is schematically shown in Figure 7.3. According to May et al. there is not yet an analytical solution for the far-field, therefore an empirical method was applied to model the far-field slipstream.

$$x_0 = \sqrt{R\frac{V_0 - V_{i,avg}}{V_0}} \tag{7.14}$$

Where $V_{i,avg}$, is given by Equation 7.15.

$$V_{i,avg}(x) = -\frac{V_x}{2} + \sqrt{\frac{V_x^2}{4} + \frac{T}{2\rho\pi R^2}} \tag{7.15}$$
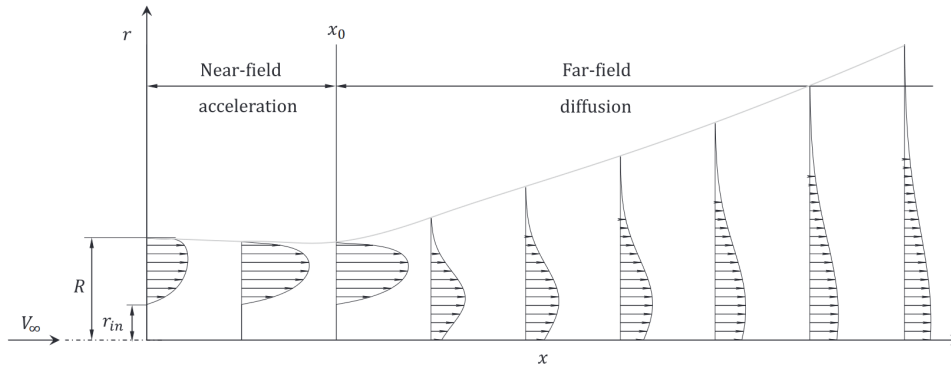
Figure 7.3: Axial slipstream development with regions of acceleration and diffusion, separated by Efflux plane at x_0 [17].

In addition to the axial velocity distribution, the radial and tangential velocities also contribute to the propeller wake. Besides the axial velocity, Conway also provides analytical solutions for both of the other velocities in terms of the same variables. The radial velocity is given by Equation 7.16.

$$V_r\left(r, x\right) = \frac{V_x\left|x\right|}{2r}\left(\frac{1}{\hat{a}} - \hat{a}\right) - \frac{V_x r}{2R}\arcsin\left(\frac{2R}{\hat{b}}\right) \tag{7.16}$$

Conversely, the tangential velocity is computed using Equation 7.17.

$$V_\theta\left(r, x\right) = -\operatorname{sgn}\left(\omega\right)\frac{f_\theta}{2\pi r\rho\left(V_x\left(r, x\right) + V_{i,x}\left(r, 0\right)\right)} \tag{7.17}$$

Where f_θ depends on the propeller geometry.

The wake model derived based on vortex theory looks like a promising model, as it contains not only axial flow. Additionally, the flow field can be computed with analytical equations, which realizes the criteria for real-time computation. The only downside is the lack of wake curvature.

7.1.3. Combined Dynamic Inflow and Wake Model
Another type of model, which is widely used in the helicopter flight simulation community, is the dynamic wake model first derived by Pitts and Peters. The Pitts and Peters model represents the inflow velocity at the rotor disk as a function of a uniform flow, side-to-side gradient and fore-to-aft gradient [28]. This velocity distribution is given by Equation 7.18.

$$v = V_0 + V_s r \sin\left(\Psi\right) + V_c r \cos\left(\Psi\right) \tag{7.18}$$

By defining the velocity as a function of three velocity distributions, it is then possible to establish a state-space system, given by Equation 7.19, which models the change over time of the inflow velocities.

$$[M]\begin{bmatrix} \dot{v}_0 \\ \dot{v}_s \\ \dot{v}_c \end{bmatrix} + V[L]^{-1}\begin{bmatrix} V_0 \\ V_s \\ V_c \end{bmatrix} = \begin{bmatrix} C_T \\ -C_L \\ -C_M \end{bmatrix} \tag{7.19}$$

Here M is the matrix of apparent mass terms, L is the inflow gains matrix and V, computed by Equation 7.20, is the weighted downstream velocity as a function of the advance ratio J, non-dimensional vertical velocity of the aircraft λ, and non-dimensional steady induced flow ν [29].

$$V = \frac{J^2 + \left(\lambda + \nu\right)\left(\lambda + 2\nu\right)}{\sqrt{J^2 + \left(\lambda + \nu\right)^2}} \tag{7.20}$$

Peters and Huang derived analytical values for each of these terms based on momentum theory. Additionally, C_T, C_L and C_M are the instantaneous rotor thrust, roll and pitching moment respectively. Note that dynamic inflow models do not predict the thrust of the propeller. This is done via different methods which were outlined in Chapter 6.

This inflow model was used by Leng et al. in their modelling of propellers at incidence [24]. The specific model which Leng et al. used was a first order Pitts & Peters model. The classical Pitts & Peters model can be extended by adding additional harmonic terms to the velocity distribution given in Equation 7.18. Deciding the number of harmonics of the inflow is a trade-off between accuracy and computational time.

Over the years, this model has been extended continuously to incorporate more effects. The three main additions were wake curvature, off-rotor flow field, and swirl velocity. Although, unlike with helicopters, the propeller system on the UAV makes up a proportionally smaller part of the vehicle dynamics. Therefore, higher order effects could be neglected to save on computation time. The last major advance in dynamic inflow models is the Huang-Peters model described in [5]. This model is capable of providing the complete 3-dimensional state of the flow at the rotor disk. Additionally, through the adjoint theorem proven by Fei, it is possible to determine the velocities in the wake as a function of adjoint states [30]. This is depicted in Figure 7.4, where the velocity of the wake at point a is a function of the co-states at points b, c and d.
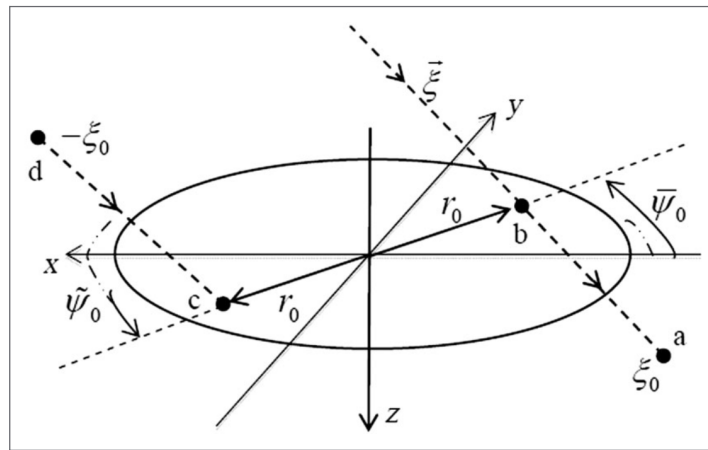
Figure 7.4: Three-dimensional perspective of adjoint co-states (taken from [30]).

Possibly the largest advantage of using this method is the possibility of having a combined inflow and wake model by using a single state space model. Additionally, the latest dynamic inflow models are not limited to a tube located behind the propeller disc, making it a perfect tool for modelling propeller-wing interactions when the propeller is not aligned with the wing. However, as mentioned in Section 6.3, Konuk et al. have tried implementing Leng's BEMT model which uses a first order Pitts & Peters model [21] and failed to realize real-time computation. Konuk et al. solved this problem by applying a surrogate model based on Gaussian processes. To make matters worse, this model does not yet consider the adjoint states necessary to calculate the velocity field behind the propeller. Lastly, there has been no mention of this method in the tilt-rotor UAV literature. While this does not diminish the potential of the method, it does make it difficult to choose over other proven methods. This also means that wind tunnel tests are a necessity to prove the validity of the model.

7.2. Wing Obstruction

All wake models described previously consider the wake to be free. This means that they ignore the potential obstruction effects caused by the wing, which is located downstream. Through experiments, Leng et al. have shown that the wake of a propeller does not necessarily take the form of a cylinder when obstructed by a wing. This is naturally the case, as the vortical flow behind the propeller cannot pass through the wing. The effect of wing obstruction is most pronounced at low advance ratio, as depicted in Figure 7.5, where the heatmap indicated the streamwise flow.
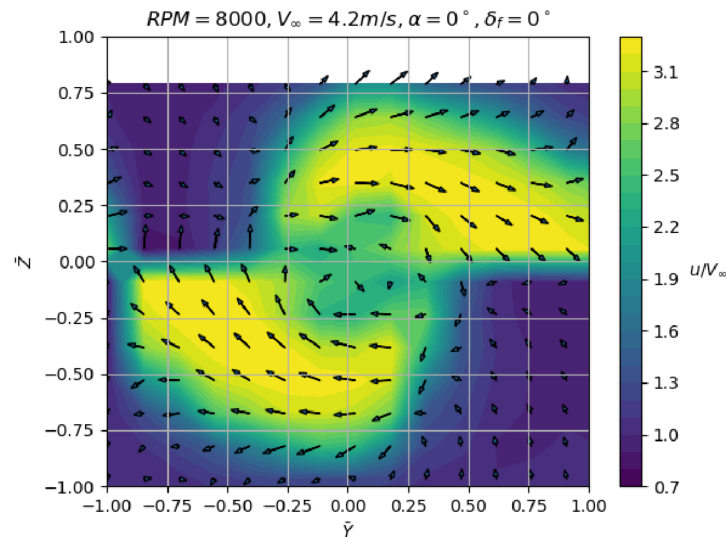
Figure 7.5: Velocity field in the propeller wake obstructed by a wing for $J = 0.25$ (taken from [31]).

To remedy this deficiency in current models, Leng et al. derived an analytical model by placing a lifting line of vortices which replace the wing [31]. However, there are some limitation with this model. First, the model requires knowledge of the propeller wake circulation Γ and wake helix angle ϕ. It was proposed that these quantities can be found through vortex theory. Second, the model assumes that the plane of interference is the center line. This assumption is appropriate for fixed propellers, but the propellers on the quad-plane can tilt in both elevation and azimuth. Although it is theoretically possible to extend this method to work with dual-axis tilting rotors, the question remains whether a general analytical solution exists.

7.3. Wing Downwash

Looking back at Figure 3.1, it is clear that the propellers located behind the wing will receive air which has travelled over the wing. This flow will certainly have different properties than the freestream airflow. In addition to the slipstream of the front propellers, the inflow of the rear propellers will experience downwash due to the wing-tip vortices.

One possible way to determine the downwash caused by the wing, is by simply using a LLT or VLM based method for determining the wing aerodynamics. These methods already calculate the spanwise downwash distribution during the process of determining the lift. However, the effect of wing downwash might be negligible in the grand scheme of things.

7.4. Takeaways

Correct modelling of propeller-wing interactions are likely the key to resolve the issues related to insufficient roll authority during fast, forward flight. Dynamic inflow provides many advantages over the other methods mentioned previously, as it can be extended to be a combined inflow and wake model. This makes the model attractive in the sense that it can be applied in two separate areas of the model. Additionally, dynamic inflow is capable of handling multiple rotor system [5, 6]. This is important, because the propellers in the back will experience inflow which lies in the wake of the propeller in the front and the wing. Dynamic inflow models are also extremely modular, and many of the publications state that they are meant to be real-time models. However, real time is subjective to a certain degree. A dynamic inflow code that might run in real time on a powerful flight simulation computer, may not run real time on the quad-plane.

However, validation of this approach was not found in the literature, making it difficult to fully commit to a dynamic inflow based approach. Inevitably, wind tunnel tests must be conducted to verify the accuracy of the model which is implemented. As a result, the viability of using system identification, similar to the propeller modelling technique applied by Simmons [11], should not be understated.

8
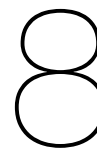
Onto a Global Aero-Propulsive Model

The previous chapters considered the modelling of different components individually. However, the goal was to construct a coherent global aero-propulsive model. Many of the methods described previously have been compared to experimental data or CFD analysis to show their accuracy. In isolation the methods perform well, however it is not clear how accurately they will model the global aerodynamics once strung together. Nevertheless, there is no general method capable of modelling all three components (aerodynamics, propulsion, propeller-wing interactions) while also running in real time. That being said, there is one exception: System identification. System identification is applicable to both aerodynamic modelling and propulsive modelling, and it indirectly takes the propeller-wing interactions into account through the coefficients. In fact, there are already examples of aero-propulsive models for UAV which were completely determined through system identification. One such example is the work by Simmons et al., where identification was used to obtain a global aero-propulsive model for a CZ-150 research aircraft [9]. Their model achieves a very close match with flight data.

However, there is one key drawback to using system identification to obtain the aero-propulsive model: The model will not give any physical insights into the propeller-wing interactions, which is hypothesized to be the driving factor behind the roll phenomenon. Additionally, the quad-plane is still in development, making it subject to potential changes. To avoid having to redo a potentially time-consuming system identification procedure, a modelling approach based on the following methods is suggested:

- Keep current stability derivative model.
- Implement Gill's propeller model.
- Wind tunnel test to identify the propeller-wing interactions.

The reasons behind these choices are the following:

Aerodynamic Model

The small perturbation model is very flexible, and replacing it with a more complex method will likely not lead to any benefits in solving the issues encountered with rolling in fast, forward flight.

Propulsive Model

The propeller model made by Gill et al. [3] provides the necessary balance between accuracy and adaptability. Unlike a system identification based approach, the model can also be used without conducting any wind tunnel testing. However, usage of wind tunnel data can help improve the accuracy if necessary.

Propeller-wing Interactions

The literature on propeller-wing interaction models applied to tilt-rotor vehicles is very limited, especially if computation time is taken into account. A combined dynamic inflow and wake model appears promising, but no experimental validation has been found for tilt-rotor vehicles. Therefore, a system identification approach will be used, where the data will be gathered from wind tunnel experiments.

9

Design of Experiments

This chapter will give an introduction on the topic of experiment design. Section 9.1 will give a brief introduction to classical design of experiments and explain why the current trend shifts away towards more modern design of experiment methods. Subsequently, Section 9.2 will explain the core principles behind modern design of experiments and give an overview of different design methods applicable to both static and dynamic testing.

9.1. Classical Design of Experiments

The most commonly used experiment designs in the last century were One-Factor-At-a-Time (OFAT) methods. As the name implies, experiments were carried out by varying only one independent variable at a time, while keeping all others constant. These designs were convenient, as they clearly expose the relationship between the system and a certain independent variable. However, this method is completely blind to the complex interactions which might be taking place inside the system when multiple independent variables are changed simultaneously.

Additionally, this method requires the system to be in "statistical control" to generate accurate and reliable data. This means that the mean value of the measurements must be constant over time. This requirement is quite stringent and difficult to maintain even in controlled environments such as a wind-tunnel [32].

9.2. Modern Design of Experiments

Modern Design of Experiments (MDOE) is a twist on conducting experiments with a different goal in mind than just collection all the necessary data. The goal of MDOE is to minimize the resources (time, runs, reconfigurations, etc.) which are necessary to gather sufficient data to model with a certain level of accuracy. This methodology was introduced by DeLoach at NASA Langley in the late 1990s to early 2000s [32].

Conventional experimental methods are usually concerned about gathering as many high quality data points in as short amount of time as possible. However, modern methods focus more on being able to predict response performance more accurately. As such, an experiment designed using the MDOE framework ends when sufficient data is captured to model a certain phenomenon with a specified accuracy, not when all test cases have been examined. This helps in reducing the time and resources spent conducting experiments. A testament to this is the wind tunnel campaign led by McDaniel used to characterize the aerodynamic model of the Shadow UAV [33]. McDaniel tested both the conventional OFAT and a face centered central composite MDOE design. The MDOE design required 70% less wind tunnel data to achieve the same level of accuracy. This also led to a 54% decrease in wind tunnel time necessary to gather all data.

Additionally, the goal of MDOE is to facilitate globally accurate response prediction. Due to the nature of MDOE designs, the prediction error of a specific response estimate is a function of the ensemble error estimate instead of solely the nearest test condition. This enables MDOE to provide more accurate models even if less accurate data sensors are used.

The MDOE framework consists of a total of five steps which need to be performed before experimentation begins [34]. The first step is stating the objective. In this case, the objective is to establish a full envelope

aero-propulsive model for a four dual axis tilt-rotor quad-plane. Specifically of interest are the propeller-wing interactions, which might be dampening the roll moment generation of the front propellers.

The second step is to set the design space. There is still doubt about which aerodynamic model will be used. The two options are the classical stability derivative model or the more recent velocity based parameterization mentioned in Section 5.2. Therefore, it is important for the experiment to cover both design spaces equally well.

Step three is to scale the experiment. The accuracy of the model is determined in this step. Once a desired accuracy and model structure is chosen, it is possible to find the required number of data points to achieve said accuracy.

In addition to the test conditions, it is also imperative to run some additional trials to gather confirmation points. This data will be used to test the identified model for accuracy and overfitting.

The final step is to select a desired design matrix. Yondo et al. give a recent review of the available experiment designs [35].

9.2.1. Factorial Designs

Factorial designs are a type of modern design of experiments. A geometrical representation of a 2-level 3-factor full factorial design can be seen in Figure 9.1. If the number of levels and factors is large, it is also possible to run a fractional-factorial experiment, which eliminates some design points. Factorial designs require the response of the system to be approximately linear over the design space.
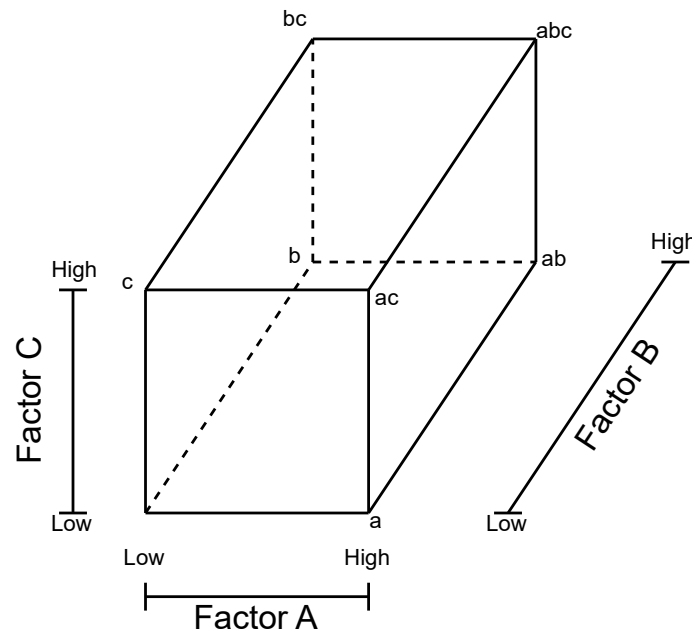
Figure 9.1: Geometrical view of a full 3-factor 2-level factorial design, adapted from Yondo et al. (taken from [35]).

Overall, it seems like factorial designs are not a good approach for the specific case of full envelope aero-propulsive modelling. Firstly, this is due to the strong nonlinearities observed in aerodynamics. Secondly, the number of independent factors which determine the aerodynamic wrench is quite large.

9.2.2. Central Composite Designs

In contrast to factorial designs, central composite designs (CCD) were developed to fit quadratic objective functions. CCDs are an extension to factorial designs, where the design is augmented with center and star points. Central composite designs are quite popular due to their adaptive nature. During the experiment, one can opt to add or remove star points.

As mentioned in Section 9.2, McDaniel used a face centered CCD for aerodynamic model identification of the Shadow UAV. The viability of this method depends on the model structure. If only up to second order terms are chosen in the model structure, then this experiment design is viable.

9.2.3. Orthogonal Arrays Designs
Orthogonal arrays, also often referred to as Taguchi methods, is a type of testing which consists of sets of fractional factorial designs. This type of testing is usually convenient for systems which have many test cases, as factors are tested in combinations. As with factorial designs, in orthogonal array designs each factor can have multiple levels.

This leads to a method which guarantees pairwise combinations of all factors, with a much lower experimental effort compared to factorial designs [35]. Additionally, it is possible to choose the distribution of pairwise combinations. This is useful in the sense that it is possible to generate one design, which includes all combinations, yet for example in the case of the quad-plane puts more emphasis on determining the propeller-wing interactions. Generation of orthogonal arrays is also relatively simple, which makes them a prime candidate for the wind tunnel experiments.

9.2.4. Latin Hypercube Designs
Latin hypercube designs are based on random sampling of the design space. The design space is divided into a certain number of equally probable intervals. In the case of two dimensions, latin hypercubes are equivalent to the latin square inspired by Euler [35]. Here, the two-dimensional square array is filled with design points such that there is only a single point in each column and row. Figure 9.2 shows a potential latin square design with four intervals on each axis. Latin hypercubes are then simply a higher dimensional generalization of this concept, with only one point on each axis.
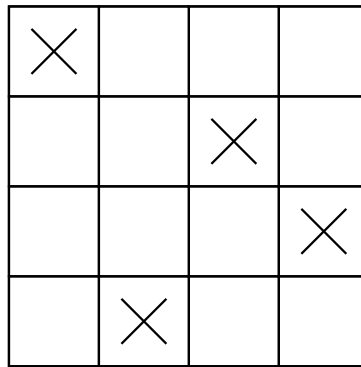
Figure 9.2: Example of a latin square design with four intervals in each dimension.

Latin hypercube designs are the most popular design strategy for computer simulations used in the field of aerodynamics [35]. This stems largely from their simplicity and flexibility. Furthermore, it was shown that latin hypercubes perform better than other same size random sampling methods [35]. However, latin hypercubes are not space-filling, meaning that there are potentially areas within the design space which will not receive sufficient points to generate an accurate response.

9.2.5. Euclidean Distance Designs
As the name implies, Euclidean distance designs are a group of designs which specify the design points through a Euclidean distance metric. One such design is miniMax design, with the goal of minimizing the maximum distance between design points in the design space. This optimization problem is defined by Equation 9.1 [36].

$$\underset{D_n \in \mathbb{D}_n}{\arg\min} \sup_{x \in \chi} \|\boldsymbol{x} - Q\left(\boldsymbol{x}, D_n\right)\| \tag{9.1}$$

Where $\mathbb{D}_n$ is the set of all unordered design points within the design space, and $Q\left(\boldsymbol{x}, D_n\right)$ returns the nearest design point, given by Equation 9.2 and Equation 9.3, respectively.

$$\mathbb{D}_n \equiv \{\{\boldsymbol{m}_i\}_{i=1}^n : \boldsymbol{m}_i \in \chi\} \tag{9.2}$$

$$Q\left(\boldsymbol{x}, D_n\right) \equiv \operatorname*{argmin}_{z \in D_n} \|\boldsymbol{x} - \boldsymbol{z}\| \tag{9.3}$$

Alternatively, there is the maxiMin design, which maximizes the minimum distance between design points. Both designs are loosely related to the sphere packing problem, which aims at maximizing the number of fixed size spheres which one can fit into a certain volume [37].

Space filling designs are generally best used in applications where the outcome of the experiment is deterministic, such as numerical simulations. As it is desirable to keep track between any model iterations or changes, a miniMax design can be used to establish a standardized set of test points. This would allow for good coverage of the design space without testing the entire flight envelope.

Although the idea behind distance based designs is simple, in practice there is still research being done on finding fast algorithms capable of covering arbitrary design spaces of high dimension. Mak et al. proposed an algorithm based on clustering and particle swarm optimization (mMc-PSO) capable of finding near globally optimal miniMax designs [36]. Although slower than principal points and Fast flexible space-filling (FFF) algorithms, mMc-PSO scales well to higher dimensions and consistently delivers designs with low miniMax criteria compared to the other methods mentioned.

9.2.6. Dynamic Testing

The previous sections concerned themselves with experiments which are carried out in static conditions, such as a static wind tunnel test bench. However, a considerable part of the aerodynamics is contained within the dynamics of the vehicle. There are multiple ways to get the necessary data to fit the model parameters related to the dynamic modes. The first and most controlled is using a dynamic test bed inside a wind tunnel, such as Szymanski et al. [38]. Alternatively, one may carry out flight tests and excite the dynamics of the vehicle with specific maneuvers and control surface inputs.

Traditionally, aircraft data was collected using multistep inputs or frequency sweeps. Flight test maneuvers were generally done in an OFAT fashion, where one actuator was given a sequence of inputs. Some examples of very popular inputs are the doublet or 3-2-1-1. A doublet refers to an alternate positive and negative deflection of a control surface, such as for example the elevator. The 3-2-1-1 maneuver is simply an extension to doublets with additional step inputs, where the number indicates the relative length of the input. Similarly, frequency sweeps target one input at a time. Here the pilot or control system gives a periodic input which varies in frequency over time. Frequency sweeps were commonly used to determine the frequency response of a vehicle.

Similar to static testing, the use of MDOE methods has recently experienced a surge in popularity in dynamic testing. However, due to constraints on the sensing equipment available on the drone and due to the large perturbations experienced, it is difficult to capture sufficiently accurate data from flight tests. Alternatively, one might conduct flight tests inside a wind tunnel, which provides an environment with minimal external disturbances. Naturally, flying inside a wind tunnel imposes certain limits on the maneuvers which a drone is allowed to undertake. The largest section wind tunnel available at TU Delft is the Open Jet Facility (OJF) with a cross-section of 2.85 by 2.85 meters. In comparison, the quad-plane already has a wingspan of 1.85 meters, leaving only fifty centimeters on either side for lateral maneuvers.

A potential solution to flight testing inside of wind tunnels are orthogonal, optimized multi-sine input designs. The general idea is to excite the drone with wideband frequency inputs containing the expected modal frequencies of the dynamic response [39]. The perturbations are applied to the system by summing the designed orthogonal multi sine signal with the feedback from the control system. The perturbations are designed to be orthogonal in both time and frequency domain and are only applied over a short period of time which minimizes the deviation from the nominal flight condition. Additionally, the signals are designed to feature a low Relative Peak Factor (RPF) between the different frequency components featured in the signal. The actuator inputs are given by a sum of orthogonal sine signals, as shown in Equation 9.4.

$$\boldsymbol{u}_j = \sum_{k \in 1,2,\ldots,M} A_k \sin\left(\frac{2\pi k \boldsymbol{t}}{T} + \phi_k\right) \tag{9.4}$$

Where the RPF is given by Equation 9.5.

$$RPF\left(\boldsymbol{u}_j\right) = \frac{\max\left(\boldsymbol{u}_j\right) - \min\left(\boldsymbol{u}_j\right)}{2\sqrt{2\frac{\boldsymbol{u}_j^T \boldsymbol{u}_j}{N}}} = \frac{\max\left(\boldsymbol{u}_j\right) - \min\left(\boldsymbol{u}_j\right)}{2\sqrt{2}\,\mathrm{rms}\left(\boldsymbol{u}_j\right)} \tag{9.5}$$

As is common for MDOE approaches, orthogonal multi sine designs excite multiple control surfaces at the same time to minimize the time required spent testing. This is particularly important for conditions which the drone cannot sustain for prolonged periods. Additionally, since the inputs to the control surfaces are orthogonal, the data which is collected is de-correlated in the inputs, leading to more accurate control effectiveness data.

Morelli has shown that using orthogonal multi sine inputs can be used to obtain estimates for aerodynamic parameters commonly found in the aerodynamic models mentioned in Section 5.1 [39, 10]. Due to the effectiveness of the multi sine inputs, Morelli et al. managed to get accurate measures for the aerodynamic coefficients even past stall. Additionally, they managed to conduct tests in unstable modes due to the time effectiveness of the designs generated by this method.

9.2.7. Generation of Orthogonal Multi Sine Signals

A key property of orthogonal multi sine signals is that they are orthogonal in both time and frequency domain. For each sinusoidal signal, there are two parameters which may be varied such that the final signal is indeed orthogonal. These two parameters are the frequency of the sine wave and the phase shift.

First, consider the frequencies of the sine waves. The set of frequencies which may be assigned to the sine wave depend on two factors. Namely, the frequency band which needs to be excited and excitation period T. In the frequency domain, sine waves are discrete peaks at their respective frequency. Therefore, they are by default orthogonal as long as two different inputs are not excited with the same frequency [40]. In short, multi sine signals are orthogonal in the time domain as long as the frequencies are chosen as the harmonic frequencies and the sine signals use the same base time period T. Additionally, the harmonic frequencies need to be unique for each signal. An example of an orthogonal multi sine signal experiment can be seen in Figure 9.3.
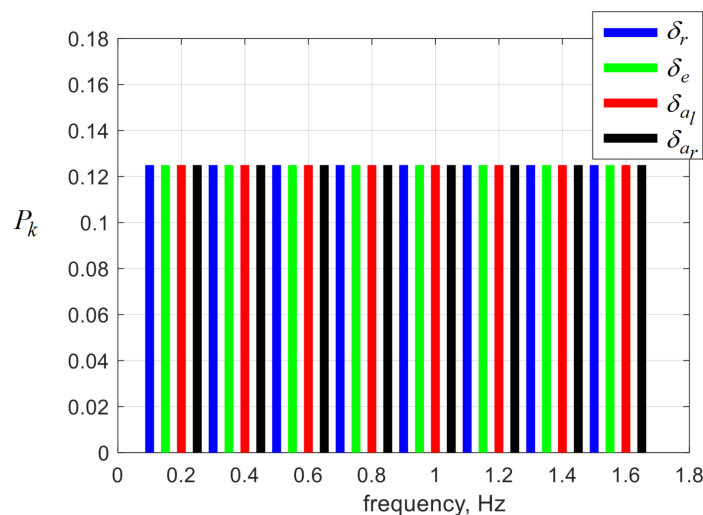
Figure 9.3: Example of an orthogonal optimized multi sine input spectra (taken from [40]).

10

Research Outline

The time frame over which this research will be carried out is approximately nine months. The first two months were spent finding relevant literature on the topic of aero-propulsive modelling, as well as deciding which parts of the modelling will be focused on. Figure 10.1 shows how the nine months of research will be split into six different phases. The first phase will end with the submission of the literature review.
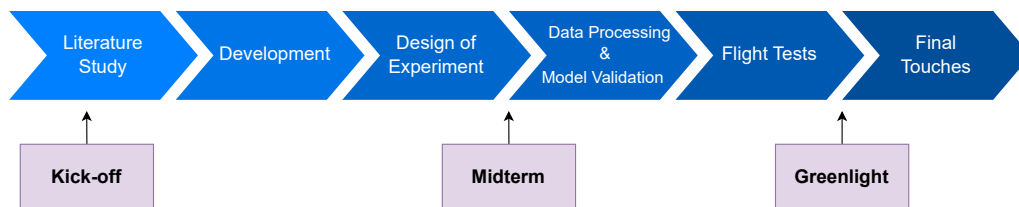

Figure 10.1: Research divided into phases.

Development

Chapter 8 discussed the choice of models. These models will be implemented and verified during the development phase. By the end of this phase, it will become clear what exactly needs to be tested during the wind tunnel experiments.

Design of Experiment

In this phase, the wind tunnel experiments will be prepared and executed. This includes manufacturing the fastening mechanism and acquiring any necessary test equipment. During the last week of this phase, the wind tunnel test will be carried out.

Data processing and model verification

Large amounts of data will be captured during the wind tunnel experiments. The data will be processed and used to refine the models which were developed during the development phase. Additionally, the models will be validated once the data has been used to estimate the parameters in the model.

Flight Tests

Flight tests will be conducted to validate the model changes and to ensure that the quad-plane can fly without aerodynamic surfaces.

Final touches

During the final phase, new insights from the flight tests will be incorporated into the model. Documentation will be generated continuously during the entirety of the research. However, it is likely that significant time will be spent here writing.

11

Conclusion

The overarching goal of this research is to create a more accurate aero-propulsive model, covering the full flight envelope of the quad-plane designed by Mancinelli et al. To fulfill this goal, a literature review was conducted to learn about the state-of-the-art in aero-propulsive modelling. The three most important components of the aerodynamic model were identified to be the aerodynamics of the wing, propeller performance and propeller-wing interactions.

The goal of the literature review was to answer the following four research questions:

> **Research Question 1**
>
> What methods are best suited for full-envelope aerodynamic modelling?

Although the model provided by Lustosa et al. comes with some clear benefits over the standard stability derivative based model, such as the non-singular inputs, it was decided to keep the current aerodynamic model. The reason being twofold: first, the current model is flexible and it can be expanded if necessary, second replacing the current model with a velocity parameterization will likely lead to a negligible improvement in roll moment prediction.

> **Research Question 2**
>
> What methods are best suited for propulsive modelling of propellers?

There were two types of model which met the criteria. The first type consists of analytical models based on blade element momentum theory. The second type are models based on parameter identification. Analytical models are more flexible, as wind tunnel data is not strictly necessary. Therefore, the model of Gill et al. will be implemented as it takes into account inflow effects, can be evaluated in real time, and the accuracy can be supplemented with wind tunnel data if necessary.

> **Research Question 3**
>
> What methods are best suited for modelling propeller-wing interactions?

Understanding the propeller-wing interactions was deemed the key to understanding the observed difficulty in rolling during fast, forward flight. While a combined inflow and wake model were briefly considered, there are too many uncertainties to confidently implement this method. There is no method which clearly satisfies all the requirements of the controller, while also having been validated for tilt-rotor quad-planes. Therefore, a system identification approach akin to what Simmons used to model propellers in oblique flow would be the simplest approach. However, this approach does require dedicated wind tunnel testing.

Research Question 4

> How can the aerodynamic and propulsive model be combined into a global aero-propulsive model?

To solve the issues regarding roll control, it would be most important to accurately model the propellers at incidence and characterize the propeller-wing interactions. It is unnecessary and even inconvenient to make a holistic model for the quad-plane, as it is still in development and subject to change. A much better approach would be to use independent components which can easily be modified if the need arises. A simple yet powerful change can already be made in the propeller model by including a dependence on the inflow angle. Taken this into account, the model which is most flexible would be the model made by Gill et al. Unfortunately, the literature on propeller-wing interaction models applicable to tilt-rotor vehicles is limited, forcing a solution based on wind tunnel testing, which might not be easily adaptable. Nevertheless, the aerodynamic model allows for easy additions of terms, which includes a model derived from wind tunnel tests.

References

[1] Alessandro Mancinelli et al. "Dual-axis tilting rotor quad-plane design, simulation, flight and performance comparison with a conventional quad-plane design". In: *2022 International Conference on Unmanned Aircraft Systems, ICUAS 2022*. United States: Institute of Electrical and Electronics Engineers (IEEE), 2022, pp. 197–206. DOI: `10.1109/ICUAS54217.2022.9836063`.

[2] Leandro R. Lustosa et al. "Global Singularity-Free Aerodynamic Model for Algorithmic Flight Control of Tail Sitters". In: *Journal of Guidance, Control, and Dynamics* 42.2 (2019), pp. 303–316. DOI: `10.2514/1.G003374`.

[3] Rajan Gill et al. "Computationally Efficient Force and Moment Models for Propellers in UAV Forward Flight Applications". In: *Drones* 3.4 (2019). DOI: `10.3390/drones3040077`.

[4] Luiz F. Fernandez et al. "Assessment of Methods for Propeller Performance Calculation at High Incidence Angles". In: *AIAA SCITECH 2023 Forum*. DOI: `10.2514/6.2023-2283`.

[5] Jianzhe Huang et al. "Real-time solution of nonlinear potential flow equations for lifting rotors". In: *Chinese Journal of Aeronautics* 30.3 (2017), pp. 871–880. DOI: `https://doi.org/10.1016/j.cja.2017.02.007`.

[6] Jianzhe Huang et al. "Validation of Blended Potential Flow Model for Lifting Rotors with Wake Contraction". In: *Journal of Applied Nonlinear Dynamics* 5 (Sept. 2016), pp. 349–371. DOI: `10.5890/JAND.2016.09.007`.

[7] John D. Anderson. *Fundamentals of Aerodynamics*. fifth. New York, NY: McGraw-Hill, 2011.

[8] Yuchen Leng et al. "Experimental Analysis of Propeller Forces and Moments at High Angle of Incidence". In: *AIAA Scitech 2019 Forum*. DOI: `10.2514/6.2019-1331`.

[9] Benjamin M. Simmons et al. "Aero-Propulsive Modeling for Propeller Aircraft Using Flight Data". In: *Journal of Aircraft* 0.0 (2022), pp. 1–16. DOI: `10.2514/1.C036773`.

[10] Eugene Morelli. "Efficient Global Aerodynamic Modeling from Flight Data". In: *50th AIAA Aerospace Sciences Meeting including the New Horizons Forum and Aerospace Exposition*. DOI: `10.2514/6.2012-1050`.

[11] Benjamin M. Simmons. "System Identification for Propellers at High Incidence Angles". In: *Journal of Aircraft* 58.6 (2021), pp. 1336–1350. DOI: `10.2514/1.C036329`.

[12] Marc S. May et al. "Dynamic Modeling and Analysis of Tilt-Wing Electric Vertical Take-Off and Landing Vehicles". In: *AIAA SCITECH 2022 Forum*. DOI: `10.2514/6.2022-0263`.

[13] Cory D. Goates et al. "Practical Implementation of a General Numerical Lifting-Line Method". In: *AIAA Scitech 2021 Forum*. DOI: `10.2514/6.2021-0118`.

[14] Jackson T. Reid et al. "General Approach to Lifting-Line Theory, Applied to Wings with Sweep". In: *Journal of Aircraft* 58.2 (2021), pp. 334–346. DOI: `10.2514/1.C035994`.

[15] Ethan Loewenthal et al. "Low-Order Modeling of Wingtip Vortices in a Vortex Lattice Method". In: *AIAA Journal* 60.3 (2022), pp. 1708–1720. DOI: `10.2514/1.J060654`.

[16] Michael Selig. "Modeling Full-Envelope Aerodynamics of Small UAVs in Realtime". In: *AIAA Atmospheric Flight Mechanics Conference*. DOI: `10.2514/6.2010-7635`.

[17] Marc S. May et al. "Semi-Empirical Aerodynamic Modeling Approach for Tandem Tilt-Wing eVTOL Control Design Applications". In: *AIAA SCITECH 2023 Forum*. DOI: `10.2514/6.2023-1529`.

[18] Rose Weinstein et al. "Global Aerodynamic Modeling Using Automated Local Model Networks in Real Time". In: *AIAA Scitech 2020 Forum*. DOI: `10.2514/6.2020-762`.

[19] Rafael L. Rubin et al. "New Development of Classical Actuator Disk Model for Propellers at Incidence". In: *AIAA Journal* 59.3 (2021), pp. 1040–1054. DOI: 10.2514/1.J059734.

[20] B. Theys et al. "Experimental and Numerical Study of Micro-Aerial-Vehicle Propeller Performance in Oblique Flow". In: *Journal of Aircraft* 54.3 (2017), pp. 1076–1084. DOI: 10.2514/1.C033618.

[21] Ege Konuk et al. "Computer Based Modeling for Tilt-Wing e-VTOL Propeller Performance". In: *AIAA SCITECH 2023 Forum*. DOI: 10.2514/6.2023-0339.

[22] Xiaofan Fei et al. "Development of an Unsteady Vortex Lattice Method to Model Propellers at Incidence". In: *AIAA Journal* 60.1 (2022), pp. 176–188. DOI: 10.2514/1.J060133.

[23] Yuchen Leng et al. "Analytic Model of Proprotor Forces and Moments at High Incidence". In: *Journal of the American Helicopter Society* 66.4 (Oct. 2021), pp. 1–15. DOI: 10.4050/JAHS.66.042002.

[24] Yuchen Leng et al. "Aerodynamic Modeling of Propeller Forces and Moments at High Angle of Incidence". In: *AIAA Scitech 2019 Forum*. DOI: 10.2514/6.2019-1332.

[25] L.L.M. Veldhuis. "Propeller Wing Aerodynamic Interference". PhD thesis. Delft, the Netherlands: Delft University of Technology, June 2005.

[26] Haitao Yang et al. "Aerodynamic performance of a small-scale tilt rotor: Numerical simulation and experiment in steady state". In: *Proceedings of the Institution of Mechanical Engineers, Part C: Journal of Mechanical Engineering Science* (2020). DOI: 10.1177/0954406220950352.

[27] Michael Selig. "Modeling Propeller Aerodynamics and Slipstream Effects on Small UAVs in Realtime". In: *AIAA Atmospheric Flight Mechanics Conference*. DOI: 10.2514/6.2010-7938.

[28] David A. Peters et al. "Dynamic Inflow for Practical Applications". In: *Journal of the American Helicopter Society* 33.4 (1988), pp. 64–68. DOI: 10.4050/JAHS.33.64.

[29] Thomas J. Ellenrieder. "Investigation of the Dynamic Wake of a Model Rotor". PhD thesis. Bristol, United Kingdom: University of Bristol, Oct. 1995.

[30] Zhongyang Fei. "A Rigorous Solution for Finite-State Inflow throughout the Flowfield". PhD thesis. Saint Louis, Missouri: Washington University in St. Louis, May 2013.

[31] Yuchen Leng et al. "Comparisons of Different Propeller Wake Models for a Propeller-Wing Combination". In: *8th European Conference for Aeronautics and Space Sciences*. Madrid, Spain, July 2019. URL: https://hal.science/hal-03385864.

[32] R. DeLoach. "The modern design of experiments - A technical and marketing framework". In: *21st Aerodynamic Measurement Technology and Ground Testing Conference*. DOI: 10.2514/6.2000-2691.

[33] Melissa McDaniel et al. "Shadow UAV Wind Tunnel Testing using a Design of Experiments Approach". In: *2018 Aerodynamic Measurement Technology and Ground Testing Conference*. DOI: 10.2514/6.2018-4195.

[34] Joao Dias et al. "Aircraft Wind Tunnel Characterization using Modern Design of Experiments". In: *54th AIAA/ASME/ASCE/AHS/ASC Structures, Structural Dynamics, and Materials Conference*. DOI: 10.2514/6.2013-1502.

[35] Raul Yondo et al. "A review on design of experiments and surrogate models in aircraft real-time and many-query aerodynamic analyses". In: *Progress in Aerospace Sciences* 96 (2018), pp. 23–61. DOI: https://doi.org/10.1016/j.paerosci.2017.11.003.

[36] Simon Mak et al. "Minimax and Minimax Projection Designs Using Clustering". In: *Journal of Computational and Graphical Statistics* 27.1 (2018), pp. 166–178. DOI: 10.1080/10618600.2017.1302881.

[37] Xu He. "Rotated Sphere Packing Designs". In: *Journal of the American Statistical Association* 112.520 (2017), pp. 1612–1622. DOI: 10.1080/01621459.2016.1222289.

[38] Jacob J. Szymanski et al. "Experimental Investigation of the Static and Dynamic Stability Derivatives Using a Novel 3-DoF Mechanism". In: *AIAA SCITECH 2023 Forum*. DOI: 10.2514/6.2023-0799.

[39]   Eugene A. Morelli. "Flight Test Maneuvers for Efficient Aerodynamic Modeling". In: *Journal of Aircraft* 49.6 (2012), pp. 1857–1867. DOI: `10.2514/1.C031699`.

[40]   Eugene A. Morelli. "Practical Aspects of Multiple-Input Design for Aircraft System Identification Flight Tests". In: *AIAA AVIATION 2021 FORUM*. DOI: `10.2514/6.2021-2795`.

[41]   Abbott Ira. *Pressure-Distribution Measurements of a Model of a Davis Wing Section with Fowler Flap Submitted by Consolidated Aircraft Corporation*. Tech. rep. National Advisory Committee for Aeronautics. Langley Aeronautical Lab. Langley Field, VA, United States, Jan. 1942.

[42]   Christian Raab et al. "Dynamic flight load measurements with MEMS pressure sensors". In: *CEAS Aeronautical Journal* 12 (2021), pp. 737–753. DOI: `10.1007/s13272-021-00529-3`.

[43]   Matthew McCarty. "The measurement of the pressure distribution over the wing of an aircraft in flight". PhD thesis. Kensington, Australia: University of New South Wales, Aug. 2008. DOI: `10.26190/unsworks/18295`.

<div align="right">

A

</div>
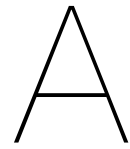
Wind Tunnel Experiment

This chapter gives a more detailed description of the wind tunnel experiment, which was originally planned, but later changed as a result of delays in manufacturing. Therefore, the description provided in this chapter will deviate from the description of the experiment given in Part I. First, the theory behind the wind tunnel experiment will be discussed in Section A.1. The quantities which will be measured and the hypotheses which were made will be stated in Section A.2. Finally, the hardware which was designed for the wind tunnel experiment will be explained in Section A.3.

A.1. Theory

To generate a roll moment, aerodynamic-surfaces are usually deflected to locally generate a higher lift force. This lift force can be characterized by the pressure distribution over the upper and lower halves of the wing and is often measured during wind tunnel experiments, even dating back to the early 1940s [41]. Similarly, the pressure distribution over the cross-section of the wing located behind the propellers can be measured during the wind tunnel experiment. The changes in pressure distribution as a function of propeller elevation can then be used to determine the strength of the propeller-wing interactions, and as a result their influence on the roll moment.

When a wing is subjected to airflow, it experiences surface pressure and shear stress, as shown in Figure A.1 [7]. At any given point the pressure is perpendicular to the surface and the shear force runs parallel to the surface.

$$p = p(s) = \text{surface pressure distribution}$$
$$\tau = \tau(s) = \text{surface shear stress distribution}$$
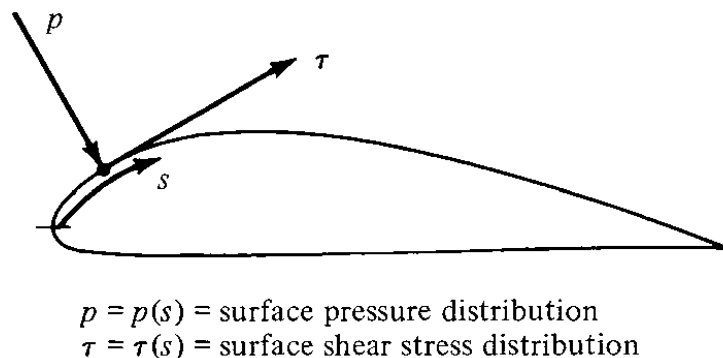
Figure A.1: Pressure and shear force definitions (taken from [7]).

The pressure and shear stress distributions can be integrated along the surface of the wing, as shown in Figure A.2.

<div align="center">

64

</div>
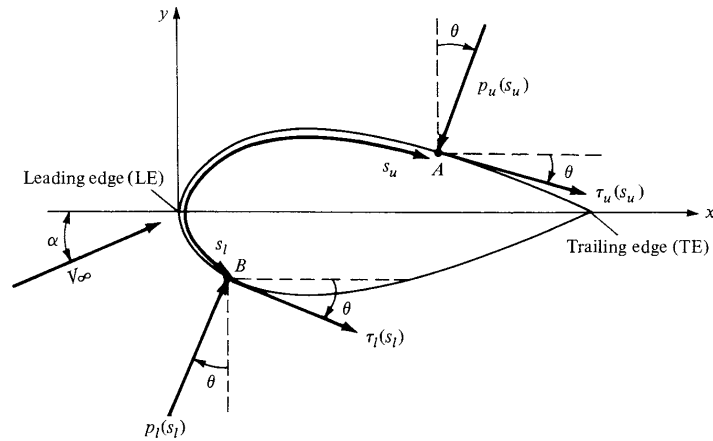
Figure A.2: Definitions of the integration of the pressure forces (taken from [7]).

Leading to the definitions of the normal and axial force given by Equation A.1 and Equation A.2, respectively.

$$N' = -\int_{LE}^{TE} (p_u \cos(\theta) + \tau_u \sin(\theta))\, ds_u + \int_{LE}^{TE} (p_l \cos(\theta) - \tau_l \sin(\theta))\, ds_l \tag{A.1}$$

$$A' = -\int_{LE}^{TE} (-p_u \sin(\theta) + \tau_u \cos(\theta))\, ds_u + \int_{LE}^{TE} (p_l \sin(\theta) + \tau_l \cos(\theta))\, ds_l \tag{A.2}$$

The definition of the lift force follows from Figure A.3, resulting in Equation A.3.

$$L = N \cos(\alpha) - A \sin(\alpha) \tag{A.3}$$

The shear force experienced on the wing is difficult to measure locally and is usually measured using a rake, which measures the change in energy in the flow. For low angle of attack the shear force is a magnitude smaller than the pressure force, therefore it will be neglected.
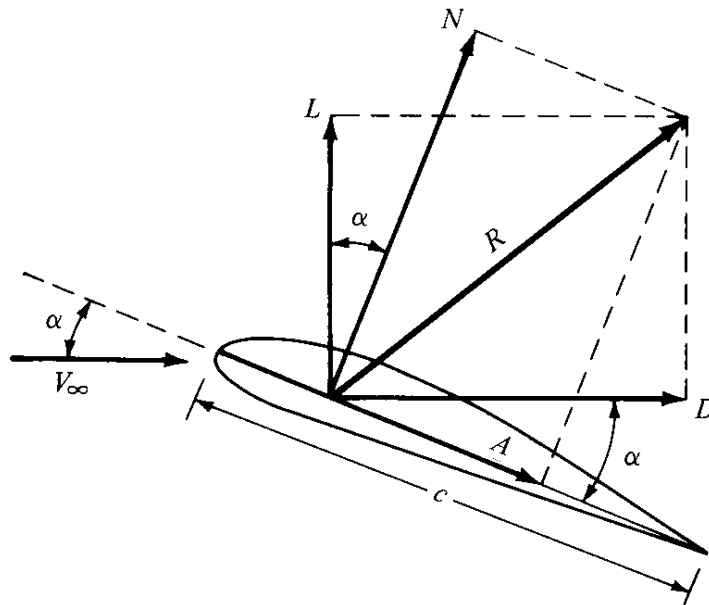
Figure A.3: Airfoil force definitions (taken from [7]).

A.2. Measurements and Hypotheses

First, the wind tunnel experiment should generate the data necessary to make a model capable of predicting the roll moment, but it should give insights into the following hypotheses:

1. The propeller-wing interactions have a damping effect on the roll moment generation from the propellers.

2. The rear propellers generate a roll moment more efficiently, as they do not contribute to the propeller-wing interactions to the same degree.

The independent variables for the wind tunnel test will be the airspeed, propeller rotational velocity and both front and rear propeller tilt angles. To make optimal use of the wind tunnel slot, it was decided to only vary the tilt of the rotors on the right side of the vehicle. This has no effect on the outcome of the experiment, as the vehicle is symmetric.

The issue regarding roll moment generation only occurs during fast, forward flight, therefore only part of the flight envelope needs to be covered. The airspeed during the experiment will be kept between nine and fifteen meters per second, as this is representative of the real drone's cruising speed.

As the propellers' RPM can vary substantially depending on the current state of the drone, a wide range of conditions should be tested. During cruise, the propellers usually spin at a rotational speed of around 700 radians per second, with a maximum of 1000 radians per second. It was decided to test speeds between 600 and 1000 radians per second, to cover both cases in which the drone would accelerate and decelerate.

Lastly, the entire tilt range of the propellers will be covered. This consists of a 145 degree range. For a description of tilt mechanism range, refer to Section 1.2.

In addition to measuring the pressure distribution over the wing located behind the propellers, the total forces and moments generated by the quad-plane will also be measured during the wind tunnel experiment.

As there is only a limited amount of wind tunnel time available, it was opted to forego testing the following quantities. First, the angle of attack will not be varied during the wind tunnel test, as it is assumed that the up/down wash generated by the propellers is not sufficient to exit the linear aerodynamic regime. A representative value of six degrees was chosen as this is often experienced during cruise. Additionally, aileron deflection was not taken into account, as they are not located in the wake of propellers, thus they will be entirely omitted from the wind tunnel model. It will also be assumed that the drone is flying with zero sideslip angle, although it is certainly possible that a non-zero sideslip angle has an effect on where the wake meets the wing, altering the propeller-wing interactions in the process. Lastly, the experiment does not consider the influence of relative wing and propeller location. Investigating the influence of relative location would require a lot of repeated testing, which is simply unattainable in a limited timeframe. However, future research could be focused on finding a configuration which minimizes or benefits from the propeller-wing interactions.

A.3. Setup

The next step is to come up with a practical setup for sensing the pressure on the wing. When measuring the pressure over airfoils, differential pressure sensors are often used. These sensors are too large to incorporate into the wing of a small quad-plane, and therefore tubes are usually routed from holes in the wing to the sensor. However, routing tubes is also a concern, as the wing is quite thin and structural elements make it difficult to route many tubes through certain sections of the wing.

Alternatively, Micro-Electromechanical System (MEMS) pressure sensors can be used. These sensors are usually absolute pressure sensors, as opposed to the differential pressure sensors discussed earlier, making them less accurate. However, they make up for it with their tiny size. A setup using MEMS pressure sensors would also not need tubes and they could be integrated into or over the wing. This has already been done before, Raab et al. used a MEMS pressure sensor array to approximate the strain on the wing using the pressure distribution [42]. They build a glove like structure which covered part of the wing. As the wing of the drone is quite thin, a glove would potentially disturb the aerodynamic characteristics as it locally alters the shape of the airfoil. Therefore, the best option would be to install the pressure sensors inside the wing. A Printed Circuit Board (PCB) can be designed which fits inside the wing and houses all the necessary MEMS pressure sensors.

McCarthy tested the accuracy of certain pressure sensor configurations and found that a cosine distribution lead to the best results [43]. It was further concluded that fitting eighteen sensors along the chord was enough to have a 1.0% average error in lift coefficient prediction.

Given the scale of the drone, fitting eighteen sensors along a single section of the chord would be difficult, therefore this number was reduced to twelve (six on the top half and six on the bottom half). Additionally, due to the load bearing structure, it would be difficult to perfectly follow a cosine distribution.

This chordwise distribution of twelve sensors will be placed in six spanwise locations to form an array of sensors, as this would also allow for observation of advancing and retreating blade effects covered in Chapter 7 and Figure 7.1. Again, due to the load bearing structure, it is impossible to fit sensors directly behind the rotor hub. Therefore, it was decided to have sensors located at 40%, 60%, and 80% of the propeller span, leading to a total of 72 sensors.

All 72 sensors should be driven by the same microcontroller, to prevent possible synchronization issues during post-processing of the data. The Serial Peripheral Interface (SPI) protocol was chosen to communicate data between the sensor and main board, as it supports driving many sensors in parallel with little wiring. The Teensy4.1 development board was chosen as the host controller[1]. Clearly, the Teensy4.1 does not have enough connections to connect all sensors. To solve this issue, two sensors are connected to the same Chip Select (CS) port, effectively cutting the required number of ports in half. This is possible because the Teensy4.1 has three (one is used for the SD card) dedicated hardware SPI ports. Additionally, the Bosch BMP581 barometric pressure sensor was chosen, as it comes in a small package, is well documented, and supports SPI.

A.4. PCB Design

To lessen the likelihood that a broken sensor or other manufacturing defects render the PCB useless, it was decided to split the setup into multiple modular parts. Therefore, the setup will be split into individual sensor strips, which contain twelve sensors each, and a main board which houses the Teensy4.1 host controller.

The sensor and main board PCBs must fit within the wing to be of any use during the experiment. Given the scale of the drone, there will be limited space to work with. Therefore, the PCB design stage consisted of design cycles, where first the PCB was designed. Subsequently, the designs were imported into CAD and an attempt was made to integrate them into the wing. Schematics and Gerber files for the PCBs can found on GitHub.

A.4.1. Main Board

The main board is responsible for housing the Teensy4.1 host controller and connecting to all six sensor strips. Three of the sensor strips would be connected to the top and three to the bottom of the main board. The front and back of the main board can be seen in Figure A.4 and Figure A.5, respectively.

A schematic of the main board is given in Figure A.6, and the bill of materials for the main board are given in Table A.1, excluding the Teensy4.1.

Table A.1: Main board bill of materials (1x), excluding the Teensy4.1 host controller.

Qty	Designator	Manufacturer	Mfg Part #	Footprint	Type
3	C1, C2, C3	KYOCERA AVX	0603YC105KAT2A	C 0603 (1608 Metric)	SMD
1	R1	Panasonic	ERJPA2F10R0X	R 0402 (1005 Metric)	SMD

---

[1]https://www.pjrc.com/store/teensy41.html
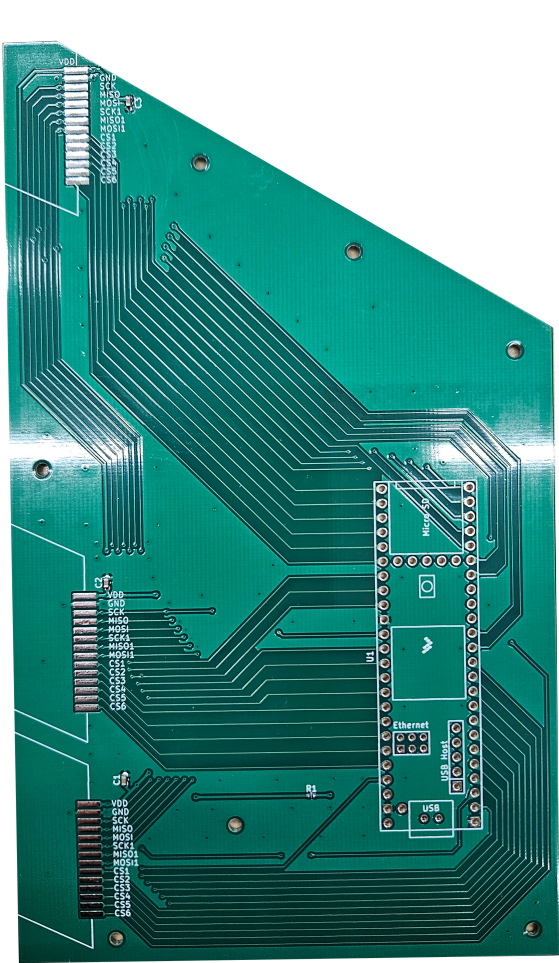
Figure A.4: Main board front
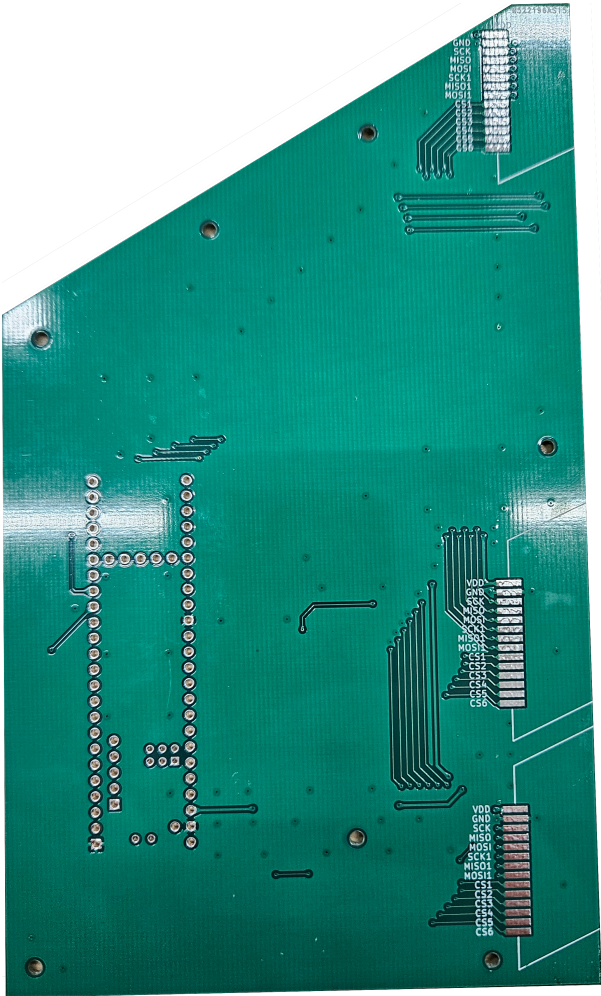
Figure A.5: Main board rear
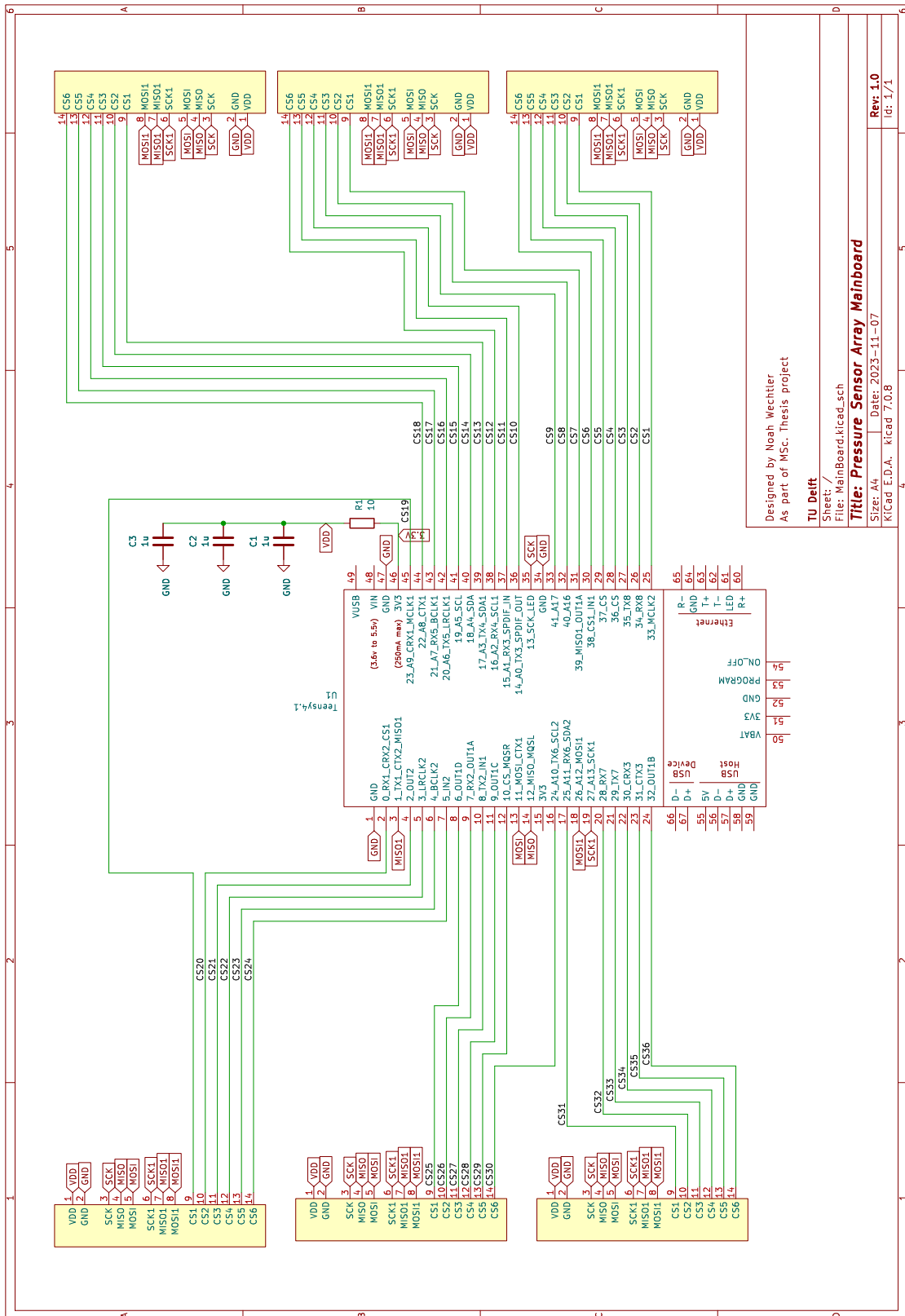
Figure A.6: Main board Schematic

A.4.2. Sensor Strip

Additionally, two kinds of sensor strips were designed. Both designs are identical but mirrored, this was necessary to align the sensors mounted at the top and bottom of the wing. Figure A.7 and Figure A.8 show the front and rear of a sensor strip meant to be mounted to the top of the wing, respectively.
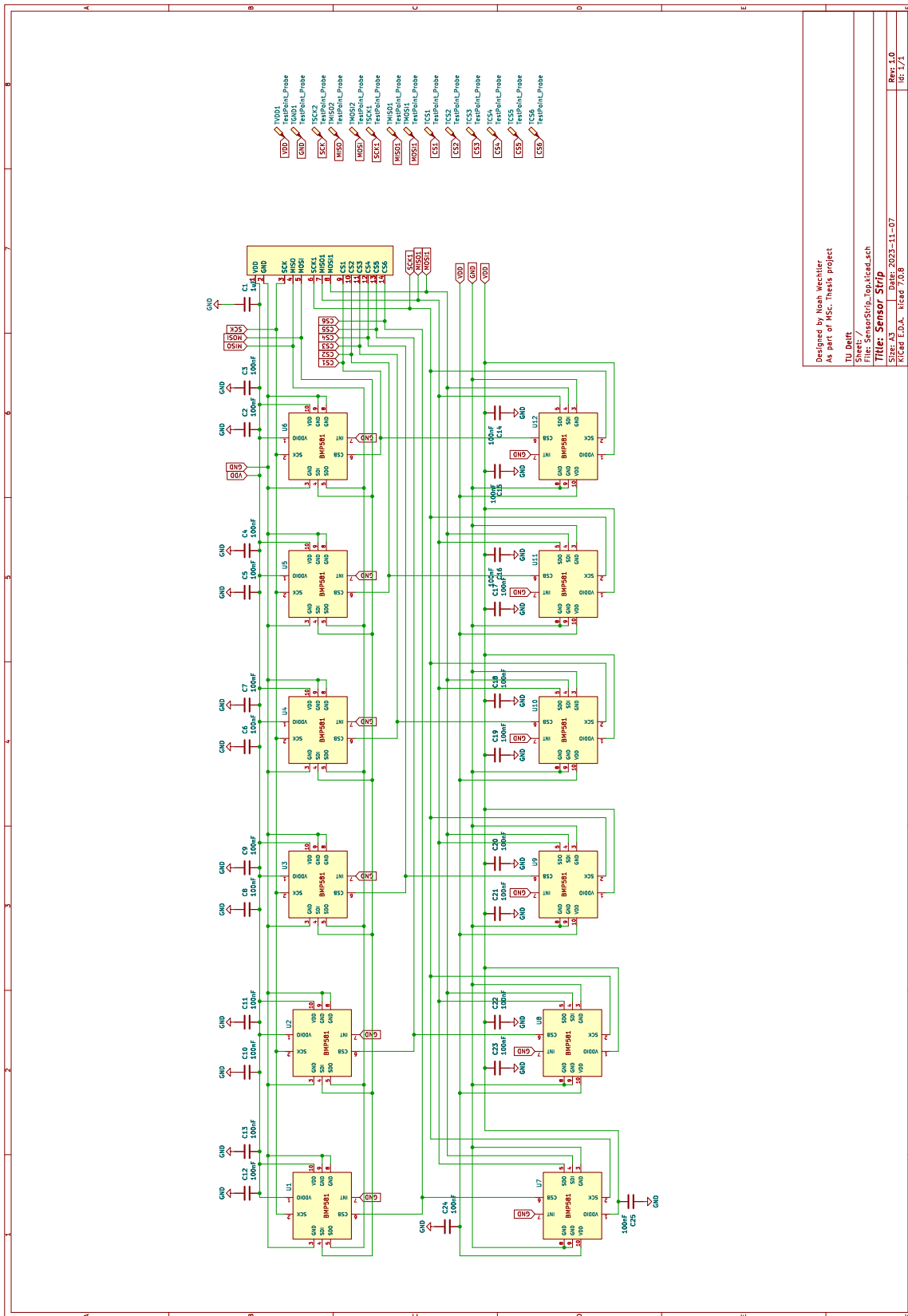

Figure A.7: Sensor strip front

Figure A.8: Sensor strip rear

The schematic of the sensor strip mounted to the top of the wing can be seen in Figure A.9, and the bill of materials for one of the sensor strips is given in Table A.2.

Table A.2: Sensor strip bill of materials (1x)

Qty	Designator	Manufacturer	Mfg Part #	Footprint	Type
12	U1-U12	Bosch	BMP581	Non-Standard[2]	SMD
24	C2-C25	KYOCERA AVX	02016D104KAT2A	C 0201 (0603 Metric)	SMD
1	C1	KYOCERA AVX	0603YC105KAT2A	C 0603 (1608 Metric)	SMD

---

[2]The footprint can be found in the BMP581 manual: `https://www.bosch-sensortec.com/media/boschsensortec/downloads/datasheets/bst-bmp581-ds004.pdf` Last Accessed: 12/04/2024

Figure A.9: Sensor strip schematic

A.4.3. Issues and Potential Improvements

Unfortunately, the PCBs did not arrive in time for the wind tunnel experiment, which led to the eventual changes mentioned in Section 1.2. Nevertheless, the PCBs were delivered at a later date and it would be a waste to not test whether they worked.

While setting up the PCBs, it was immediately noticeable that it would be impossible for the castellated edges to support any load. After soldering two connections between the main board and a sensor strip, the copper plating of the castellated edges separated from the sensor strip under minimal force. This was already expected during the design of the PCBs, and a supporting structure was designed to keep the assembly together. However, it is still recommended to replace the castellated edges with different connectors if the design is reused.

The BMP581 manual mentioned to use a 10 Ohm resistor between the power source and the sensors if it was suspected that the rising edge of the voltage could be sharp. However, during testing with a single strip it was noticed that the resulting voltage at the sensors was too low, and therefore the sensors could not be driven with the Teensy's 3.3V output. Attempts to short the resistor resulted in tripping the overcurrent protection of the Teensy's 3.3V rail. This was clearly an oversight in the design, but it might be possible to solve this issue by connecting the Teensy's 5V rail to the power trace, as it would result in a higher voltage at the sensors.

For further testing, it was decided to connect the sensor strips using an external power supply. This finally resulted in the sensors powering up, and being recognized by the driver. According to the driver, the sensors were all successfully configured, however no real pressure data was ever received by the Teensy. The driver has been used previously on a combination of BMP581 breakout boards with no trouble, indicating that the issue lie elsewhere. No further signal analysis has been done to determine the root cause behind this issue, as the wind tunnel test was already over by this time and attention had to be spent on other parts of the project.

B

Flight Tests: Additional Figures

This appendix contains additional figures, not shown in the scientific paper, which provide additional context to the results stated in Section 1.3. First, Section B.1 gives the linear and angular velocities and accelerations which were commanded and experienced by the quad-plane during the flight in which all model additions and no ailerons were used. Similarly, Section B.2 and Section B.3 provide figures showing the linear and angular velocities and accelerations of the new and old model when allowed to use ailerons. Additionally, Figure B.1 compares the commanded and experienced aileron deflections during all flight tests.
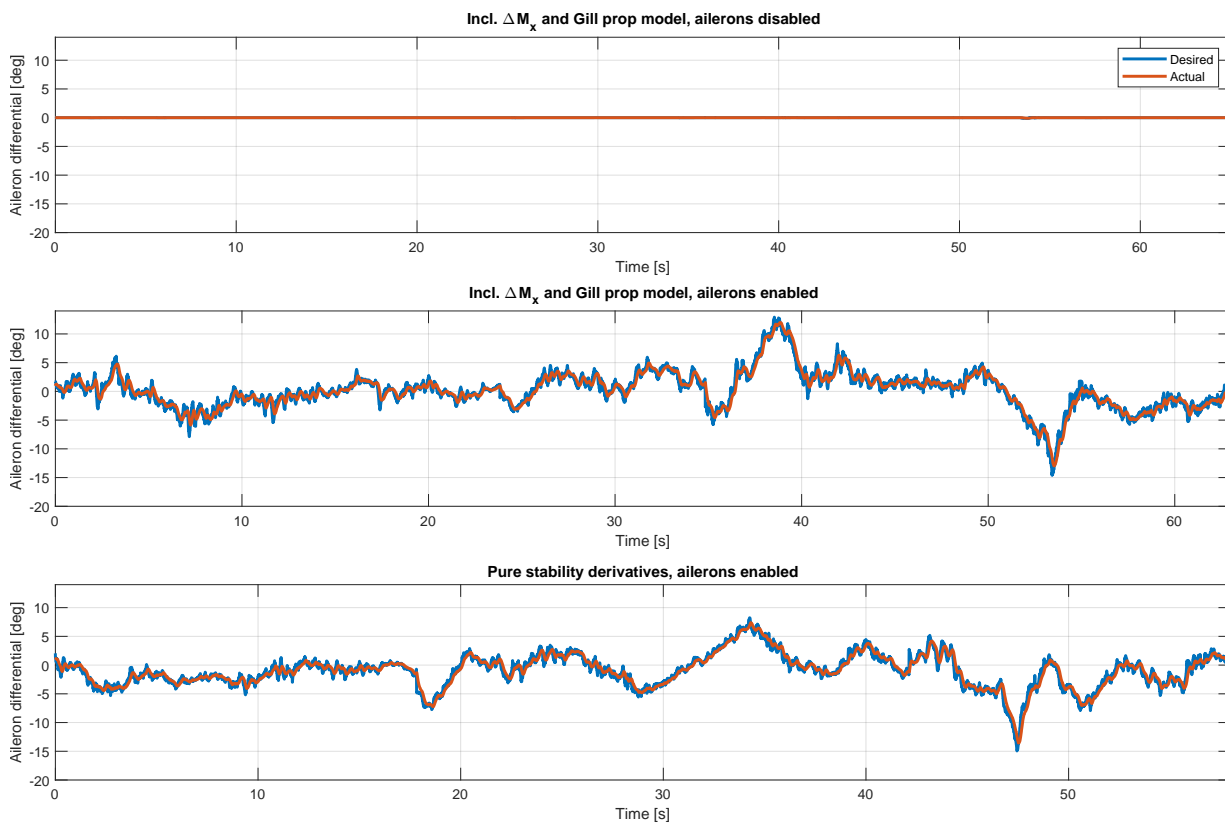
Figure B.1: Aileron commands

B.1. With Model Inclusions, Ailerons Disabled
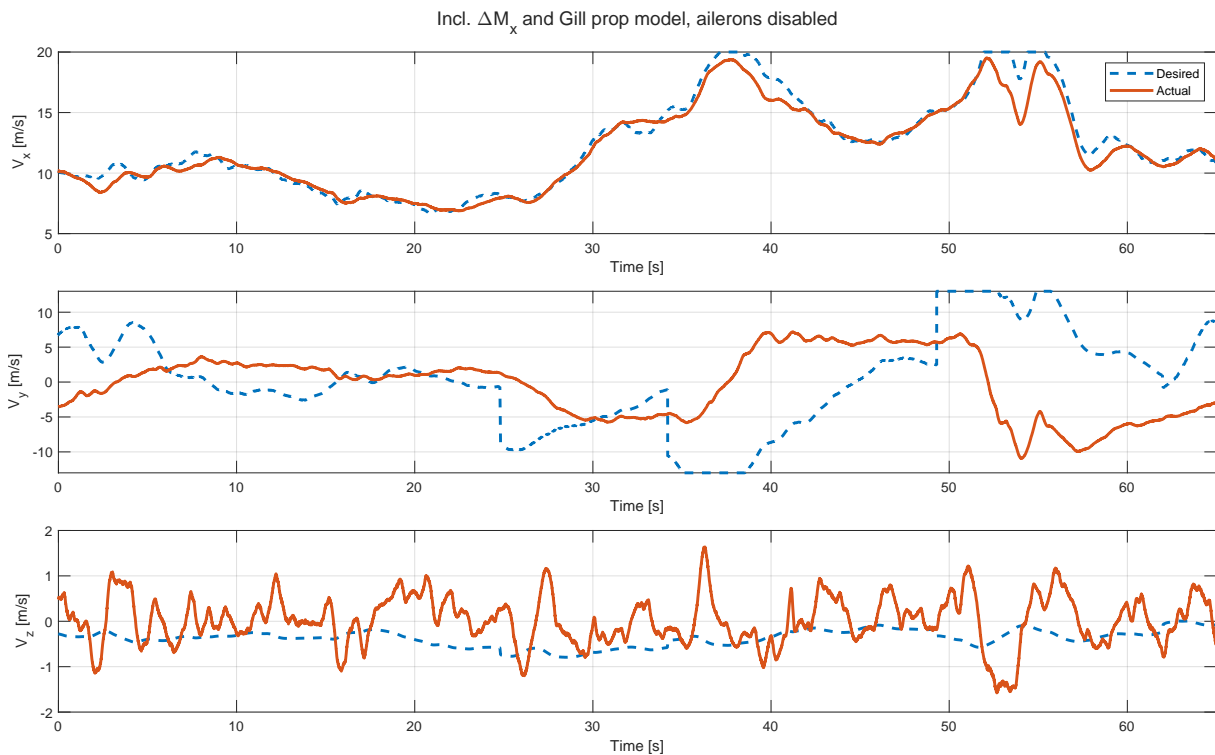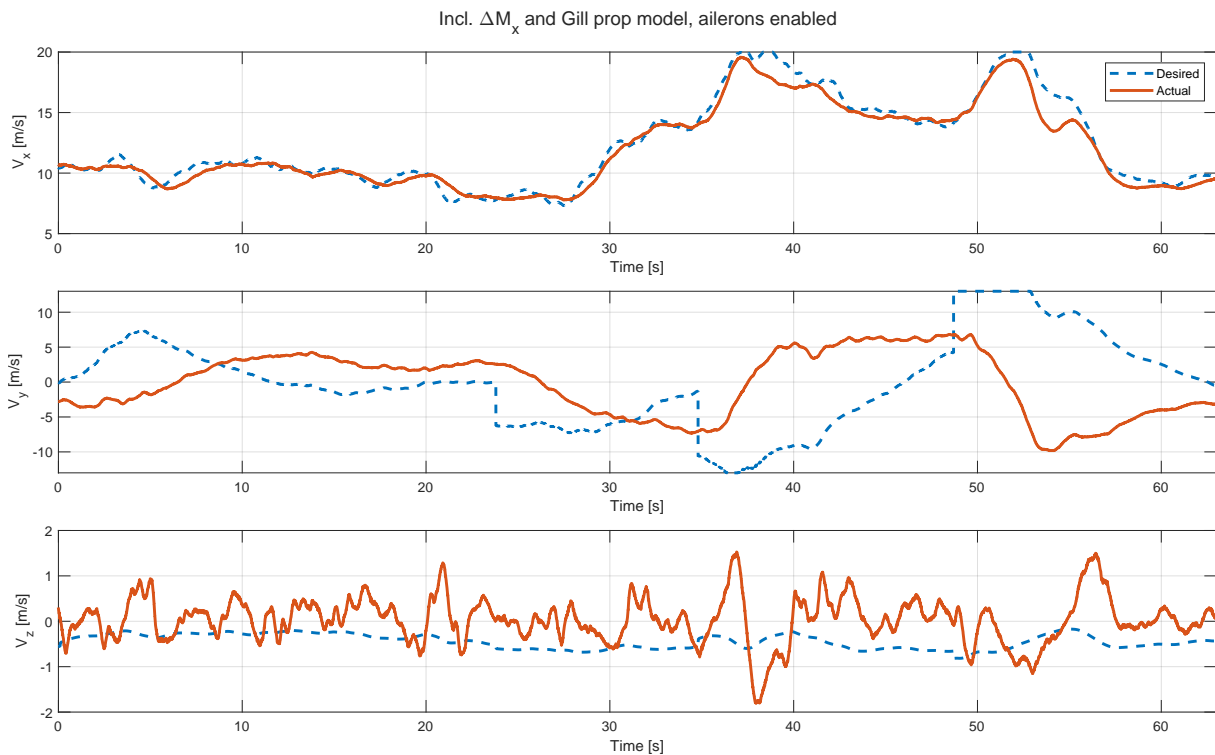

Figure B.2: Linear velocity tracking when ΔM_x and Gill's propeller model are included in the control allocation, with ailerons disabled. V_y is not tracked during fast, forward flight.
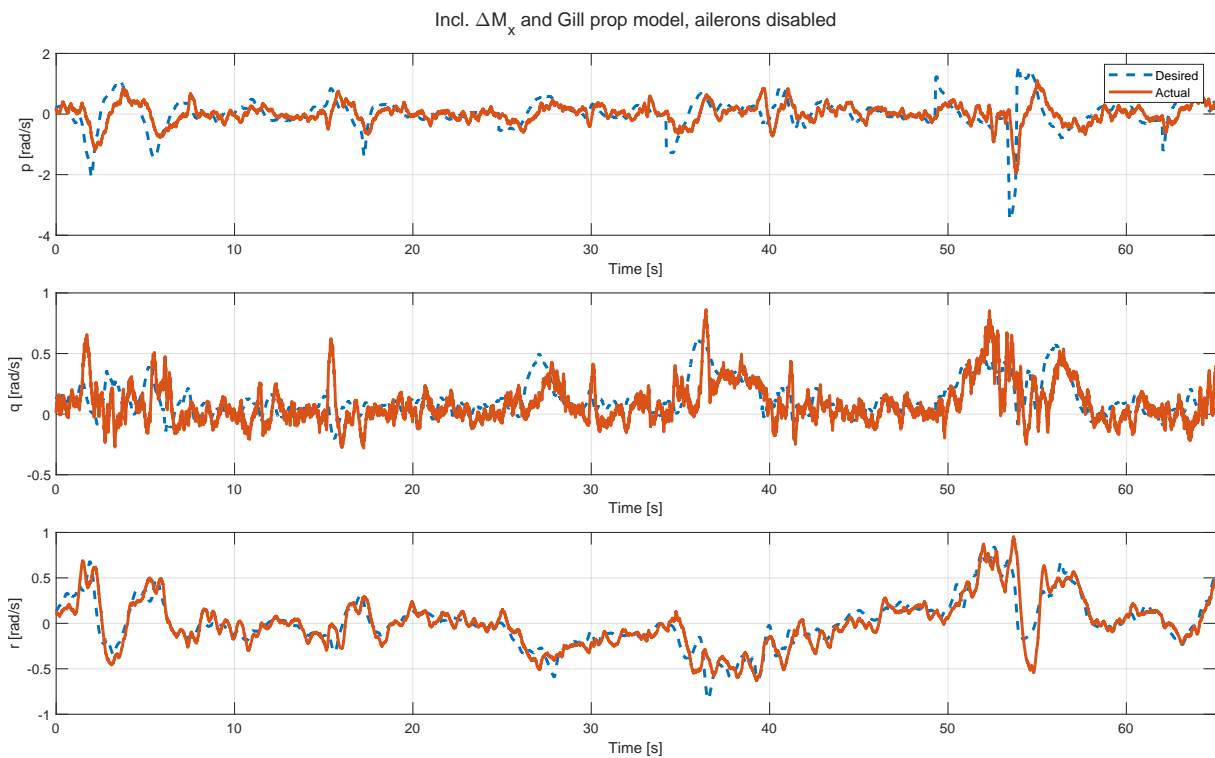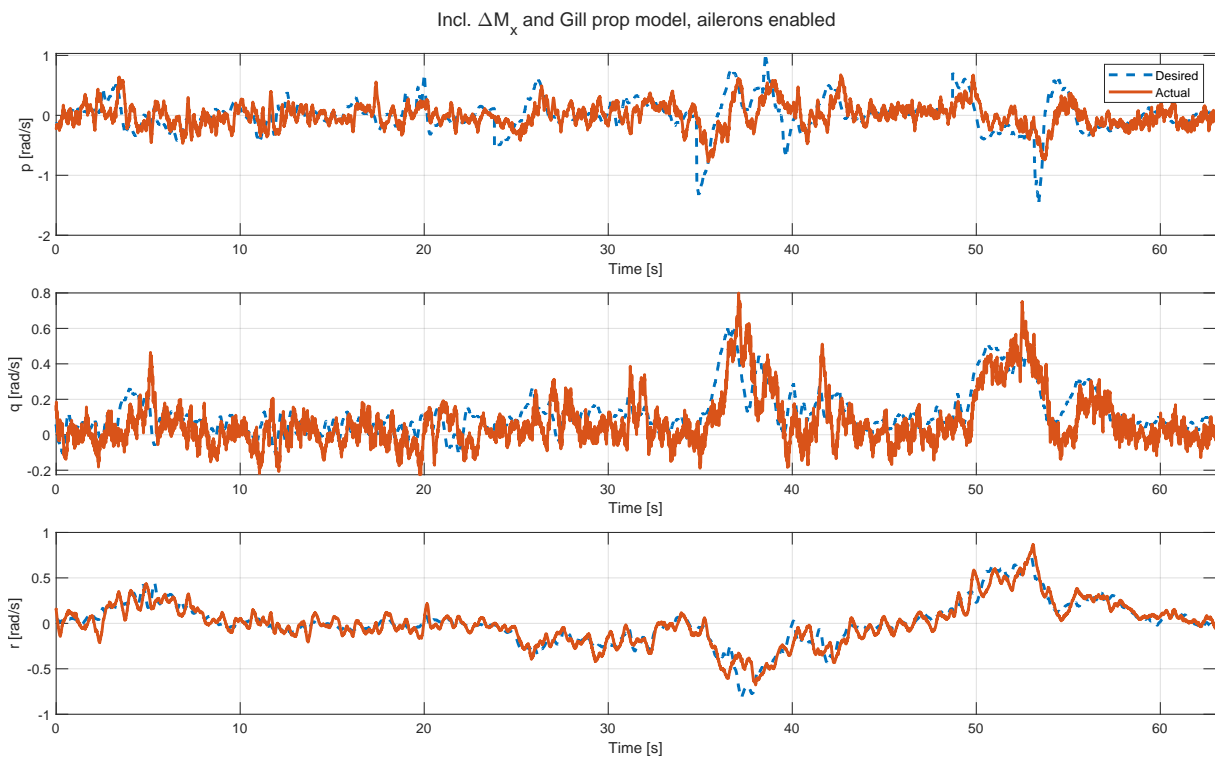

Figure B.3: Angular velocity tracking when ΔM_x and Gill's propeller model are included in the control allocation, with ailerons disabled.
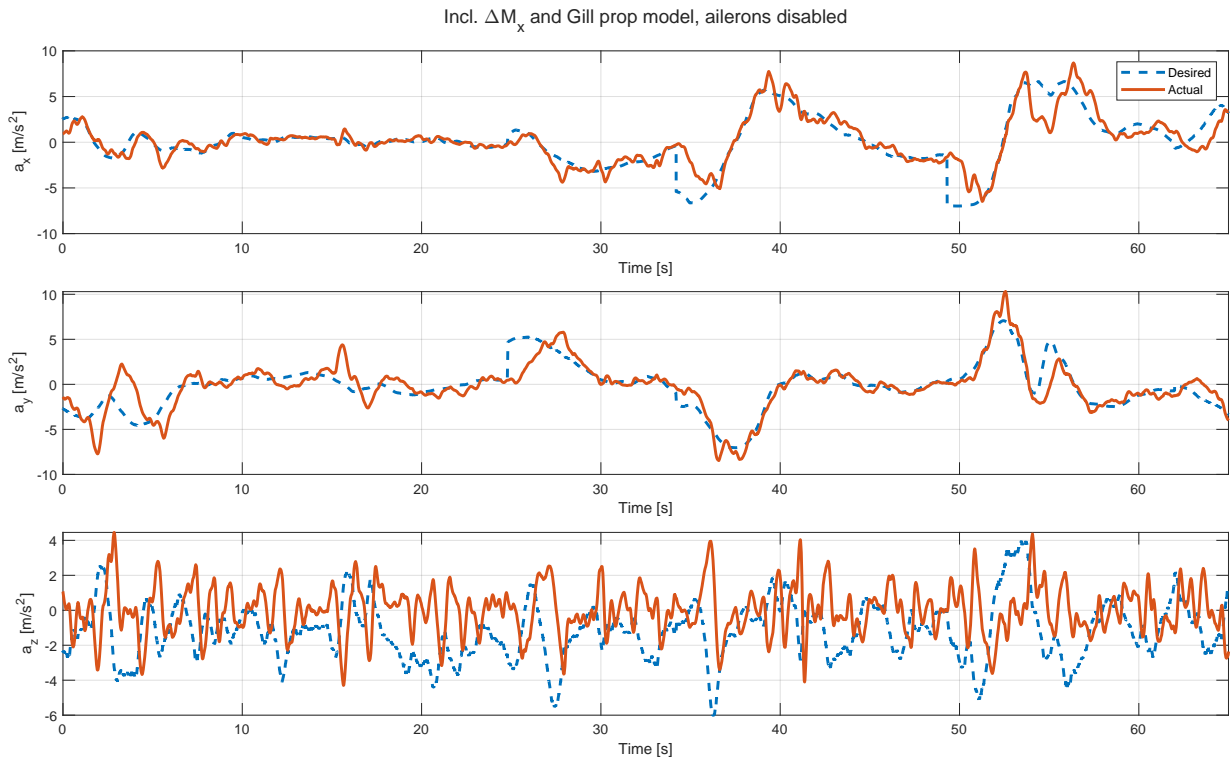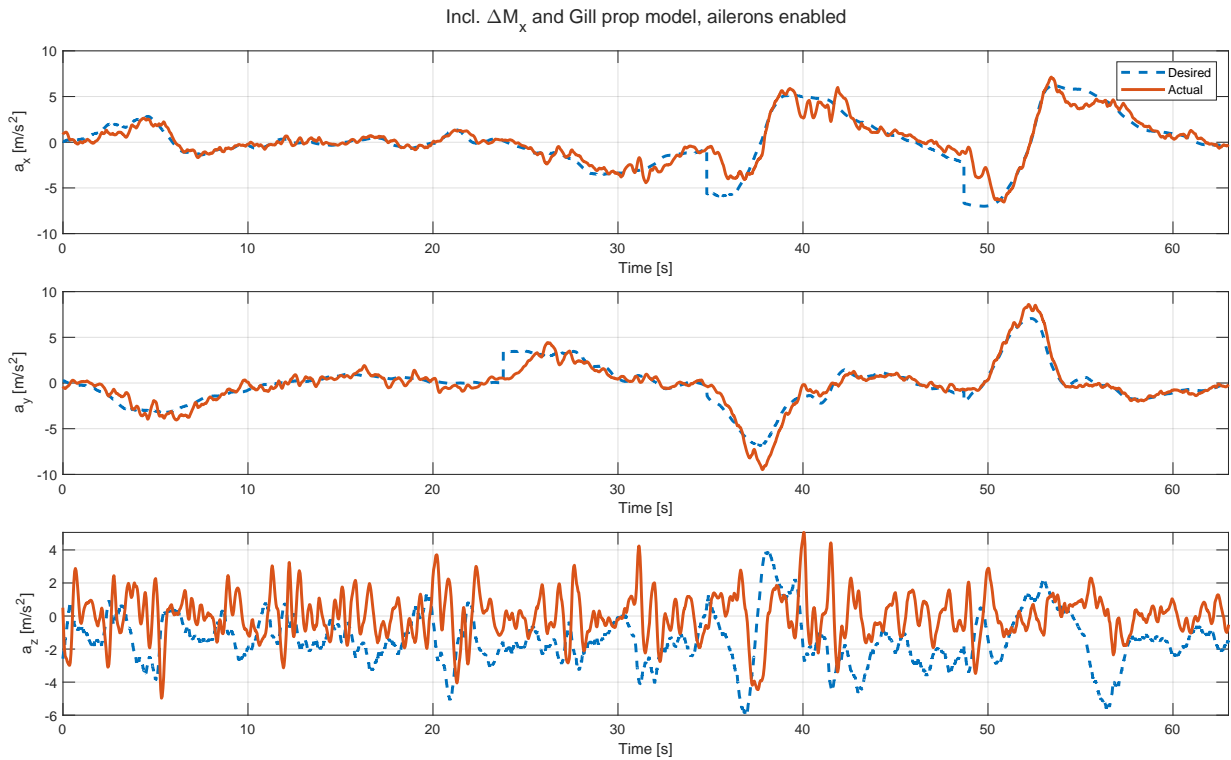
Figure B.4: Linear acceleration tracking when ΔM_x and Gill's propeller model are included in the control allocation, with ailerons disabled.
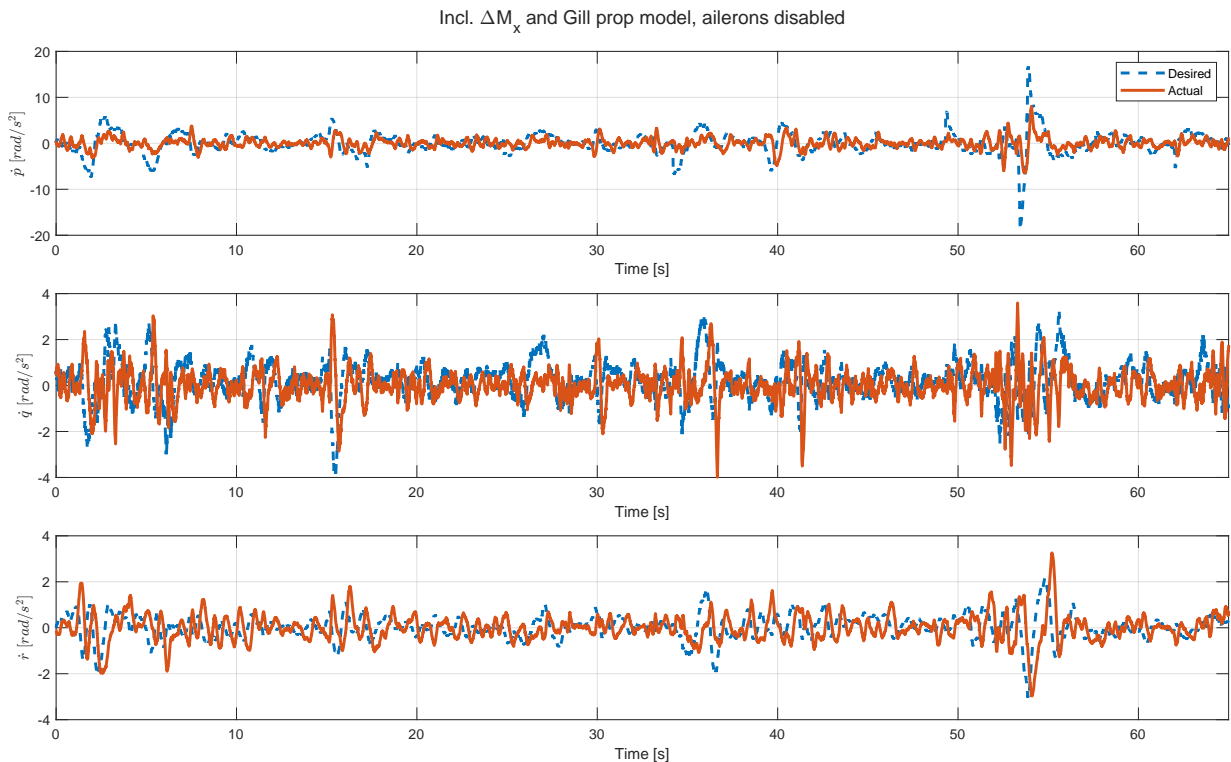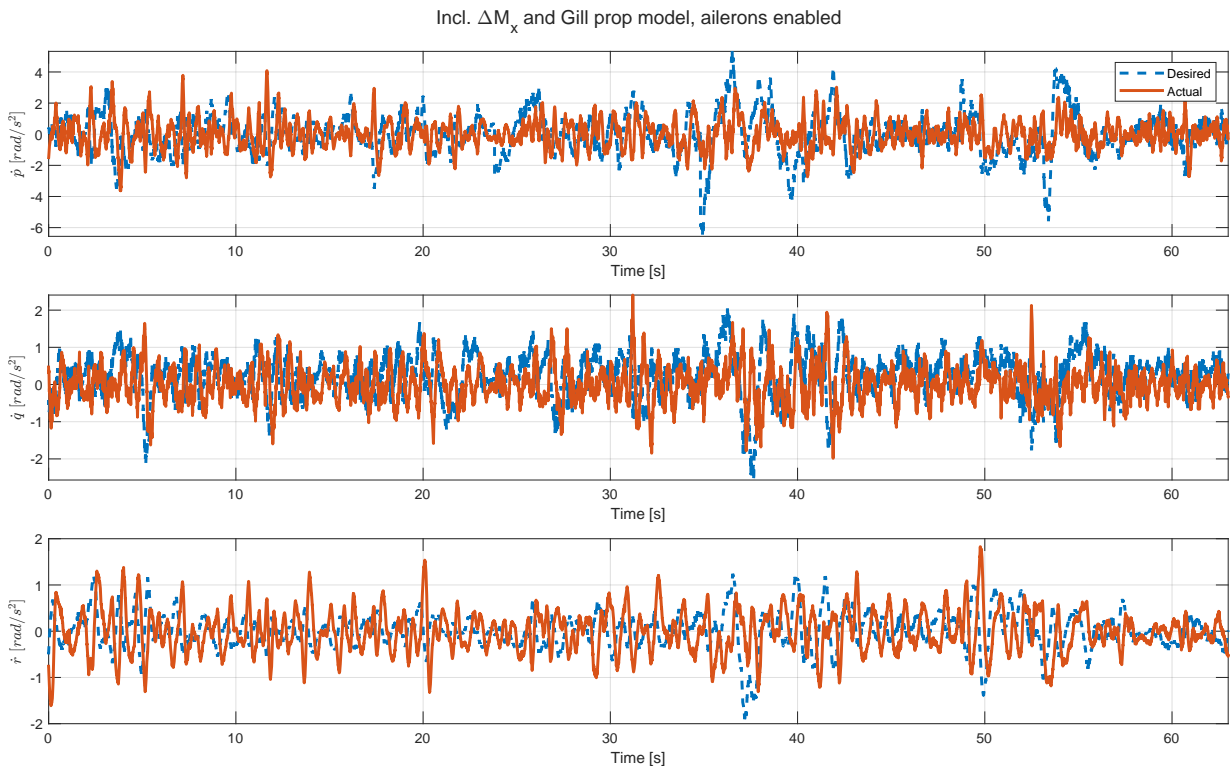

Figure B.5: Angular acceleration tracking when ΔM_x and Gill's propeller model are included in the control allocation, with ailerons disabled.

B.2. With Model Inclusions, Ailerons Enabled

Figure B.6: Linear velocity tracking when ΔM_x and Gill's propeller model are included in the control allocation, with ailerons enabled. V_y is not tracked during fast, forward flight.

Figure B.7: Angular velocity tracking when ΔM_x and Gill's propeller model are included in the control allocation, with ailerons enabled.

Figure B.8: Linear acceleration tracking when ΔM_x and Gill's propeller model are included in the control allocation, with ailerons enabled.

Figure B.9: Angular acceleration tracking when ΔM_x and Gill's propeller model are included in the control allocation, with ailerons enabled.
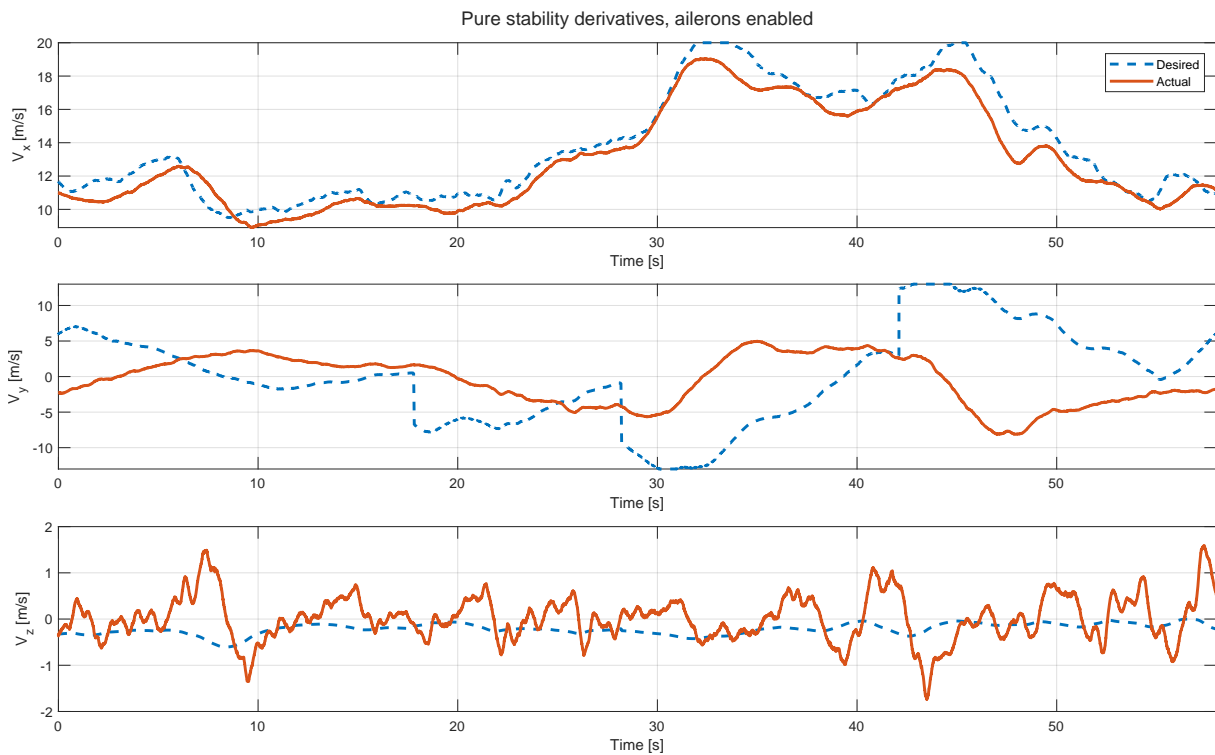
B.3. Pure Stability Derivatives, Ailerons Enabled

Figure B.10: Linear velocity tracking when pure stability derivatives are used in the control allocation, with ailerons enabled. V_y is not tracked during fast, forward flight.
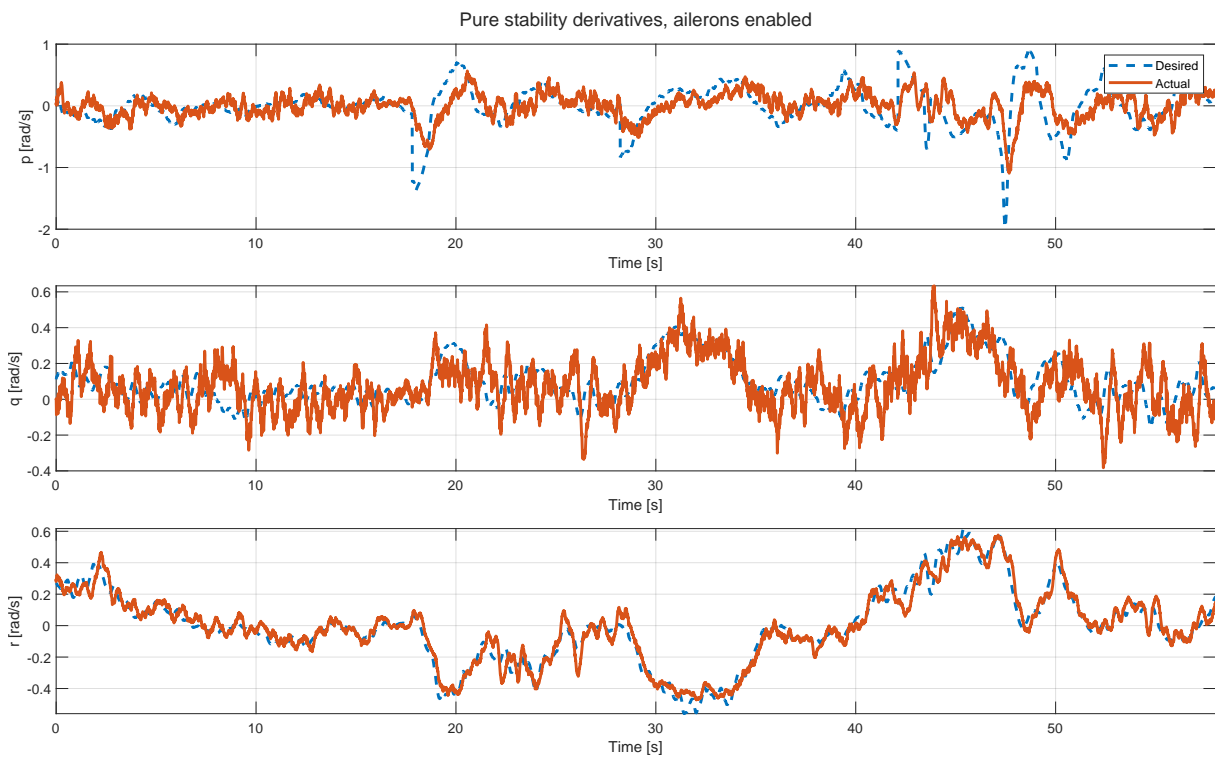

Figure B.11: Angular velocity tracking when pure stability derivatives are used in the control allocation, with ailerons enabled.
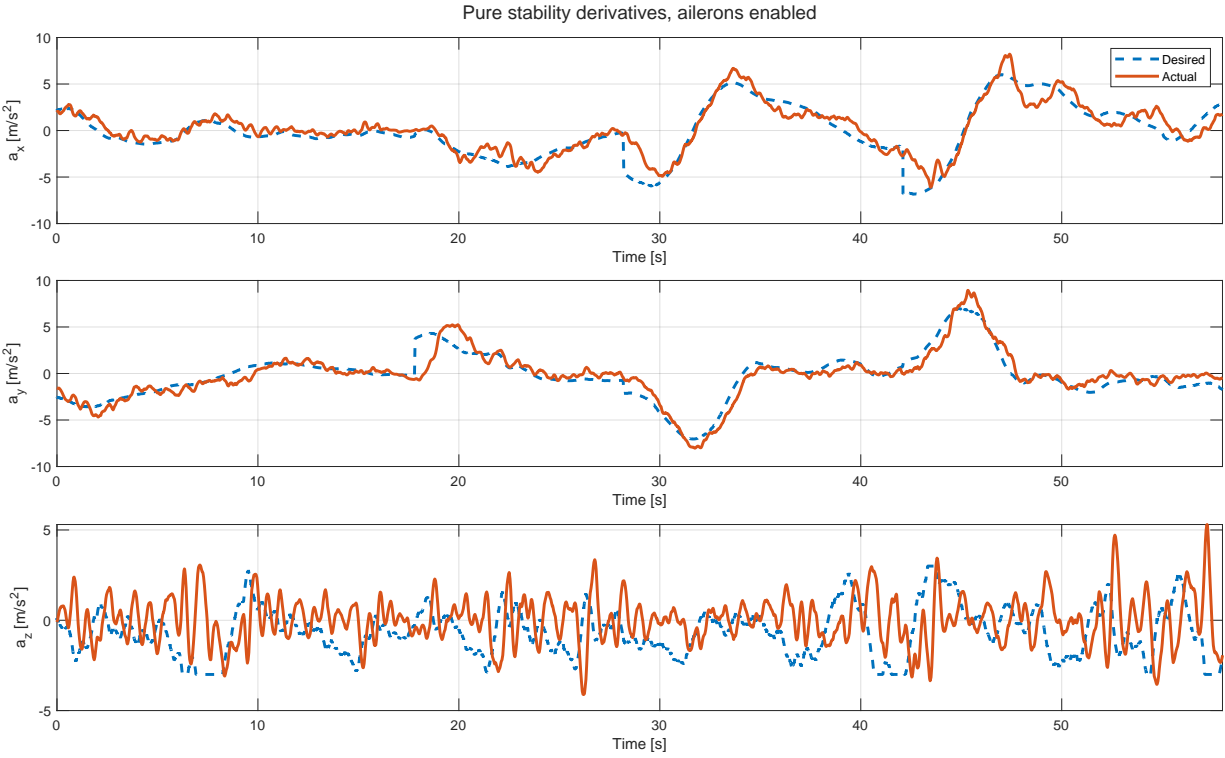
Figure B.12: Linear acceleration tracking when pure stability derivatives are used in the control allocation, with ailerons enabled.
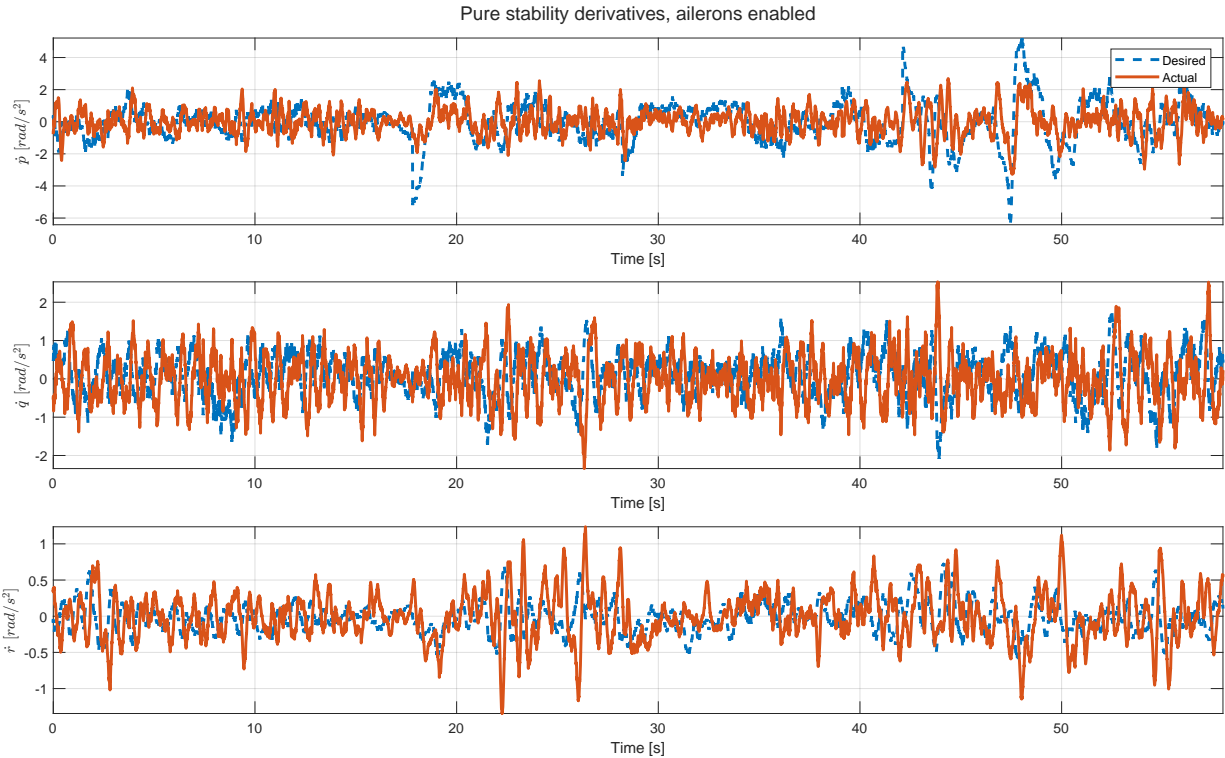

Figure B.13: Angular acceleration tracking when pure stability derivatives are used in the control allocation, with ailerons enabled.